

Thickness Determination of Melanocytic Nevi by Means of Optical Coherence Tomography

Der Fakultät für Mathematik und Physik
der Gottfried Wilhelm Leibniz Universität Hannover

zur Erlangung des Grades
Doktor der Naturwissenschaften
Dr. rer. nat.

genehmigte Dissertation von

M.Sc. Arthur Varkentin

geboren am 05.08.1985 in Purkary (Moldawien)

2018

Referent: Prof. Dr. Bernhard Roth - Hannoversches Zentrum für optische Technologien
Korreferent: Prof. Dr. Uwe Morgner - Institut für Quantenoptik
Tag der Promotion: 09.05.2018

Abstract

This thesis presents a fast, reliable, and non-invasive method for *in vivo* thickness determination of melanocytic nevi, and melanomas in particular. Such a tool is highly desirable for clinical dermatology as it may facilitate the identification of surgical melanoma margins, determine if a sentinel node biopsy should be performed or not, and, thus, reduce the number of surgical interventions for patients.

In this work, optical coherence tomography (OCT) is evaluated for quantitative *in vivo* preoperative assessment of the melanocytic skin infiltration depth. Comparison with the Breslow tumor thickness obtained from subsequent histopathology as the gold standard reveals that non-invasive OCT can determine the infiltration depth of melanocytic lesions preoperatively and *in vivo* with an accuracy comparable to invasive histopathology measurements on skin biopsies. Moreover, OCT can produce volumetric images of the lesion giving access to lateral and axial dimensions after applying an image segmentation algorithm. Successive OCT measurements allow for growth tracking of the invisible parts below the skin surface and the evolution of the lesion infiltration depth.

In addition, a multimodal measuring device for rapid, noninvasive *in vivo* skin cancer screening is presented, combining three optical modalities: OCT and optoacoustics (OA) to provide precise tumor depth determination with a Raman spectroscopic modality capable of detecting the lesion type and, thus, providing diagnostic capability. Both setups, OA and Raman, use wide field skin illumination to ensure compliance with Maximum Permissible Exposure (MPE) requirements for clinical use. The Raman signal is collected via the OCT scanning lens to maximize the signal-to-noise ratio (SNR) of the measured signal. OCT is used to optically determine the tumor thickness and for volumetric imaging whereas optoacoustics utilizes acoustic signals generated by optical absorption contrast for thickness determination at potentially higher penetration depths compared to OCT.

Results of first clinical trials using the described setup are also presented in this work. The measured lesion depth is in good agreement with histology results, while Raman measurements show distinctive differences between normal skin and melanocytic lesions, and, moreover, between different skin areas.

For future work, approaches are discussed to validate the setup for reliable detection of pathophysiological parameters, morphology and thickness of suspicious skin lesions.

Key words: optical coherence tomography, human skin, *in vivo*, skin cancer, tumor margin assessment, medical device, multimodal, optics measurement system

Kurzzusammenfassung

Die vorliegende Dissertation präsentiert eine Methode zur schnellen, zuverlässigen *in vivo* Dickenbestimmung von melanozytären Nevi. Ein derartiges Instrument ist für die klinische Dermatologie höchst wünschenswert, da es die Identifizierung von chirurgisch relevanten Melanom-Rändern erleichtert und der Dermatologe schneller bestimmen kann, ob eine Lymphknoten-Biopsie durchgeführt werden sollte oder nicht. Dies würde die Anzahl der chirurgischen Eingriffe für die Patienten signifikant verringern.

In dieser Arbeit wird die optische Kohärenztomographie (OCT) zur präoperativen *in vivo* Messung der melanozytären Hautinfiltrationstiefe evaluiert. Ein Vergleich mit der Breslow-Tumordicke, die aus der nachfolgenden histopathologischen Analyse, dem Goldstandard, erhalten wurde, zeigt, dass die nicht-invasive OCT-Messung die Infiltrationstiefe von melanozytären Läsionen präoperativ mit einer Genauigkeit messen kann, die mit einer invasiven histopathologischen Messung vergleichbar ist. Darüber hinaus kann das OCT volumetrische Bilder der Läsion erzeugen, die nach Anwendung eines Bildsegmentierungsalgorithmus Zugang zur lateralen und axialen Ausdehnung gewähren. Wiederholte OCT-Messungen ermöglicht so eine Verfolgung des Läsionswachstums unterhalb der Hautoberfläche und insbesondere des Dickenwachstums. Darüber hinaus wird ein multimodales Messsystem zur schnellen, nicht invasiven *in vivo* Hautkrebs-Früherkennung vorgestellt. Es kombiniert drei optische Modalitäten: OCT und Optoakustik (OA) zur präzisen Bestimmung der Tumortiefe und Raman-Spektroskopie, die den Läsionstyp erfassen kann und Diagnosefähigkeiten bereitstellt. Beide Geräte, OA und Raman, verwenden eine Weitfeld-Hautbeleuchtung, um die Einhaltung der maximalen zulässigen Expositionsanforderungen (MPE) für die klinische Verwendung sicherzustellen. OCT wird zur optischen Bestimmung der Tumordicke und zur volumetrischen Bildgebung verwendet, während die OA akustische Signale einsetzt, die durch optischen Absorptionskontrast für die Dickenbestimmung mit höheren möglichen Eindringtiefen im Vergleich zu OCT erzeugt werden.

Ergebnisse einer präklinischen Studie sind ebenfalls Teil dieser Arbeit. Die gemessenen Läsionstiefen stimmen gut mit den histologischen Ergebnissen überein, während die Raman-Messungen deutliche Unterschiede zwischen normaler Haut und melanozytären Läsionen und zwischen verschiedenen Hautbereichen zeigen.

Für zukünftige Anwendungen werden konkrete Ansätze diskutiert, um den Aufbau für den zuverlässigen Nachweis pathophysiologischer Parameter, Morphologie und Dicke verdächtiger Hautläsionen zu validieren.

Schlagwörter: optische Kohärenztomographie, menschliche Haut, *in vivo*, Hautkrebs, Tumor Sicherheitsabstand, medizinisches Instrument, multimodal, optisches Messsystem

Für Elisa und Lukas

Contents

1	Introduction	1
2	Human skin and malignant melanoma	5
2.1	Skin physiology	5
2.2	Optical properties of human skin	7
2.2.1	Absorption	7
2.2.2	Elastic scattering	8
2.2.3	Inelastic scattering	10
2.3	Acoustic properties of human skin	10
2.4	Malignant melanoma	11
2.4.1	Dermatological classification criteria	11
3	Optical coherence tomography on scattering media	13
3.1	Types and Principles of OCT	13
3.1.1	Time domain OCT	14
3.1.2	Spectral domain OCT	16
3.1.3	Swept-source OCT	17
3.1.4	Other OCT types	19
3.2	Theory of spectral domain OCT signal generation	21

Contents

3.3	Characteristics of optical coherence tomography measurements	26
3.3.1	Image distortions and measurement artifacts	27
3.3.2	Coherence gating, axial resolution and sensitivity roll-off	31
4	Quantitative measurements of optical properties	35
4.1	Optical coherence tomography setup	35
4.2	Homogeneous tissue phantoms for optical coherence tomography . . .	37
4.2.1	Homogeneous liquid phantoms	37
4.2.2	Homogeneous hydrogel phantoms	38
4.2.3	Layered phantoms	39
4.3	Layer thickness and refractive index	41
4.4	Scattering coefficient	42
5	Numerical OCT simulations	45
5.1	Simulation of an OCT A-scan	47
5.1.1	Modeling of the coherence condition	48
5.1.2	Modeling of multiple scattering	49
5.2	Simulations and Measurements	52
5.3	Discussion	59
6	Preclinical studies	63
6.1	Histopathology, a gold standard	63
6.2	Thickness determination of melanocytic lesions with OCT and high frequency ultrasound	63
6.3	Materials and methods	66
6.3.1	Patients	66

6.3.2	Imaging devices	66
6.3.3	Image processing	67
6.4	Results and discussion	69
6.5	Conclusions	74
7	Lesion segmentation	75
7.1	2-D-segmentation of cross-sectional OCT lesion data	76
7.2	3-D-segmentation of volumetric OCT lesion data	81
8	Multimodal approaches including optical coherence tomography	85
8.1	Optical coherence tomography with optoacoustics	85
8.1.1	Optoacoustics	86
8.1.2	Preliminary multimodal OCT-optoacoustics measurements	86
8.2	Combined OCT-Raman and co-localized optoacoustic measurements	89
8.2.1	Experimental setup	89
8.2.2	Ethics and Maximum Permissible Exposure compliance	93
8.2.3	Measurement protocol	94
8.3	Data processing	96
8.3.1	OCT	96
8.3.2	Optoacoustics	97
8.3.3	Raman	98
8.4	Results and discussion	101
8.4.1	OCT	101
8.4.2	Optoacoustics	101
8.4.3	Raman	103
8.4.4	General	103

Contents

8.5 Conclusions	104
9 Conclusions and outlook	107
Appendix	111
A Device specifications	111
A.1 TELESTO-II - Spectral Domain OCT Imaging System	111
A.2 GON360 - Instrument Systems	117
B Layer segmentation	119
B.1 EpiSeg_GetData.m	119
B.2 LayerDetection2D.m	123
B.3 boundary_detection.m	125
B.4 classification3.m	130
B.5 LayerDetection3D.m	133
B.6 EpiSeg_Example.m	136
Bibliography	145

Acronyms

Notation	Description
APSF	axial point spread function
CPSF	confocal point spread function
CUDA	Compute Unified Device Architecture
DEJ	dermoepidermal junction
DFT	discrete Fourier transform
FD-OCT	frequency domain optical coherence tomography
FF-OCT	full-field optical coherence tomography
FF-TD-OCT	full-field time domain optical coherence tomography
FWHM	full width at half maximum
GPU	graphics processing unit
HD-OCT	high definition optical coherence tomography
HFUS	high frequency ultrasound
ITO	indium tin oxide
LSP	least scattered photons
MC	Monte Carlo
MPE	Maximum Permissible Exposure
MSP	multiple scattered photons
NA	numerical aperture
NIR	near-infrared
OA	optoacoustics
OCT	optical coherence tomography
PCA	principal component analysis
PMMA	polymethyl methacrylate

Acronyms

Notation	Description
PVA	polyvinyl alcohol
PVDF	polyvinylidene fluoride
SD-OCT	spectral domain optical coherence tomography
SDK	software development kit
SDS	sodium dodecyl sulfate
SLD	superluminescent diode
SNR	signal-to-noise ratio
SS-OCT	swept source optical coherence tomography
TD-OCT	time domain optical coherence tomography
UV	ultraviolet
VIS	visible

List of Symbols

Notation	Description
c	speed of sound
dB	decibel, logarithmic unit
d_m	measured optical axial distance
d_{\max}	expected depth, based on the simulated path length
d_r	real axial distance
\mathbf{E}	electric field
E	electric field amplitude
F_w	weighting function
g	anisotropy factor
$\gamma(z)$	coherence function
$h(z)$	confocal point spread function
$I_D(k)$	detected intensity spectrum
$i_D(z)$	detected intensity depth profile
k	wavenumber
λ	wavelength
λ_0	center wavelength
L_c	coherence length (simulation parameter)
l_c	coherence length
L_p	simulated total optical path length
MHz	megahertz, frequency unit, 10^6 Hz, 10^6 s $^{-1}$
μ_a	absorption coefficient
μ_s	scattering coefficient
μJ	microjoule, energy unit, 10^{-6} J

List of Symbols

Notation	Description
mW	milliwatt, power unit, 10^{-3} W
n	refractive index
N_{se}	number of scattering events
ν	frequency
φ	simulated acceptance angle of the detector
π	pi, mathematical constant
$p(\theta)$	Henye-Greenstein phase function
\mathcal{R}	power reflectivity
r	field reflectivity
ρ	detector responsivity
$S(k)$	power spectrum
θ	scattering angle
$u_x(\theta), u_y(\theta), u_z(\theta)$	cosine projections, direction cosines
ω	angular frequency
w_0	Gaussian beam waist
$w(z)$	Gaussian profile
z	axial position coordinate
z_{f}	axial focal point
z_{i}	Rayleigh length
z_{max}	maximal reached geometrical depth

1

Chapter 1

Introduction

Melanocytic nevi, also referred to as mole or liver spot, are pigmented skin lesions. In most cases they are harmless marks on human bodies. However, primarily due to UV exposure the eponymous melanocytes, cells responsible for the pigmentation, mutate and cause uncontrolled growth. As a result, the very dangerous skin cancer type malignant melanomas can develop. This process from degeneration to spreading can be very fast within months but it can also last several years. In any case, monitoring changes of suspicious nevi is indispensable. For an early diagnosis the patient has a very good 5-year survival prognosis of more than 95%. When a melanoma grows into depth, the risk rises dramatically making melanomas the most aggressive and deadliest skin cancer [1]. Reaching the circulatory system, the cancerous cells become able to spread to the whole body reducing the 5-year survival prognosis to less than 20%. Early diagnosis and rapid and complete surgical excision of melanomas are essential for survival as metastasized melanomas are still not curable. From this situation the need for appropriate monitoring and diagnosis tools arises improving early detection and screening of melanoma.

In the past decades there was rapid progress of non-invasive methods for skin cancer diagnostics and tumor size detection for excision margin assessment. Today, melanoma diagnostics consists of initial visual inspection and post-excisional histopathological verification. Both stages need well-trained and experienced medical staff. Histopathology can identify tumor tissue morphologically and measure the infiltration depth of the tumor, but it is invasive, time consuming and does not provide information about spatial dimensions of the lesion. In addition, this can be potentially painful for the patients. The depth of a suspicious lesion is the main criterion for determination of the appropriate safety margin for curative surgery: 1 cm for a thickness ≤ 1 mm to 2 mm and 2 cm for a thickness between 2.01 mm to 4 mm [2]. If it was possible to determine the thickness before the first excision, the number of repetitive surgeries could be reduced drastically. Thus, there is an urgent need for a fast, non-invasive, and objective technique for preoperative melanoma depth assessment, as the documented incidence of melanoma are increasing worldwide.

Several non-invasive techniques have been applied to melanoma size detection and differential diagnosis so far: high frequency ultrasound (HFUS) [3–6], as well as a variety of optical methods such as fluorescence spectrometry, Raman spectroscopy, confocal microscopy, optical coherence tomography (OCT) and reflectance spectrometry, comprehensively reviewed in [7]. Out of all these modalities, HFUS and OCT have been shown to be the most useful in depth detection, but only up to a lesion thickness of approximately 1.3 mm [8]. To be able to exceed this limit another approach is needed. The optoacoustic effect, first described by Bell in 1880 [9], combines optical contrast with acoustic (ultrasound) penetration depth. Utilizing this effect allows for tomographic imaging, and in particular non-invasive *in vivo* measurements of biological tissue making it compatible with other optical techniques like OCT.

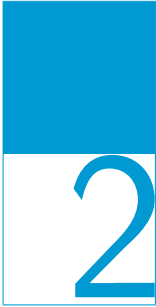
Both techniques, OCT and optoacoustics (OA), have the potential to improve preoperative planning, appropriate safety margin assessment and decision on necessity of sentinel node biopsy preventing from repetitive surgical interventions. In general, the different techniques utilized for non-invasive melanoma depth assessment so far have complimentary capabilities with regard to penetration depth, resolution or range of operation. Currently, it can be assumed that one technique alone will not be able to reliably determine the melanoma depth for a wide range of thicknesses non-invasively, and, therefore, a combination of such techniques might be a more promising route to realize such a system. However, OCT and OA are limited to detection of dimensions and morphology of a suspicious lesion. Additional measurements of pathological relevant chemical fingerprints would be beneficial.

At this point, Raman spectroscopy is used as the third modality which is currently at the stage of development as an *in vivo* technique for skin cancer diagnostics [10]. For fast *in vivo* clinical Raman screening, a relatively small hand-held Raman probe is required in order to reach skin areas on all parts of the human body. However, both *ex vivo* and *in vivo* Raman measurements have shown that detection of the Raman signal from the biological tissue is not a trivial task. The problems arising from *in vivo* use of the Raman spectroscopy for skin cancer screening and the ways to solve them have been reviewed in [11, 12]. The main obstacle for the routine clinical *in vivo* Raman skin cancer screening is an inherently low quantum yield of the Raman signal obtained upon the incident laser intensity, further limited by Maximum Permissible Exposure (MPE) requirements, resulting in low signal-to-noise ratio (SNR) of the detected Raman signals. These signals with low SNR limit the identification of the skin cancer forms, unless high power densities of the incident light are used, which exceed MPE values significantly [10].

This work is centered on OCT for thickness assessment and screening of melanocytic lesions including melanomas. First, in Chapter 2 the skin physiology and relevant skin properties are discussed to create a knowledge basis of the tissue sample under investigation. Chapter 3 presents the basics of OCT, i.e. signal generation and the principle of extracting quantitative information. Afterwards, in Chapter 4 preliminary experiments for quantitative OCT measurements of thickness, refractive index and scattering coefficient on different tissue phantoms are shown. Numerical OCT simulations described in Chapter 5 deepen the understanding of scattering in turbid media providing a model for signal degradation of OCT. A preclinical study, performed in the course of this work, is presented in Chapter 6 evaluating the performance of OCT compared to high frequency ultrasound (HFUS) and the gold standard histopathology. In Chapter 7 an improved three-dimensional segmentation algorithm for OCT lesion data is introduced. Multimodal approaches, which are compatible with OCT, and particular modifications are reviewed in Chapter 8. Finally, in Chapter 9 the findings of this work are summarized and an outlook for possible prospective work is presented.

“The future depends on what you do today.”

— Mahatma Gandhi



Chapter 2

Human skin and malignant melanoma

Skin is the largest human organ and the first and foremost interface to the environment. Covering and shielding all other organs it is a complex sensory system sensitive for various internal and external stimuli like heat, cold, pressure, roughness and many more. Human skin is able to regenerate and heal after being wounded, it also undergoes a continuous renewal and plays an important role in our body's water balance. Healthy skin is protecting us from radiation, pollution and pathogens also providing an armor against various mechanical attacks. Last but not least it is a part of the representation of our person. Considering all these points it is imperative to keep this organ intact. Skin diseases or damage may lead to a significant decrease in the quality of life or even can be life threatening. Thus, investigating human skin and possible diseases is important for medicine and the everyday life.

2.1 Skin physiology

The structure of human skin is similar to that of other mammals. It consists essentially of three layers (see Figure 2.1). The inner layer is called *subcutis* and serves as cushion consisting mainly of fat cells embedded in a loose collagen network. It contains the *Pacinian corpuscles*, which are mechanoreceptors sensitive to vibration and pressure enabling to sense roughness. Blood vessels (*arteriovenous plexus*) passing the subcutaneous tissue connect the other layers to the circulatory system and provide them with nutrients and oxygen. They reach into the *dermis*, the middle skin layer, and branch out towards the dermoepidermal junction (DEJ). The stability and flexibility of the dermis is maintained by *fibroblasts* and *fibrocytes* producing the extracellular matrix mainly consisting of collagen and elastin fibers. Starting in the deep dermis the *eccrine sweat glands* reach out to the skin surface and take care of temperature regulation. *Hair follicles*, responsible for hair production, and the hair

2 Human skin

erector muscles (*arrector pili muscles*) are also located in the dermis. The *epidermis* is the outermost skin layer responsible for absorbing radiation and shielding the deeper layers from other environmental influences, e.g. chemicals or pathogens. The dermoepidermal junction zone is determined by the *papillary dermis* and the *stratum basale* (epidermis) in a corrugated structure (*dermal papillae*) which is maximizing the surface and, thus, strengthens the conjunction of dermis and epidermis. The inner epidermal layers *stratum spinosum* and *stratum granulosum* consist mainly of *keratinocytes* which are constantly reproduced. They build up the outer epithelium layer denoted as *stratum corneum*, the 'horny layer'. The stratum basale also contains *melanocytes* producing melanin pigments. These pigments are responsible for light absorption (especially in the ultraviolet (UV)) to protect the inner layers from light induced damage. Ultraviolet light has the capability to damage the DNA and lead

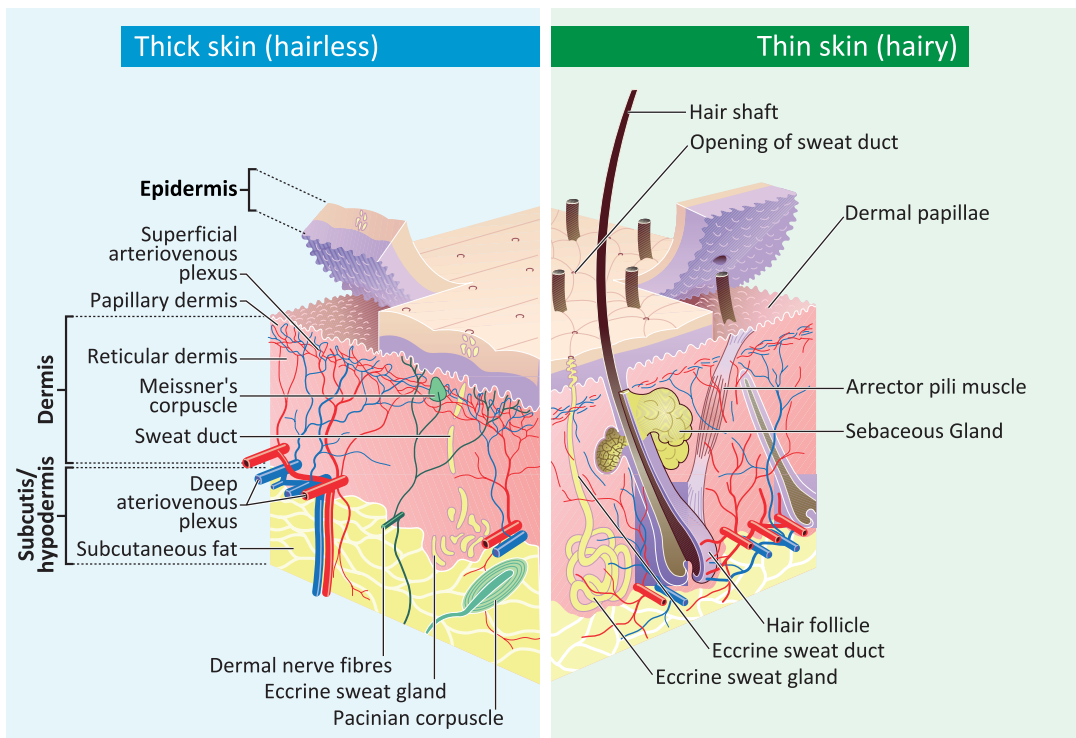


Figure 2.1: Exemplary scheme of human skin. The layers' content and thickness varies for different regions of the human body. Hairless, thick skin (hand palm, sole of the foot) has other thickness relations of the different layers and features than thin, hairy skin (most of the human body) [13].

to uncontrolled cell growth. On the one hand, protecting other cells and, on the other hand, being eminently exposed the melanocytes may degenerate as well and lead to the formation of melanomas. This growing cancer produces a change in the morphology and especially the thickness of the layer at the particular location.

This work is focused on thickness determination of melanocytic nevi in prospect to determine the skin infiltration depth of melanomas and takes advantage of the morphological change (see Chapter 4).

2.2 Optical properties of human skin

In the context of this work, understanding the optical properties of human skin tissue is crucial. Skin, in general, is a highly scattering and light absorbing medium. Various layers with different cell structures described in the previous section give rise to numerous parameters concerning scattering regimes and absorption wavelengths. Investigating those parameters enables to utilize their variation in tissue to retrieve interfaces, the morphology and even chemical changes which can be used for pathological differential diagnosis.

The investigations in this work focus onto light-tissue interaction of visible and near-infrared light. Depending on the effects to be utilized and the desired penetration depth the wavelength can be chosen. Three basic cases are important for this work: absorption where the light is transformed to inner energy of the matter, elastic scattering where only the photon's direction is changed but not its energy and inelastic scattering where both the direction and the energy of a photon are changed. These processes are described particularly with emphasis on skin in the following sections.

2.2.1 Absorption

Since it is one of the main functionalities of skin to absorb light, especially in the UV, there is always a trade-off for imaging systems, e.g. between contrast or signal intensity and depth of penetration. For example in the UV range most of the light is absorbed by the stratum corneum such that signal based on absorption or inelastic scattering is mainly limited to the according depth. In contrast, in the near-infrared (NIR) biological tissue has a so called *therapeutic window* (650 nm to 1350 nm). There the absorption is low and the dominating interaction process is scattering, which also leads to light loss. Nevertheless, the window allows for deeper penetration than light in the UV or visible (VIS).

The absorption of light in a medium is described by the Beer–Lambert law

$$I(z) = I_0 \cdot e^{-\mu_a z} \quad (2.1)$$

where I_0 is the incident intensity and z is the path length in the medium. The intensity $I(z)$ decreases exponentially with increasing propagation length. μ_a describes the attenuation due to absorption of the light denoted as absorption coefficient and can

2 Human skin

be considered as material parameter. It is possible to measure changes of μ_a and extract relevant information, by pathological means, about the skin [14]. However, the role of absorption in this work is limited. OCT (Chapter 3) is not sensitive to absorption, whereby for OA (Chapter 8.1.1) it is the main property determining the contrast (although, not used quantitatively there).

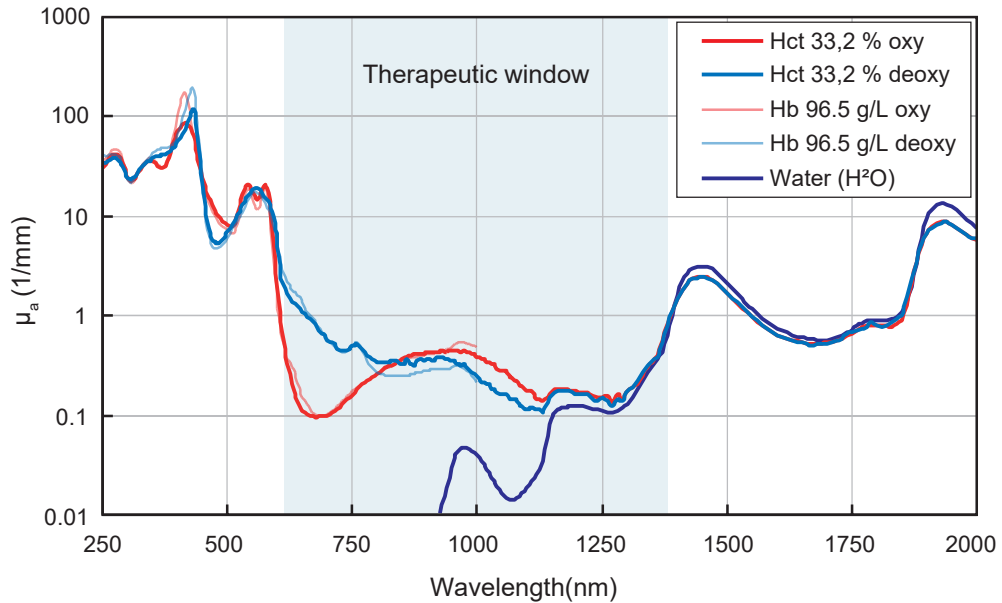


Figure 2.2: Absorption coefficient μ_a of hematocrit (Hct, blood cells), hemoglobin (Hb) and water. In the therapeutic window (blue region) the absorption has the lowest values [15].

2.2.2 Elastic scattering

Skin is a highly diffuse heterogeneous medium. In addition to absorption, elastic scattering is the main process of photons in tissue. It is naturally increasing the photons' path length and thus the absorption efficiency of the medium. Similar to Equation 2.1 the intensity decrease due to scattering can be described via Beer-Lambert law as well:

$$I(z) = I_0 \cdot e^{-\mu_s z} \quad (2.2)$$

with initial intensity I_0 and μ_s as the scattering coefficient. There are two relevant scattering regimes: Rayleigh scattering [16] and Mie scattering [17]. The latter is of major importance for this work.

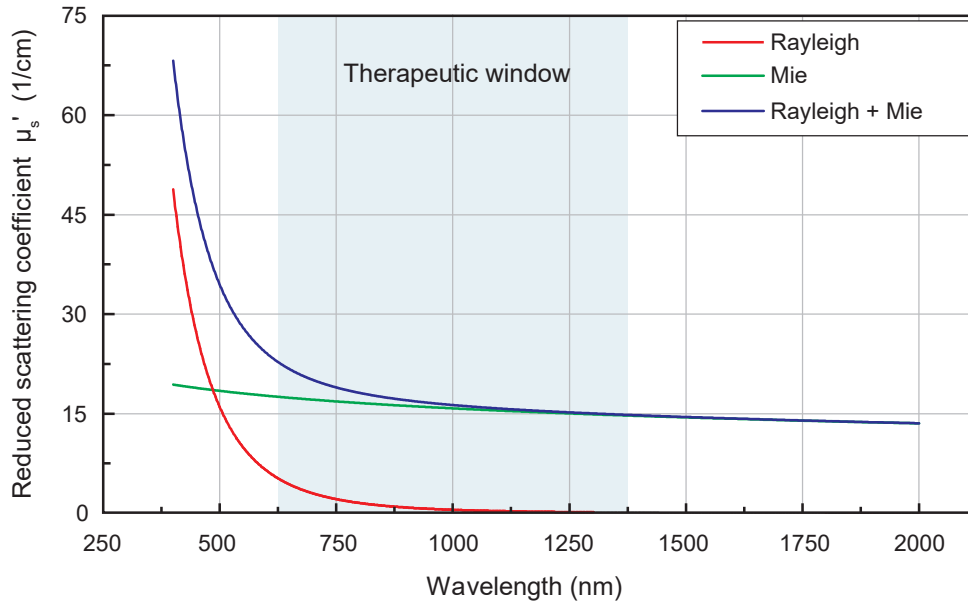


Figure 2.3: Spectral dependence of reduced scattering coefficient μ'_s of human skin (*in vitro*) [18]. In the therapeutic window (blue region) Mie scattering (green line) is the dominant process, whereas Rayleigh scattering (red line) plays a marginal role. The observed scattering is a superposition (blue line) of both processes.

Rayleigh scattering

The electromagnetic field of incident photons induces dipole moments in atoms and molecules oscillating synchronously with the light field and creating an electromagnetic wave on their own. This radiance has the same frequency and a characteristic angular dipole distribution in case of small particles compared to the wavelength ($\ll \lambda$). It is denoted as Rayleigh scattering [16]. The scattering cross-section (σ_s) of this process is proportional to $1/\lambda^4$ leading to stronger scattering of shorter wavelengths. As a visible result of this effect the sky looks blueish by day (widely spread blue light due to stronger scattering) and reddish at the evening (less scattered red light dominates). However, the assumption of particles being much smaller than the wavelength is not valid for skin tissue and visible or infrared light. Moreover, the skin structure's granularity is considered to be exactly in the range of λ .

Mie scattering

Particles with sizes of the order of the magnitude of the wavelength ($\approx \lambda$) cannot be treated as a single dipole as it is assumed in the Rayleigh theory. Instead, a multipole expansion is required. The corresponding formalism was initially developed

by Gustav Mie [17] and describes solutions of the interaction of electromagnetic plane waves with spherical objects. The size of biological cells is typically in the micrometer regime. Considering the wavelengths used in this work (1250 to 1350 nm and 532 nm) the main scattering process is Mie scattering as shown in Figure 2.3. Further formal description is given later on in Chapter 3.

Besides Rayleigh scattering for objects with a small diameter $d \ll \lambda$ and Mie scattering for $d \approx \lambda$, scattering on much larger objects ($d \gg \lambda$) is well described by geometrical optics, particularly refraction at a spherical surface.

2.2.3 Inelastic scattering

For light tissue interaction not only elastic scattering is present. In addition, inelastic scattering appears, even though with a more than three orders of magnitude smaller scattering cross section [19] compared to the elastic case. Inelastic scattering by optical means occurs due to interaction of light with the tissue molecules' rotational and vibrational states leading to an energy shift of the scattered light. This effect is referred to as Raman scattering, previously predicted by Adolf Smekal [20] and discovered in 1928 by C.V. Raman [21]. Using an excitation wavelength at (or close to) an absorption band of the medium the scattering efficiency (i.e. cross section) is enhanced by five orders of magnitude [19]. Hence, this so called resonance Raman effect is 10^5 times more effective than normal Raman scattering and has become a useful tool in spectroscopy and especially in life sciences. This work utilizes resonance Raman spectroscopy as one modality of the multimodal setup presented in Chapter 8.

2.3 Acoustic properties of human skin

Human skin is an acoustically dense medium and thus the attenuation of acoustic waves propagating in the tissue is small (e.g. compared to air). This allows for measuring acoustic signals on the skin surface even if they are originating from deep tissue. In dermatology high frequency ultrasound is used to produce cross-sectional images of the skin structure. The speed of sound in skin highly depends on water content and collagen concentration and is in the range of 1550 m s^{-1} to 1600 m s^{-1} . An increased collagen fraction leads to higher sound velocity whereas high water content reduces the velocity [22]. There is not only a frequency dependence of the speed of sound but also of the penetration depth. The higher the frequency the more sound is absorbed by the medium leading to significant signal loss. Ultrasound devices for skin imaging differ in the frequency of the applied sound. E.g. for 20 MHz devices the penetration depth in skin is about 6 – 10 mm whereas for 100 MHz HFUS used in this work the depth is effectively limited to 1.5 – 2.5 mm.

While for OCT the optical properties are important (see Chapter 3) and for HFUS only acoustic properties are relevant (see Chapter 6) optoacoustics utilizes both light absorption and sound propagation (described in Chapter 8.1.1).

2.4 Malignant melanoma

The malignant melanoma is the most dangerous skin cancer type. In 2012 about 232,000 people developed a melanoma and 55,000 people died from black skin cancer worldwide [23]. In Germany 10,500 women and 10,900 men developed melanomas and about 3,000 died in 2013 [24]. At that time almost 100,000 Germans lived with the diagnosis made in the past five years. And still this trend is rising, especially in regions with predominantly Caucasian skin type. In most cases melanomas develop from benign melanocytic nevi. This preliminary stage is modified by mutation of melanocytes leading to an uncontrolled mitosis and tumor growth. In later stages the cancer cells may spread to other organs leading to massive destruction and in the worst case to organ failure and death.

2.4.1 Dermatological classification criteria

Melanomas if discovered at early stages can be treated very well. A preterm removal of the cancerous tissue increases the chances of a complete cure significantly (up to 99% if detected in the early, so called first stage). Therefore, regular screening of suspicious nevi is required. The ABCDE rule was established as a tool to classify nevi (see Figure 2.4) [25]. This rule facilitates finding candidate moles for further investigation. If at least two criteria match, the mole is treated as a possible melanoma and should be removed to be on the safe side. The classification of nevi and the ABCDE rule are

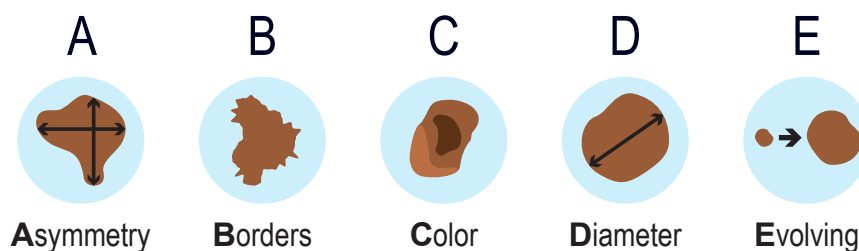


Figure 2.4: Illustration of the ABCDE criteria for melanomas. If one or more criteria match to the lesion it is advised to make an appointment with a physician.

based on examination by eye or dermatoscope lacking for thickness evaluation. Once a suspicious lesion is found and excised its infiltration depth is most important for the risk evaluation. Depending on the thickness classification the medical treatment is chosen. If the biopsy is positive for melanoma and the histologically measured

thickness is of certain magnitude an additional excision might be needed to preserve safety margins to minimize the risk of metastatic spread. The more a melanoma has infiltrated the skin the higher is the probability to spread mutated cells to the lymphatic or cardiovascular system (see Figure 2.5). Considering these aspects a

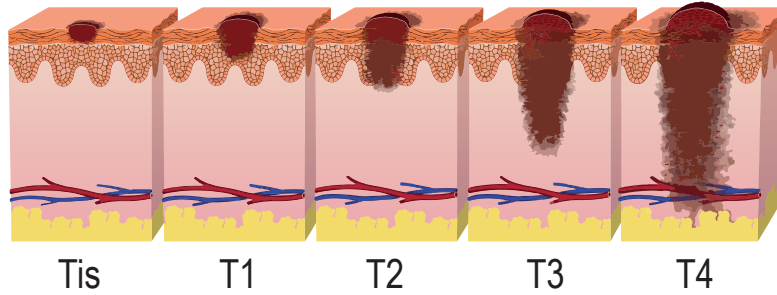


Figure 2.5: Different melanoma stages, inspired by [26].

staging and notation system was developed by the *Union for International Cancer Control* (UICC): the *TNM Classification of Malignant Tumors* [27]. The first letter T describes the tumor size and the tissue invasion, the second letter N shows if the nearby lymph nodes are involved and the third letter M denotes if distant metastasis are present. For the purpose of this work only the tumor size, particularly its thickness, and the tissue invasion is relevant. In Table 2.1 the classification scheme for the melanoma thickness (T parameter) is presented.

Table 2.1: T parameter classification of melanoma, corresponding thickness and recommended surgical excision safety margins [23].

Class	Thickness	Margins
Tis	In situ melanoma. No invasion of the dermis.	5 mm
T1	≤ 1 mm	10 mm
T2	1.01 – 2 mm	10 mm
T3	2.01 – 4 mm	20 mm
T4	> 4 mm	20 mm

“Imagination is more important than knowledge.”

— Albert Einstein



Chapter 3

Optical coherence tomography on scattering media

3 OCT

Optical coherence tomography (OCT) is in the focus of this work which aims at the development of multimodal approach including OA and Raman spectroscopy (see Chapter 8) applied on human skin. Since skin is a diverse, highly scattering medium the investigation of the behavior and signal generation of OCT in such media is crucial. Due to the complexity of skin it is convenient to study simpler samples with well-known parameters first. This chapter gives an overview of relevant OCT techniques available and inherent principles needed herein. Also, the fundamental theory of signal generation is provided. Finally, different characteristics such as typical distortions and sensitivity roll-off of OCT measurements are discussed.

3.1 Types and Principles of OCT

OCT is based on white or at least broadband light interferometry also called low coherence interferometry. There are different OCT techniques where the most comprehensible is time domain optical coherence tomography (TD-OCT) (see Chapter 3.1.1). The less intuitive frequency domain optical coherence tomography (FD-OCT) can be divided in two groups depending on the information encoding of the signal: spatially and time encoded FD-OCT. The spatially encoded spectral domain optical coherence tomography (SD-OCT) uses a broadband light source similar to TD-OCT and is explained in Chapter 3.1.2. Since the Fourier transformation plays an important role, often the unsystematic denotation Fourier domain OCT is used for SD-OCT. The time encoded types of FD-OCT do not use broadband light but tuned narrow-band sources as for swept source optical coherence tomography (SS-OCT) (see Chapter 3.1.3).

All OCT techniques are distinguished mainly by the domain of the signal encoding and the light source and have in common that light is split into a reference beam and

a sample beam. The reference beam is reflected from a mirror whereas the sample beam is reflected from different layers of the structured specimen under investigation. Reflection is caused by interfaces between layers with different refractive indices following the Fresnel conditions. In the returned sample beam probing one particular spot, the structure is encoded as a superposition of phase shifts generated by varying propagation lengths. By combining the sample beam with the reference beam (correlating both beams), only the light interferes where the difference of the optical path lengths between object and reference beam falls within the coherence length of the light source.

The penetration depth of the sample beam only depends on the center wavelength, the corresponding light absorption and scattering properties of the specimen. The axial (depth) resolution depends on the coherence gate and thus on the bandwidth of the light source: the higher the bandwidth is, the smaller is the coherence gate and the higher is the resolution. Note that there is also a dependence on the mechanical parts or the detector described in the next sections.

3.1.1 Time domain OCT

TD-OCT was the first established OCT technique. It is based on the translation of the reference mirror to measure different depth intervals. The principle of this low coherence interferometric technique is depicted in Figure 3.1. The movement of the mirror is encoded by time as well as the signal of the photo detector. Hence, it is possible to measure the time evolution of the correlation by continuously measuring the intensity of the interference, e.g. at the center of the ring-shaped interference pattern (zeroth order).

The resulting signal is an intensity modulation over time (see Figure 3.2). The shape of the envelope of this oscillation corresponds to the depth profile since every point of the intensity signal has a corresponding mirror position. Considering an infinitesimally thin boundary (e.g. a mirror surface) both, the intensity signal and the envelope, become quite simple shapes. In Figure 3.2 such an exemplary intensity modulation is shown. In case of infinitesimally thin boundaries the full width at half maximum (FWHM) of the envelope corresponds to the coherence length l_c of the light source:

$$l_c = \frac{2 \ln(2)}{\pi} \cdot \frac{\lambda_0^2}{\Delta\lambda} \quad (3.1)$$

where λ_0 is the center wavelength and $\Delta\lambda$ is the bandwidth of the laser light source. However, the signal response to an infinitesimal boundary is broadened. This particular signal broadening is referred to as axial point spread function (APSF) and will be discussed in another context later on in Chapter 3.2. Note that only

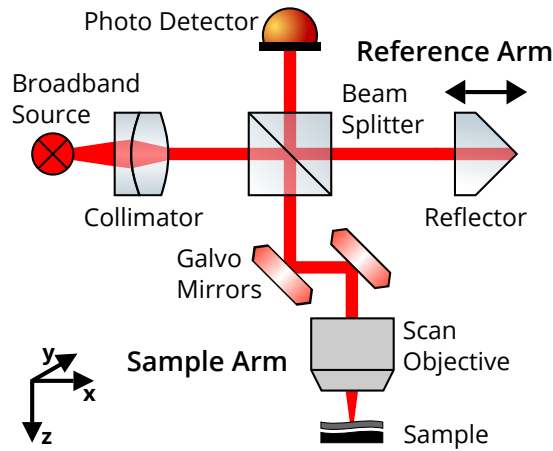


Figure 3.1: Sketch of a typical scanning time domain OCT system. A broadband light source is split into a reference beam with a variable length and a sample beam (z-direction). A galvanometer based scanning system allows for 2-D and 3-D imaging (x-y-plane). Both reflected beams are cross-correlated at the photo detector measuring the center of the ring-shaped interference pattern.

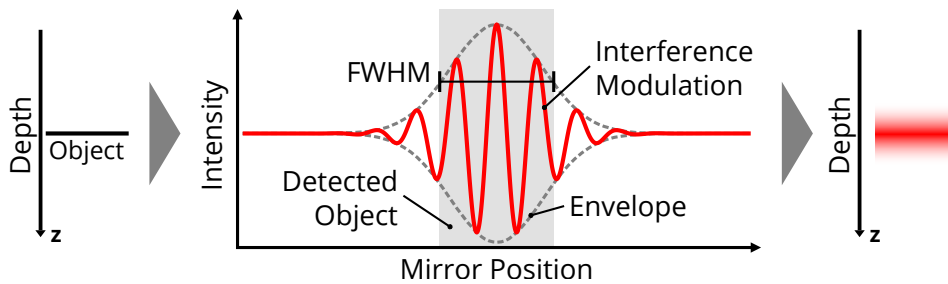


Figure 3.2: Sketch of typical time domain OCT signal. An infinitesimally thin interface (left-hand side) is measured in z-direction. The detected signal (middle plot) is an intensity modulation (red curve). The FWHM of the envelope (gray dashed line) corresponds to the coherence length of the light source l_c . The detected interface, which is located at a certain depth is represented by the light gray box with a finite thickness. On the right-hand side the broadened image of the object is shown.

light from within the coherence gate contributes to the signal leading to a low SNR compared to other OCT techniques where the whole spectrum carries the signal (e.g. SD-OCT) [28]. Beside the dependence on the source properties mentioned above the accuracy of the mechanical translation of the reference reflector is limiting the depth precision. Even by using fast piezoelectric mirror devices the speed of a depth scan is very limited. In particular this is relevant for cross-sectional or volumetric imaging where the sample beam is moved via additional galvanometric scanning mirrors. There, the scanning time is raised to the power of two or three,

respectively, compared to one-dimensional depth profile measurements. Nevertheless, for non-living or non-moving specimen, where short measurement time is not crucial, this technique still offers good results.

3.1.2 Spectral domain OCT

Spectral domain optical coherence tomography (SD-OCT) uses spectral information of light to retrieve the depth profile and reconstruct a tomogram. Therefore, a spatial decomposition of this light is necessary and provided by a spectrometer consisting of a prism or a grating and a linear CCD array camera (see Figure 3.3). With this configuration no moving reference reflector is needed and only the scanning system, if available, has moving mechanical parts like galvanometer-driven scanning mirrors (Galvo Mirrors). Interference patterns directly depend on the frequency

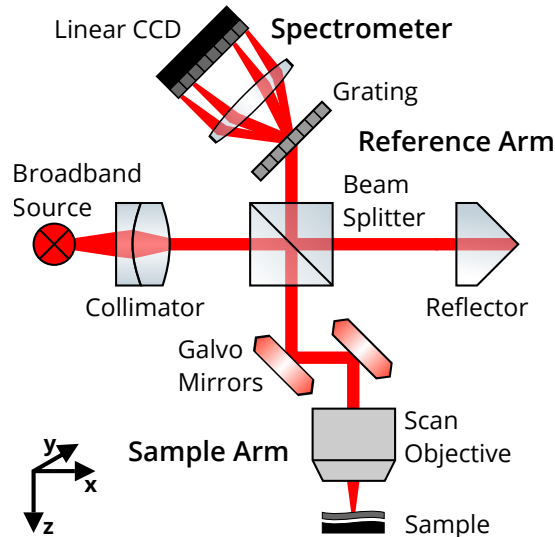


Figure 3.3: Sketch of a typical scanning spectral domain OCT system. A broadband light source is split into a reference beam and a sample beam (z-direction). A galvanometer based scanning system allows for 2-D and 3-D imaging (x-y-plane). The cross-correlated beam is spectrally analyzed by a spectrometer (grating and a linear CCD array).

(or wavelength) of the light. Thus, considering a broadband light source, multiple patterns are present for different frequencies corresponding to different depths. This fact is used for spectral domain OCT. The intensity of each frequency component is modulated by depth according to the particular phase shift and coherence. This is equivalent to a spectral modulation of the source spectrum as the Wiener–Khinchin theorem demonstrates [29]: the power spectrum of the signal is the Fourier transform of the autocorrelation of this signal and vice versa. The spectral modulation frequency

depends on the depth. The deeper the reflecting object or the larger the distance between reference mirror and sample reflector is, the higher is the modulation in the frequency domain. In Figure 3.4 such a modulation of the source spectrum is presented. The signal shape is given by Equation 3.2 and is thoroughly described in

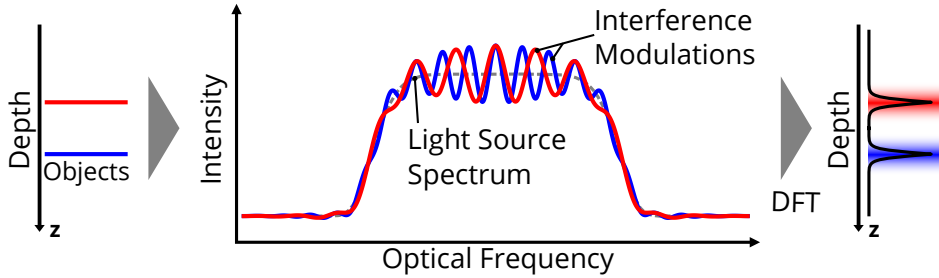


Figure 3.4: Sketch of a typical frequency domain OCT signal. Two infinitesimally thin interfaces are measured in z -direction. The detected signal (middle plot) is a superposition of intensity modulations (red and blue curve) on top of the source spectrum (gray dashed line). Each reflection at a particular depth produces a modulation of a corresponding frequency. Different components of the superposition are decomposed via a discrete Fourier transform (DFT) and produce the depth profile (right plot).

Chapter 3.2 (see Equation 3.8).

$$I_D(k) = \frac{\rho}{2} \left[S(k) \sum_{n=1}^N \sqrt{R_R R_{S_n}} (\cos [2k (z_R - z_{S_n})]) \right] \quad (3.2)$$

Faster spectrometers and higher computational power are improving SD-OCT more and more. For volumetric imaging the spectrometer is limiting the imaging speed and thus the field of view. There is a trade-off between imaging speed and sensitivity: The faster the scan is, the less light is collected for each particular measurement point and the lower the spectral intensity is projected on the CCD. This is an important drawback especially in biomedical *in vivo* imaging where motion artifacts are to be avoided by faster scanning. However, there are different approaches to overcome these limitations (e.g. using multiple spectrometers [30] or parallelization as in Chapter 3.1.4) and faster detectors are developed giving SD-OCT a viable future.

3.1.3 Swept-source OCT

Unlike the spectrally encoded SD-OCT signal, the SS-OCT signal is sequentially obtained, and thus time encoded. Instead of using a broadband light source a tunable monochromatic light source with a small bandwidth is used [28, 31]. It is tuned over a similar frequency range compared to the bandwidth of SD-OCT producing the according coherence gate for interference signal generation. Figure 3.5 shows

3 Optical coherence tomography on scattering media

an SS-OCT setup which is very similar to TD-OCT, however, there are no moving parts (except the scanning mirrors) and the light source is different. Different layer

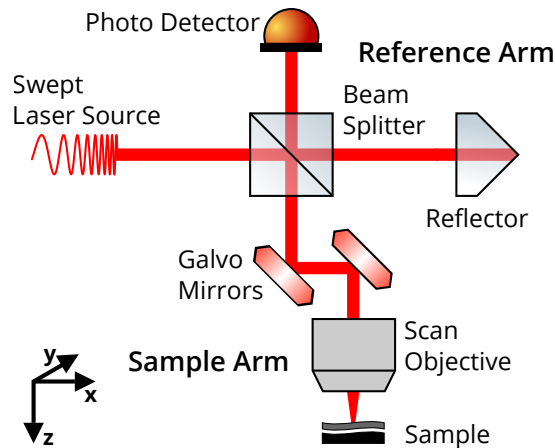


Figure 3.5: Sketch of a typical scanning swept source OCT system. A swept laser light source is split into a reference beam and a sample beam (z-direction). A galvanometer based scanning system allows for 2-D and 3-D imaging (x-y-plane). Both reflected beams are cross-correlated at the fast photo detector recording the time evolution of the intensity signal.

depths produce various time shifts and point to specific sweep states of the laser source. Through interference with the reference beam a beat signature with specific frequencies and amplitudes occurs. The modulated intensity signal is measured as for TD-OCT with a single photo diode recording the signal time evolution. The diode has to be fast enough to resolve the frequency sweep of the source sufficiently. Similar to SD-OCT the frequency components of the beat signature (envelope of intensity $|E_1 + E_2|^2$) correspond to the interfaces of the sample. The low-pass filtered beats of different successive frequency steps are combined and after a discrete Fourier transform a depth profile is obtained.

With the use of a swept source laser a high SNR is achieved because the spectral intensity is larger than for SD-OCT. This results in a higher sensitivity for greater depths. However, the influence of non-linear media leading to a broadening of the sweeping pulse frequency potentially distorts the measurement. As an interferometric technique, the system is very phase sensitive. Hence, wavelength and phase stability of the sweeping laser source is crucial. Phase fluctuations induced by the source lead to additional decorrelation of the signal. Movements of the specimen on small scales (sub-wavelength) can produce image artifacts as well [32]. There are various methods to counter-act these drawbacks, e.g. better post-processing, making SS-OCT to a good working and still very promising technique. New laser sources like Fourier domain mode-locked lasers were recently implemented in biomedical imaging

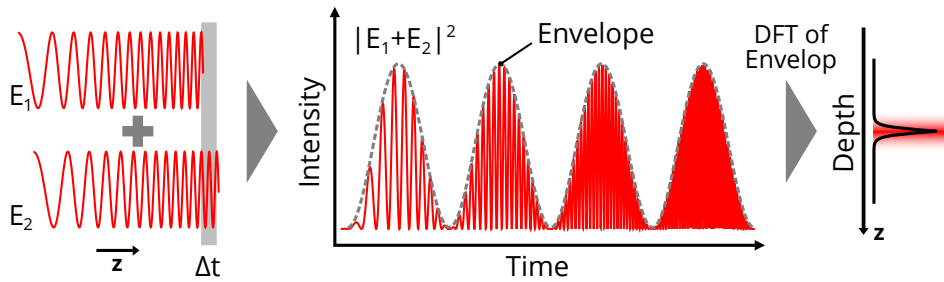


Figure 3.6: Sketch of a typical scanning swept source OCT signal. The reflected reference field E_1 and the reflected, time delayed sample field E_2 interfere on the detector. The time evolution of the interference of the swept fields (red curve) has a beat signature over time (envelope, gray dashed line). An infinitesimally thin interface produces a sinusoidal beat with a specific frequency. A DFT provides the sample's depth profile.

providing very high sweeping speed [33]. This allows for very fast imaging and larger field of views. With higher computational power also the (post-)processing becomes increasingly better making SS-OCT evolve to a great volumetric imaging system.

3.1.4 Other OCT types

The former presented techniques all have drawbacks and limitations especially concerning the scanning speed or image acquisition time for 2-D or 3-D images. Most attempts to overcome these limitations are modifications of the previously mentioned systems with a parallelization component. In the following a few approaches are outlined. A more detailed review of different techniques is presented in [34].

Line-field OCT

Line-field OCT is applicable for both time domain and spectral domain OCT (LF-TD-OCT, LF-SD-OCT). In case of SD-OCT, the technique is extended by a 2-D CCD array instead of a one dimensional line array. One dimension of the array is for acquisition of the interference signal (depth profile), the other for lateral resolution. A cylindrical lens shapes a line producing an x - z cross-sectional image [35]. A big advantage is the instantaneous acquisition of a tomographic image without a scanning system. In case of TD-OCT a reflective grating in a Littrow configuration is used as reference mirror, providing the time encoding of the signal due to the phase differences of the blazed grating. The interference pattern of the grating and the back-reflected light from the sample interfere on a 2-D CCD array. This interference, which in one dimension encodes the depth profile and in the other dimension resolves the lateral structure, is modulated by a piezoelectric actuator mounted on the grating

to shift the phase between the two sequential interference images, thus removing motion artifacts [36]. In both cases a cylindrical lens produces a scan line and a scanning mirror moves the line in an additional direction allowing for 3-D imaging.

Full-field time domain OCT

Also denoted as full-field optical coherence microscopy, full-field time domain optical coherence tomography (FF-TD-OCT) is a combination of conventional *en face* microscopy providing high lateral resolution and TD-OCT for in-depth signal. A phase modulator (e.g. an oscillating reference mirror or a photoelastic modulator) together with lock-in detection of the modulated signal allow for a direct 2-D *en face* signal measurement without scanning [37]. The sample is mapped to the CCD sensor surface where each CCD pixel corresponds to lateral sample coordinates and can be considered as a single TD-OCT detector. All pixels together produce a two-dimensional image comparable to conventional microscopy. The depth scan is obtained by moving the sample axially in z-direction (or the offset of the reference mirror) measuring successively *en face* images of the x-y plane producing a volumetric image. With this approach cellular lateral resolution is possible at the cost of field of view. This is particularly useful if cellular resolution and higher penetration is required than possible with conventional microscopy.

Full-field swept-source OCT

Similar to FF-TD-OCT the full-field swept-source OCT (FF-SS-OCT) is a combination of confocal microscopy and SS-OCT for in-depth data acquisition. As for SS-OCT a frequency-swept laser is used as light source. Instead of using a photo detector as in Chapter 3.1.3 an ultrahigh-speed 2-D camera is used. Two identical objectives are implemented in reference and sample arm to image the specimen correctly on the detector [38]. This technique is the current state-of-the-art by means of full-field OCT.

In this work only the SD-OCT technique was used. The overview of different mentioned types and their principles is useful for orientation and to pinpoint the following descriptions and the theoretical part.

3.2 Theory of spectral domain OCT signal generation

This section gives an introduction to the theory of OCT signal generation which is required for understanding the processing of experimental data obtained in this work. The present elaboration is centered on spectral domain OCT since this is the technique the OCT measurements presented in the following chapters are acquired with. However, a major part of the shown theory is applicable for other OCT techniques in a similar way. The theory is used to remove effects such as the influence of the confocal point spread function (CPSF) and to retrieve the scattering coefficient μ_s of homogeneous samples as presented in Chapter 4.

Since OCT is an interferometric technique the signal can be described as an autocorrelation of the sample and the reference beam. In Figure 3.7 the according electrical fields are sketched. The input electric field strength E described with

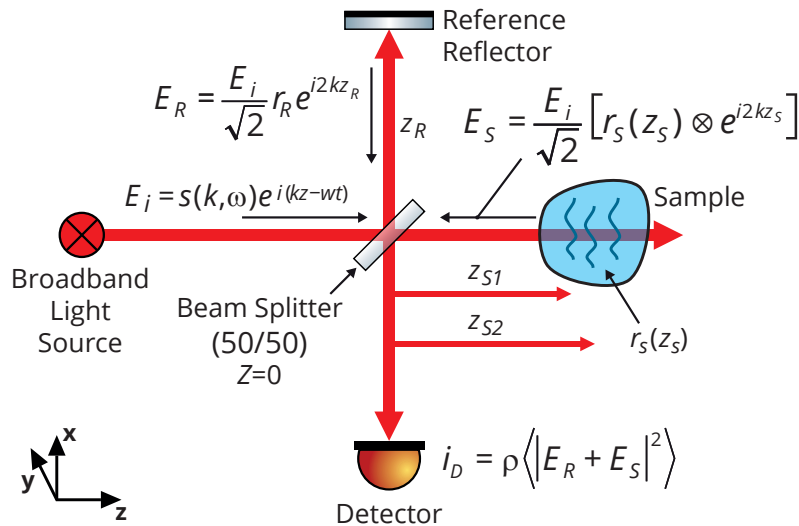


Figure 3.7: Scheme of the field propagation in a typical SD-OCT system. The sample beam (z -axis) and the reference beam (x -axis) interfere through the combination via the beam splitter. The measured detector signal intensity i_D corresponds to the interference intensity of the reference field E_R and the sample field E_S [39].

the general expression $E_i = s(k, \omega) e^{i(kz - \omega t)}$ is coupled into the interferometric setup. $s(k, \omega)$ is the spectrally resolved electric field amplitude, the argument $k = 2\pi/\lambda$ is the wavenumber, and $\omega = 2\pi\nu$ is the angular frequency. The latter two are coupled by the dispersion relation

$$\omega = \frac{c}{n(\omega)} k \quad \text{or} \quad \nu = \frac{c}{n(\lambda)} \lambda^{-1} \quad (3.3)$$

3 Optical coherence tomography on scattering media

where $n(\lambda)$ is the material specific dispersion (wavelength dependent refractive index). Assuming a perfect beam splitter the field is divided in two equal parts that are modified differently. One is influenced by the reference mirror with the field reflectivity r_R and a phase shift e^{i2kz_R} due to the geometrical path length of the reference arm z_R . The same applies to the sample arm, except that the specimen can be considered as an assembly of many reflectors S_n , each providing its own field reflectivity r_{S_n} and path length z_{S_n} . As a result, the reflected field is given as the sum of all n partial fields or as convolution (here denoted by \otimes) of the reflector structure and the incident field:

$$E_S = \frac{E_i}{\sqrt{2}} \sum_{n=1}^N r_{S_n} e^{i2kz_{S_n}} = \frac{E_i}{\sqrt{2}} [r_S(z_S) \otimes e^{i2kz_S}]. \quad (3.4)$$

In case of a simple photo detector as in Figure 3.7 the detector signal i_D is the time average (also denoted as expectation value indicated by $\langle \rangle$) of the squared sum of both electric field amplitudes $\langle |E_R + E_S|^2 \rangle$ scaled by the detector responsivity ρ . However, for SD-OCT (see Chapter 3.1.2) not the intensity is measured but an intensity spectrum $I_D(k, \omega)$ with

$$I_D(k, \omega) = \frac{\rho}{2} \left\langle \left| \frac{s(k, \omega)}{\sqrt{2}} r_R e^{i(2kz_R - \omega t)} + \frac{s(k, \omega)}{\sqrt{2}} \sum_{n=1}^N r_{S_n} e^{i(2kz_{S_n} - \omega t)} \right|^2 \right\rangle \quad (3.5)$$

where the sample depth profile is encoded in the spectrum of the interference signal as field reflectivity profile (of all n reflectors) $r_{S_n}(z_{S_n})$. The expression in Equation 3.5 using the power spectrum $S(k) = \langle |s(k, \omega)|^2 \rangle$, the power reflectivities $R_R = |r_R|^2$ (reference arm) and $R_{S_n} = |r_{S_n}|^2$ (sample arm) is evaluated. The fast oscillating terms are neglected since generally they are much faster than the detector response time and thus are not contributing to the OCT signal (similar to the rotating wave approximation). With this, the power spectrum gets the following shape consisting of three terms [39]:

$$\begin{aligned} I_D(k) &= \frac{\rho}{4} \left[S(k) \left(R_R + \sum_{n=1}^N R_{S_n} \right) \right] && \text{"DC Term"} \\ &+ \frac{\rho}{2} \left[S(k) \sum_{n=1}^N \sqrt{R_R R_{S_n}} (\cos [2k(z_R - z_{S_n})]) \right] && \text{"Cross-correlation Term"} \\ &+ \frac{\rho}{4} \left[S(k) \sum_{n \neq m=1}^N \sqrt{R_{S_n} R_{S_m}} (\cos [2k(z_{S_n} - z_{S_m})]) \right] && \text{"Autocorrelation Term"} \end{aligned} \quad (3.6)$$

The first component, the DC terms, gives an offset based on the undistorted source spectrum $S(k)$ only scaled by the reflectivities of reference reflector and sample. The autocorrelation term, in this case, represents the speckle interference of different reflectors of the sample. For OCT the most relevant component is the cross-correlation term. For all three terms the original source spectrum $S(k)$ is modified to the resulting interference spectrum $I_D(k)$ carrying the relevant sample information. Note that k is a spectral coordinate which corresponds to the wavelength of the light or the wavenumber, respectively. In case of a spectrometer with a linear CCD array k is discrete and each value corresponds to one CCD pixel. $S(k)$ can also be described as the Fourier transform of the coherence function $\gamma(z)$ which is a property of the light source. In case of a coherence function with a Gaussian shape, according to [39] and the Wiener–Khinchin theorem [29], the following rule applies:

$$S(k) = \frac{1}{\Delta k \sqrt{\pi}} e^{-\left[\frac{(k-k_0)}{\Delta k}\right]^2} \xleftrightarrow{\mathcal{F}} \gamma(z) = e^{-z^2 \Delta k^2} \quad (3.7)$$

Here, Δk is the half width of the light source spectrum at $1/e$ of the maximum. This relation is light source specific and has a different form for non-Gaussian sources. In reality the shape of a broadband light source (e.g. a superluminescent diode (SLD)) is not necessarily Gaussian and the transformation is more complex. However, with Δk as the spectral bandwidth this relation is a sufficient approximation for most broadband light sources.

Assuming a good adjustment of the reference intensity with respect to the sample intensity level, which minimizes the DC-term, and a small autocorrelation, the cross-correlation terms can be considered as solely contributing to the OCT signal:

$$I_D(k) = \frac{\rho}{2} \left[S(k) \sum_{n=1}^N \sqrt{R_R R_{S_n}} (\cos [2k (z_R - z_{S_n})]) \right] \quad (3.8)$$

This is valid because the magnitudes of the DC and autocorrelation terms can be tuned by choosing the right reference power. The power reflectivities of the sample scatterers are typically much smaller than the reflectivity of the reference mirror ($R_{S_n} \ll R_R$) such that the auto-correlation in our system is weak compared to the interferometric cross-correlation. The typically large DC terms only give a signal offset and do not contribute to the change of the signal slope which is of interest here. Equation 3.8 is the acquired spectrum at one point of the specimen considering the interferometric field propagation. To acquire the desired depth (or reflectivity) profile $R_S(z_S)$ from the single reflector signals R_{S_n} an inverse Fourier transform of

3 Optical coherence tomography on scattering media

$I_D(k)$ is required. Considering the discrete transform

$$\sqrt{R_s(z_S)} = \sum_{n=1}^N \sqrt{R_{S_n}} \delta(z_S - z_{S_n}) \quad (3.9)$$

where the summation index n , again, refers to the different scatterers, the Fourier transform of Equation 3.8, according to [39], becomes

$$I_D(k) \stackrel{\mathcal{F}}{\Leftrightarrow} i_D(z_S) = \frac{\rho}{4} \sqrt{R_R R_S(z_S)} \{ \gamma [2(z_R - z_S)] + \gamma [-2(z_R - z_S)] \} \quad (3.10)$$

Since OCT is only sensitive to relative distance between reference and sample it is convenient to substitute the path length difference $z_R - z_S$ by Δz . Furthermore, the reference reflector is considered as perfect ($R_R = 1$). One then obtains:

$$i_D(\Delta z) = \frac{\rho}{4} \sqrt{R_S(\Delta z)} [\gamma (2\Delta z) + \gamma (-2\Delta z)] \quad (3.11)$$

Using the relation of Equation 3.7 the expression is modified to

$$i_D(\Delta z) = \frac{\rho}{2} \sqrt{R_S(\Delta z)} e^{-4\Delta z^2 \Delta k^2} \quad (3.12)$$

Indeed, Equation 3.12 gives good access to the real depth profile of the sample represented by the power reflectivity profile R_S . This relation of the reflectivity and the measured OCT signal can be used to fit the processed data $i_D(\Delta z)$ and retrieve the sample structure encoded in R_S . But there is also an influence of the optical imaging system, in particular the scanning lens focusing the parallel beam on the specimen. This leads to an axial photon density distribution given by the Gaussian beam shape and its transverse intensity profile, which especially in low concentration media cannot be neglected. The transverse Gaussian profile is given by

$$w(z_S) = w_0 \sqrt{\left(\frac{z_S - z_f}{z_i} \right)^2 + 1} \quad (3.13)$$

The lens optics of the OCT probe determine the focal point z_f and the Rayleigh length z_i . z_S is the imaged sample depth or the axial coordinate on the optical axis, respectively, and $w_0^2 = \frac{\lambda}{\pi} z_i$ is the beam waist. It has been shown that for a confocal OCT system the confocal point spread function (CPSF) can be defined from the optical properties of the objective [40] as:

$$h(d) = \left[\frac{w_0}{w(z_S)} \right]^2 = \left[\left(\frac{d}{z_i} \right)^2 + 1 \right]^{-1} \quad (3.14)$$

with $d = z_s - z_f$ being the effective distance between the focal point and the axial coordinate of the signal. For a homogeneous purely scattering medium such as milk, as was also used in this work, the modified axial reflectivity profile $R_S(\Delta z)$ can be written as convolution:

$$R_S(\Delta z) = h(d) e^{-2\mu_s \Delta z} \quad (3.15)$$

where $h(d)$ is the CPSF (Equation 3.14), which describes the influence of the imaging optics on the detected signal and $\exp(-2\mu_s \Delta z)$ represents the OCT signal decay due to scattering according to the Beer-Lambert law (see Equation 2.2). The factor 2 in the power of the exponent accounts for the fact that the photon travels the double distance within the sample with the result that the optical path length is $2\Delta z$ where the scattering coefficient μ_s takes effect. By substituting $\hat{z} = 2\Delta z$ the double photon path is removed for better comparison. Rewriting Equation 3.12 by using Equations 3.15 and 3.14 one obtains a mathematical description of an OCT measurement:

$$i_D(\hat{z}) = \underbrace{\frac{\rho}{2}}_{\text{Profile}} \cdot \underbrace{e^{-\mu_s \hat{z}}}_{\text{PSF}} \cdot \underbrace{\left[\frac{(\hat{z} - z_f)^2}{z_i} + 1 \right]^{-1/2}}_{\text{CPSF}} \quad (3.16)$$

Since the signal offset is not relevant for determination of μ_s , it can be neglected. In the measurement data the offset is mainly determined by averaging and signal noise, such that for weakly scattering media the offset is larger than for strongly scattering media. Even the DC terms and the autocorrelation terms possibly contribute to this offset. As shown in Figure 3.8 (top), good agreement between experimental and theoretical data can be achieved by applying Equation 3.16 as a fit function for data of a homogeneous measurement sample (see Chapter 4).

The scattering coefficient μ_s , the Rayleigh length z_i and the focus position z_f can be used as fit parameters. Hence, μ_s can directly be determined from the fitted exponential decay term in Equation 3.16, which acts as deconvolution with the CPSF. By placing the focus at the end of the field of view (axial shift of the sample) the focal convolution is only relevant in the low scattering regime where the photon reflection is mainly of specular kind. Note, that in scattering media, the actual beam extent does not necessarily correspond to the free space Rayleigh length. Rather, due to diffuse reflection, the parameter becomes twice the free space Rayleigh length, i.e. $2z_i$, as has been pointed out in [41]. However, as z_i is a free parameter of the fit, the beam broadening due to scattering is included in the OCT signal fit. In the bottom panel of Figure 3.8 the same data after deconvolution with the CPSF, i.e. after elimination of the beam focus contribution, is shown. For all further OCT measurement data presented in this work, this fit function was used or, at least if

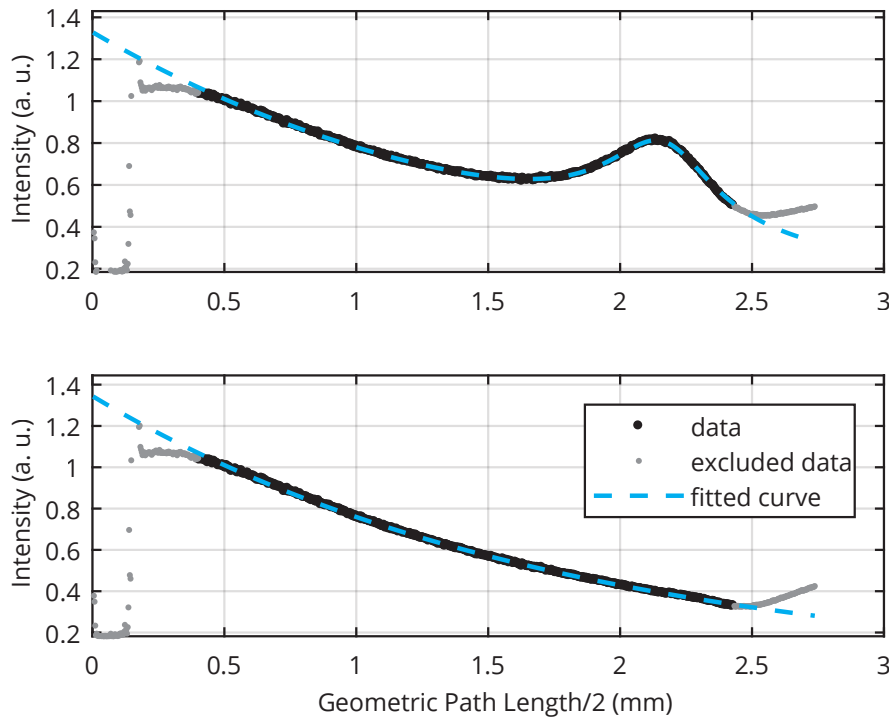


Figure 3.8: Fit of normalized measured data of 10% milk concentration including focal contribution (top) and with deconvolved CPSF (bottom). The fitting curve is marked as cyan dashed line. Due to artifacts the first and the last data points are excluded from the evaluation (gray).

necessary, a deconvolution with the CPSF was carried out.

Although the effective μ_s is obtained by fitting of the data, it is not possible to quantify its non-linear dependence on milk concentration. This, however, can be investigated by simulations, as explained in Chapter 5.

3.3 Characteristics of optical coherence tomography measurements

The previously described transverse depth profile acquired at one point of the sample is called amplitude scan or *A-scan*. In case of scanning or parallelization as described in Chapter 3.1 it is possible to acquire cross-sectional images, so called brightness scans or *B-scans* (see Figure 3.9). These are at least 2-D intensity maps of multiple *A-scans* widely used in medical applications. With full-field optical coherence tomography (FF-OCT) or two-dimensional scanning a 3-D point cloud is

produced with an intensity value at each point in a volumetric segment. This *C-scan* can be considered as a concatenation of B-scans as shown in Figure 3.10.

As an example in Figure 3.9 an A-scan (left) and a B-scan (right) of a thumbnail are shown. The solid cyan line points to the slice corresponding to the presented A-scan. Also, some intensity peaks of the A-scan are linked to the B-scan by a dashed cyan line. The signal intensity of the reflectivity profile is expressed in the logarithmic unit Decibel (dB), which is convenient for imaging.

3.3.1 Image distortions and measurement artifacts

Imaging has always limitations determined by the measurement technique, the setup and the specimen under investigation. For example: limited resolution causes blurring of edges, discrete Fourier transformations produce artifacts, and electrical noise of the photo detector's CCD leads to signal noise. By looking at the A- and B-scan in Figure 3.9 the question arises which image distortions are present and how to counteract them. In the following the most important distortions are discussed.

Noise and grain

In the left part of Figure 3.9 the original signal of the A-scan (gray curve) has a significant noise level leading to a grain distortion in the B-scan. The black curve is the smoothed signal serving as guide to the eye. Noise highly depends on the sample characteristics and is produced by different scattering objects or inhomogeneities. This is only natural since OCT is sensitive to backscattering. To reduce the noise and improve the SNR longer integration times are required (assuming the sample is not moved). For material checks this is viable, whereas for *in vivo* measurements in the life sciences there are limitations of total exposure and the patient's convenience. Hence, the setup components have to be chosen accordingly to meet the requirements of the application.

Interference and transformation artifacts

Interference is the key principle of OCT, but some effects are able to distort the pattern. For highly reflecting, plane compositions like air-glass interfaces or the human stratum corneum interference artifacts appear due to high autocorrelation of the reflected light. With the large amount of directly reflected light the autocorrelation term of Equation 3.6 is not negligible anymore and produces vertical lines in the B-scan as shown in Figure 3.11(a). This can be reduced by tilting the sample relatively to the scanning head (for liquid samples the head has to be tilted). There is also a post-processing algorithm implemented in the measurement software which reduces the impact but fails for really strong reflections.

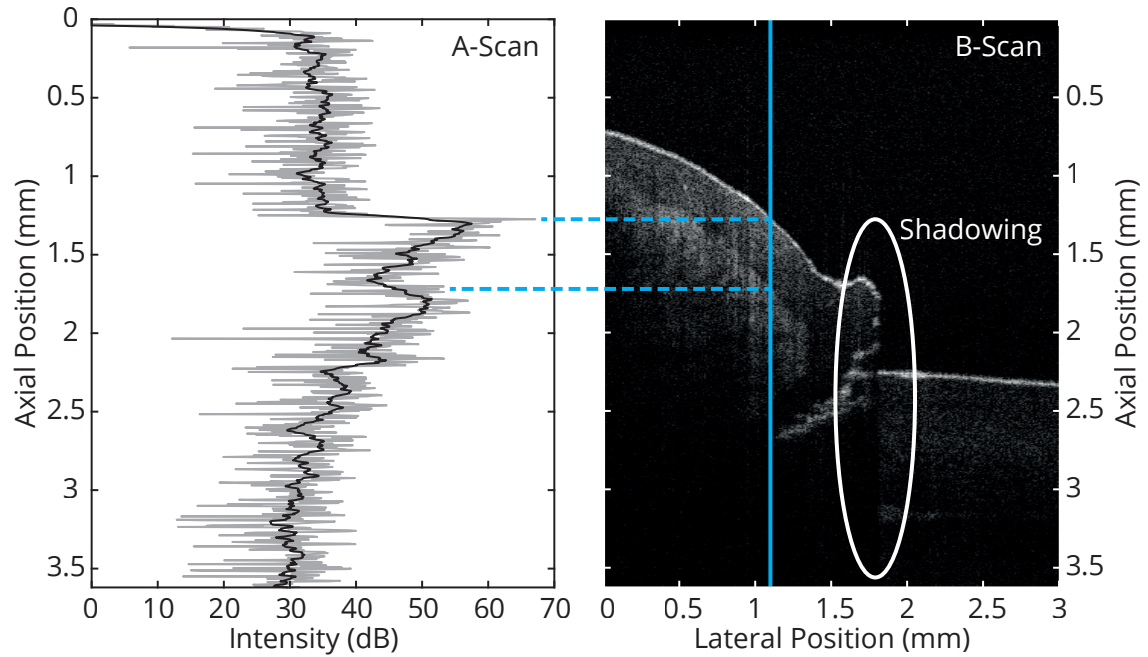


Figure 3.9: OCT A- and B-scan of a thumbnail. On the left-hand side a typical A-scan is presented as a part (marked by a cyan line) of a B-scan image (right-hand side). The light gray curve is the original data whereas the black curve is the smoothed data guiding the eye. The peaks are linked to the corresponding positions of the interfaces between different layers of the skin. In the B-scan shadowing occurs, a typical OCT problem.

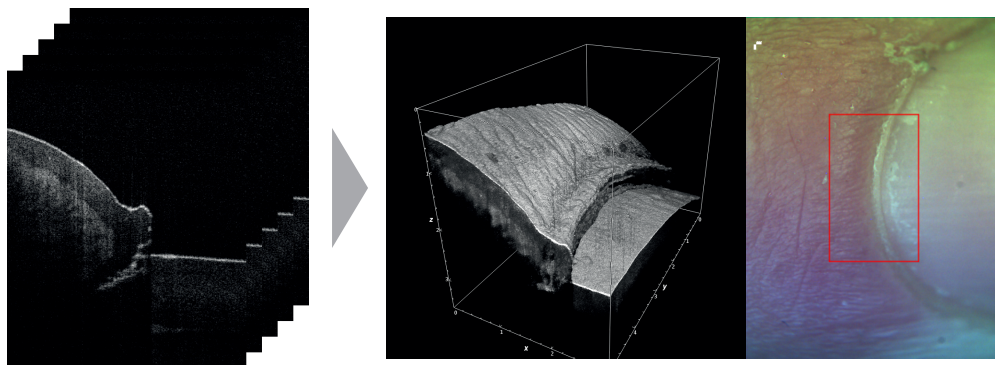
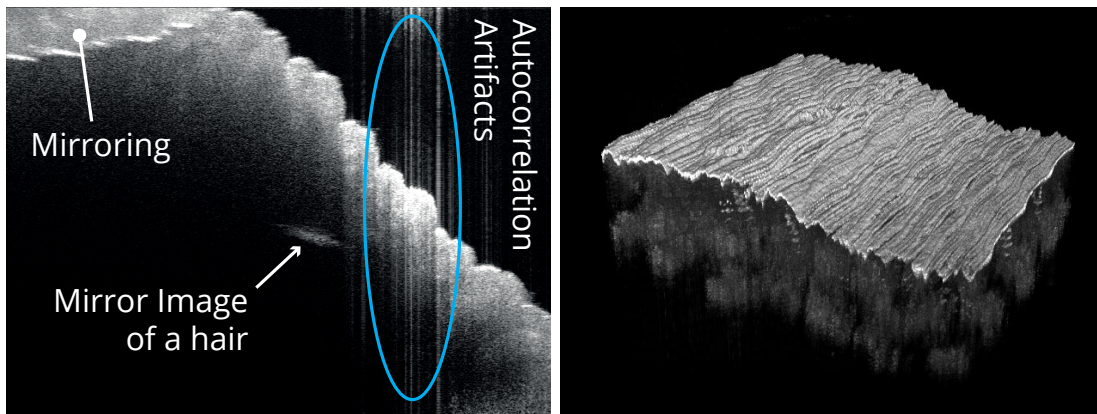


Figure 3.10: Concatenated cross-sectional B-scans (left) produce a C-scan which is a 3-D point cloud (center). On the right hand side the *en face* image of the measured region is shown marked by a red box.

The Fourier transformation produces a signal of 2048 data points out of 2048 detector pixels. Due to the symmetric characteristics of Fourier transformations the A-scan has only 1024 data points. Every image point has a complex conjugate at the negative distance. Hence, moving the sample beyond the zero delay point to a negative position results in a mirror image. In Figure 3.11(a) this flip effect is marked. Even objects not in the axial field of view may produce signal (e.g. a hair on a skin as in Figure 3.11(a)). In most cases mirroring can be avoided by keeping this in mind when positioning the sample.



(a) Mirror and autocorrelation artifacts

(b) Motion artifacts

Figure 3.11: Artifacts present in FD-OCT. Both images were obtained on human skin. (a) At the top of the image (zero delay) the structure is flipped or mirrored. A hair, not visible in the picture, is producing a signal due to mirroring. In the focal region (vertical center) the reflected light is causing autocorrelation artifacts producing vertical lines (blue ellipse). (b) A typical ripple distortion caused by motion of the sample.

Motion artifacts

While measuring, longer integration times lead to an increasing probability of signal displacements for slightly moving samples. E.g. an unintended muscle contraction or even the heartbeat is able to distort an OCT measurement significantly. A distorted 3-D OCT image is shown in Figure 3.11(b). Motion leads to a rippled structure of the measurement. With higher illumination power and shorter integration times while having a sensitive detector this can be handled well. Still, there is always a trade-off between a good SNR and motion artifacts for *in vivo* measurements. Recent fast OCT systems do not have these limitations on the time scale of heartbeat.

Shadowing

Shadowing is a more OCT specific issue. The more light is scattered or reflected the less light is available for deeper structures. Especially highly reflective interfaces where the difference of the refractive indices is very high (e.g. the interface of air and *stratum corneum* or keratin) produce a kind of shadow. In the right part of Figure 3.9 this effect is shown. There the highly reflective horny layer covers the nail producing a significant contrast. A first approach is to reduce the difference of the refractive indices and providing a kind of impedance matching. For example, cleaning skin with ethanol before measuring reduces the reflectivity as well as using index matching substances. If the illumination of the sample is sufficiently high, there is the opportunity to use so called digital optical clearing. A method that amplifies the signal of deep structures by post-processing algorithms able to remove the shadow and reconstruct a scan. However, due to the large computational cost this is currently not applicable for real-time processing during measurements, especially for volumetric imaging with a large amount of data.

Absorption

OCT is not sensitive to absorption and there is no related contrast in the measurements. However, it is still possible that the specimen has a strong absorption at the OCT wavelength. In general, less light results in a decreasing SNR which then drops for highly absorbing media significantly. Provided that enough light and scatterers are present in less absorbing surrounding media, for absorption centers contained in this environment OCT would produce a dark noisy patch, at least for conventional OCT systems. By using a specific wavelength region like the therapeutic window in the life sciences (see Chapter 2.2.1) this effect can be minimized.

Sometimes absorption is an important parameter to be investigated. So called spectroscopic OCT (SOCT) [42] is able to produce hyperspectral, cross-sectional OCT images where every point is associated with its absorption spectrum. Via a Morlet wavelet transform in addition to the Fourier transform not only the envelope of the interference signal is used, but also faster oscillation where the modified source spectrum is encoded (in contrast to the assumption made from Equation 3.5 to 3.6). Provided a suited setup this technique allows for measuring the spectral properties of tissue, e.g. absorption. In [43] SOCT is utilized to measure changes in the absorption spectrum of oxy- and deoxy hemoglobin. Although being a powerful approach, this technique is beyond the scope of this work.

Optical path vs. real path

Due to the interferometric design OCT is measuring phase differences (see Chapter 3.2). The measured axial distance is derived out of the correlation (interference

pattern) of the electromagnetic fields with their particular phases. The phase propagation is determined by the speed of light in the medium or the refractive index, respectively. For e.g. air with $n \approx 1$ the real (geometrical) axial distance d_r and the measured (optical) axial distance d_m correspond to each other, where for optical denser media ($n > 1$) the measured axial distance is given by $d_m = n \times d_r$. The same applies for meta-materials with $n < 1$.

This is problematic if the OCT system is also used for quantitative thickness assessment of specimen layers like in this work. Different layers with varying effective refractive indices may lead to misinterpretation of the layer thicknesses. In Figure 3.12 the schematic shows a 2×3 grid with different refractive indices. With the knowledge of the indices it is easy to reconstruct such an image but the information is not always available. Thus, the reconstruction may require preliminary measurements of

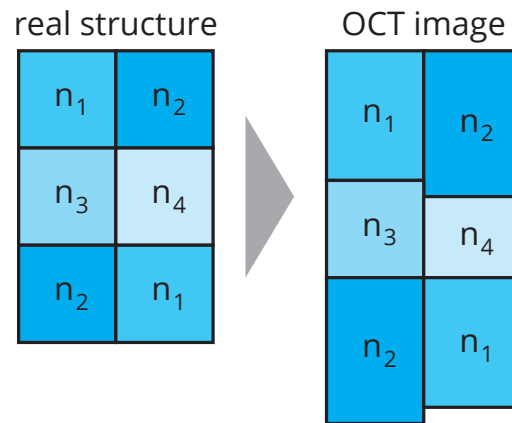


Figure 3.12: Principle of image distortion by different refractive indices. The acquired image does not show the original equidistant pattern. Real distances are modified by the indices n_1 to n_4 .

the refractive index.

The other way around, it is possible to get the refractive index by comparing the measured thickness and the real thickness, if available, as presented in Chapter 4.3. Of course, this requires a suitable sample and a proper a priori thickness measurement or specification.

3.3.2 Coherence gating, axial resolution and sensitivity roll-off

All three terms, coherence gating for TD-OCT, axial resolution and sensitivity roll-off for SD-OCT are related to the source spectrum and detector properties as boundary conditions for the autocorrelation (see Chapter 3.2).

By nature, the temporal coherence is determined by the spectral bandwidth of the source spectrum described in Equation 3.7. Interference only occurs for path

3 Optical coherence tomography on scattering media

differences of sample and reference arm within the coherence length given by

$$l_c = \frac{2\sqrt{\ln(2)}}{\Delta k} = \frac{2\ln(2)}{\pi} \frac{\lambda_0^2}{\Delta\lambda} \quad (3.17)$$

where Δk is the FWHM frequency bandwidth, λ_0 is the central wavelength and $\Delta\lambda$ is the FWHM wavelength bandwidth of the source. This is identical to Equation 3.1 in Chapter 3.1.1. In the following, k is denoted as frequency and used synonymously to the wavenumber described in Chapter 3.2 with $k = 2\pi/\lambda$. The induced filter mechanism is denoted as coherence gating, a main property of TD-OCT. The broader the spectrum of the source, the higher is the axial resolution which can be achieved. Provided a light source capable of a very broad spectrum of hundreds of nm with a sufficient intensity output new challenges arise (e.g. varying wavelength dependent absorption and scattering). Thus, a tradeoff is needed suiting the specimen's properties and the available hardware.

A very similar mechanism is determining the axial resolution of SD-OCT. The acquired signal is limited in two ways connected to each other. One is the confined detector where typically the dispersive element of the spectrometer is chosen to fit the spectrum to the detector size. Another one is the finite spacing and the pixel size or the spectrometer resolution, respectively [44]. As described in [39] the finite resolution can be modeled (in good approximation) as an additional convolution of Equation 3.16 with a Gaussian function (right part of Equation 3.18) which can be interpreted as spectral resolution function.

$$I_D(k) \otimes \exp\left[-\frac{4\ln(2)k^2}{(\delta_r k)^2}\right] \stackrel{\mathcal{F}}{\Leftrightarrow} i_D(\hat{z}) \cdot \exp\left[-\frac{\hat{z}^2 (\delta_r k)^2}{4\ln(2)}\right] \quad (3.18)$$

where $\delta_r k$ is FWHM of the spectral resolution of the measurement system. Again, \hat{z} is the substitution of $2\Delta z$. Note that the convolution (denoted by \otimes) is equivalent to a product of the Fourier transformed factors as indicated by $\stackrel{\mathcal{F}}{\Leftrightarrow}$. The spectral resolution function transforms to a Gaussian shaped attenuation function (left part of Equation 3.18). As a result, for increasing frequencies k the intensity i_D is reduced. Since higher frequencies correspond to longer photon paths this is equivalent to a sensitivity reduction for deeper regions. The depth where the signal's SNR is reduced by a factor of two (or 6 dB) can be easily calculated by

$$\exp\left[-\frac{\hat{z}^2 (\delta_r k)^2}{4\ln(2)}\right] = 1/2 \quad \Rightarrow \quad \hat{z}_{6\text{dB}} = \frac{2\ln(2)}{\delta_r k} = \frac{\ln(2)}{\pi} \frac{\lambda_0^2}{\delta_r \lambda} \quad (3.19)$$

The last representation of Equation 3.19 is similar to half of the coherence length (Equation 3.17) but for spectral resolution $\delta_r \lambda$ instead of spectral bandwidth $\Delta\lambda$.

3.3 Characteristics of optical coherence tomography measurements

This dependence leads to a signal attenuation for higher frequencies corresponding to deeper positions \hat{z} , called *sensitivity roll-off*. Hence, the signal degradation originating from this mechanism can be reduced by improving the resolution of the spectrometer.

“An investment in knowledge pays the best interest.”

— Benjamin Franklin



Chapter 4

Quantitative measurements of optical properties

In this chapter the knowledge on OCT signal generation will be applied to real measurements of different samples as a prerequisite for the investigation of human skin with OCT as a central modality. It is convenient to start with more comprehensible samples and successively increase the level of complexity, since skin is a very complex tissue. The focus here lies in the data gathered from different homogeneous specimen starting with simple liquid samples like milk solutions, to specially prepared polyvinyl alcohol (PVA) hydrogel phantoms and layered structures. In particular the optical properties like scattering coefficient μ_s , the refractive index n and the thickness are of interest where the latter two are naturally coupled by the light velocity in the medium.

4.1 Optical coherence tomography setup

While mostly used as pure imaging device, an OCT system also enables to measure depth dependence of light scattering directly [41]. The measured signal of an OCT device is always a convolution of the light signal and the detection or device function of the measurement system including the confocal point spread function. The light signal is produced by backscattered or reflected light. In homogeneous media this OCT signal decreases exponentially with depth following the Beer-Lambert law. The extinction coefficient μ_{ext} can be directly estimated from the slope of the exponential decay (see Section 3.2). For (nearly) non-absorbing media (absorption coefficient $\mu_a \approx 0$) the extinction coefficient μ_{ext} is only determined by the scattering coefficient ($\mu_{ext} = \mu_a + \mu_s \approx \mu_s$).

For the investigations in this work the commercial Spectral Domain OCT imaging system *Telesto-II* manufactured by Thorlabs GmbH, Germany was used. The general setup is outlined in Figure 4.1 and consists of an OCT base unit with the light

source and a spectrometer including data acquisition on the left hand side and a galvanometric scanning system including the interferometer on the right hand side. The central wavelength of this device is 1300 nm with a spectral bandwidth of 100 nm resulting in an axial resolution of 5.5 μm (air). The probe is equipped with an LSM03 F-Theta scanning objective providing a lateral resolution of 13 μm . It reduces the image distortion by translating the angular beam displacement, originating from the galvanometric mirror rotations, into equidistant lateral steps in the focal plane. The reference reflector can be moved axially adjusting the reference arm length to match the phase difference of the focal position in the sample. In this way the axial field of view or the imaging window z-axis, respectively, can be moved and the depth region of the imaging can be selected. The base unit and the scanning system are connected by a control cable and a single mode optical fiber which is used bidirectional to provide the source's light and to deliver the correlated light to the spectrometer. These paths are decomposed by a fiber based circulator. As light source two SLDs with slightly displaced output spectra (in relation to one another) are coupled to one fiber guiding the light to the circulator. The spectrometer is a linear CCD array with a size of 2048 pixels connected to the acquisition PC processing the data.

In the following, if no other parameters are given, each measurement was averaged over 50 B-scans where each A-scan was averaged over 20 single shots. This is a good trade-off between speed to avoid motion artifacts or blurring and a sufficient SNR. However, for very weakly scattering media the backscattered light might be very low such that the signal becomes small and the SNR drops substantially. In general, this is acceptable, since the comparability of the measurements has to be

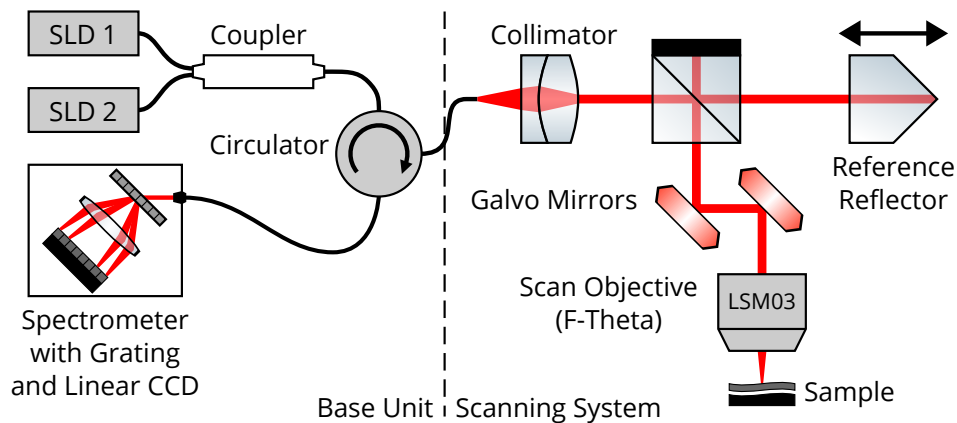


Figure 4.1: Scheme of the SD-OCT setup. Two broadband SLDs are used as light sources. The scanning probe is a Michelson interferometer with adjustable reference arm length. A galvanometric mirror set and an F-Theta objective allow scanning the surface in x and y direction (in the surface plane). The spectral signal is detected by a linear CCD-array.

maintained. Accordingly, the signal and the SNR increase with increasing scattering rates generating a good signal at the cost of penetration depth. Although OCT is very sensitive even for small amounts of light, at some point the loss becomes too high to image deeper structures (see also *shadowing* in Chapter 3.3.1). In addition, the sensitivity roll-off (Chapter 3.3.2) has to be considered.

4.2 Homogeneous tissue phantoms for optical coherence tomography

As mentioned in the introduction of this chapter, it is convenient to start with simple homogeneous phantoms. Measurements with well-known scattering particles with defined sizes in the region of the scattering structures of the human skin provide a preliminary understanding of the fundamental processes in such scattering media.

4.2.1 Homogeneous liquid phantoms

Although liquid, it has been shown that Intralipid[®] solutions are a good choice as homogeneous scattering medium [45–47] to mimic skin properties. Intralipid[®] is a fat emulsion of soy bean oil, egg phospholipids and glycerin available with different standard concentrations. The fat particles can be considered to be equally sized at about 1 μm with a certain margin that can be improved via sonication with ultrasound. Being in the Mie scattering regime (for 1300 nm, Chapter 2.2.2) the emulsion offers the opportunity to produce solutions of liquid samples with arbitrary well-defined particle concentrations, relevant for OCT measurements. However, there is also another, much more accessible fat emulsion available, that is sufficient for the purpose of this work and many other purposes in general: milk.

The liquid homogeneous scattering phantoms in this work were prepared by diluting homogenized, heat-treated milk (3,5% H-Milch) in ultra-pure water (Milli-Q reagent grade water, Millipore Corp.). Prior to the dilution, milk was sonicated for 30 min (PALSSONIC, Allpax) to ensure its homogeneity. This type of phantom is widely used to test the models of light propagation in turbid media [48] (see Chapter 5). Note that the knowledge of the explicit size distribution of the fat-droplets in the emulsion is not needed, since it contributes to the effective anisotropy factor, which is of interest later on. The particle size of milk is expected to be in the micrometer region (0.1 μm to 10 μm), and thus in the Mie scattering regime according to [48]. In Figure 4.2 a typical OCT measurement of such a sample is presented.

Undiluted milk is a very strong scatterer, such that the penetration depth of OCT is limited to roughly one millimeter, which is stronger scattering than in human skin.

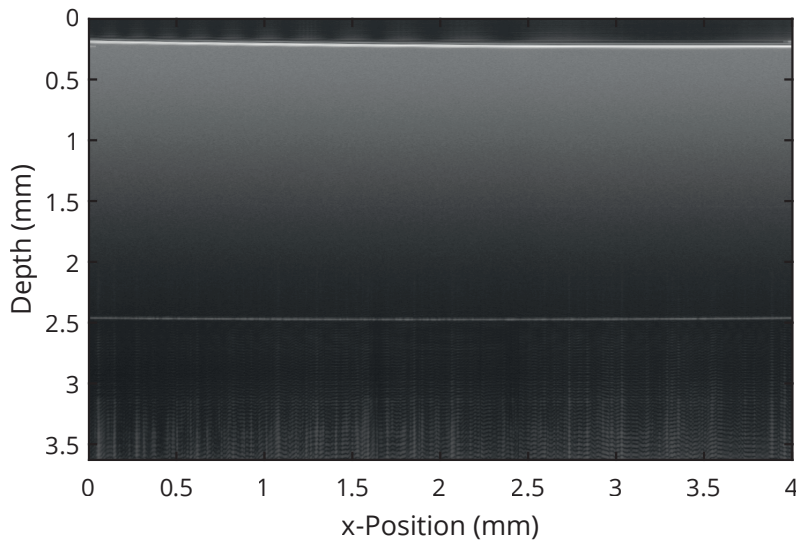


Figure 4.2: OCT measurement of a homogeneous liquid phantom with 50 wt. % milk in demineralized water. The particles, with a size of $\approx 1 \mu\text{m}$, are not resolvable with the used OCT system and produce homogeneous scattering and a decreasing uniform gradient.

4.2.2 Homogeneous hydrogel phantoms

For the purpose of multimodal measurements with OCT and optoacoustics the phantoms require also a similarity of acoustic properties. Polyvenyl alcohol (PVA) hydrogels (Sigma-Aldrich 363146, M_w 85–124 99+% hydrolyzed) were chosen to perform this task. The samples produced in this work are based on the same recipe as described by Blumenröther et. al in [49]. The liquid mixture of PVA, demineralized water and ethanol is poured on a glass plate with a spacer ring defining size and thickness of the phantom. Another glass plate is placed on top and fixed with the first glass plate. After 2 days in a freezer it is polymerized to a hydrogel as soft tissue phantom with the acoustic properties similar to those of skin.

In addition, scattering properties have to be considered since the hydrogel is transparent for OCT. Therefore, dry polystyrene microspheres Polybead© (by Polysciences) with a diameter of $1.00 \mu\text{m}$ were added to the PVA. The spheres are hydrophobic and need to be used with the solvent sodium dodecyl sulfate (SDS) to produce a homogeneous distribution. However, there are still drawbacks concerning the homogeneity: clustering occurs resulting in larger scattering centers leaving the Mie scattering regime showed in Figure 4.3. When adding melanin as an absorber for the optoacoustics contrast the melanin particles may also cluster and form even bigger scattering centers.

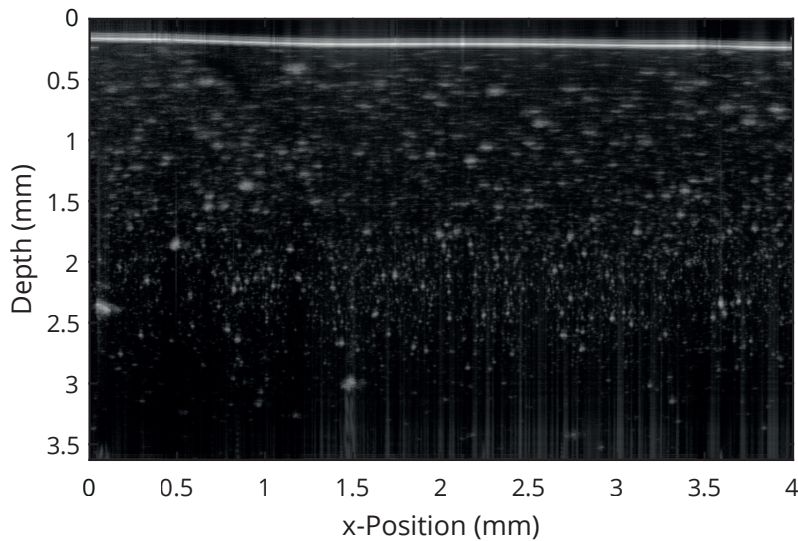


Figure 4.3: OCT measurement of a PVA hydrogel phantom with microsphere scatterers. Clusters are present as white grains of different sizes. The upper blurred clusters are out of the focus of the OCT beam.

4.2.3 Layered phantoms

Both, the liquid and the hydrogel phantoms are stackable. In case of the liquid samples a cuvette with two chambers was constructed consisting of three Zeiss/Schott cover glasses fixed on 3-D-printed spacers with double faced adhesive tape and a holder socket as shown in Figure 4.4. Dilutions with different liquid concentrations were filled into the cuvette chambers to mimic different layers. The OCT measurements were applied horizontally from the side. For low concentrations enough light passed through the first chamber to measure the second chamber as well. But for high concentrations, particularly in the first chamber, the loss of light due to scattering was too large to image the second chamber. The air-glass and solution-glass interfaces led to additional light loss. With the availability of the PVA phantoms this approach was not further pursued. Still, it can be constructed as simple one layer cuvette providing a determined thickness for refractive index measurements of liquid samples with appropriate concentrations.

With the PVA hydrogel it is possible to produce different pieces with different parameters (absorption realized by adding melanin and scattering by adding microspheres) and stack them for the OCT measurements. For OCT the difference in their scattering properties is visible. In Figure 4.5 an example of such a phantom is shown. Two different melanin concentrations are used leading to a different amount and size of clusters. Note that the upper scatterers are blurred and appear larger. This effect occurs due to the decreasing lateral resolution outside the axial focal plane which is

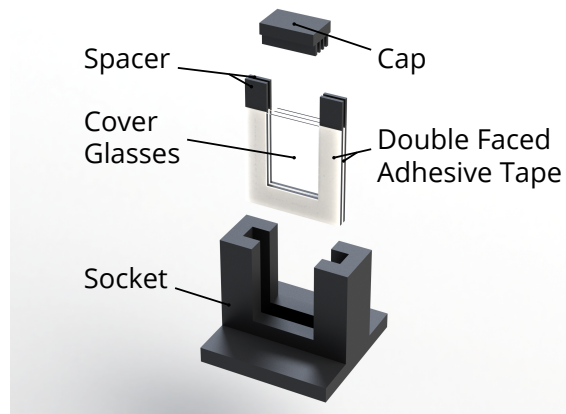


Figure 4.4: Rendered image of the double layer cuvette. The core element consists of two spacers combined with double faced adhesive tape on each side. Three cover glasses are pasted to create two chambers for the liquid. A socket is holding the assembly vertically, where a cap is closing up the cuvette.

located in the lower segment at ≈ 3 mm depth in Figure 4.5.

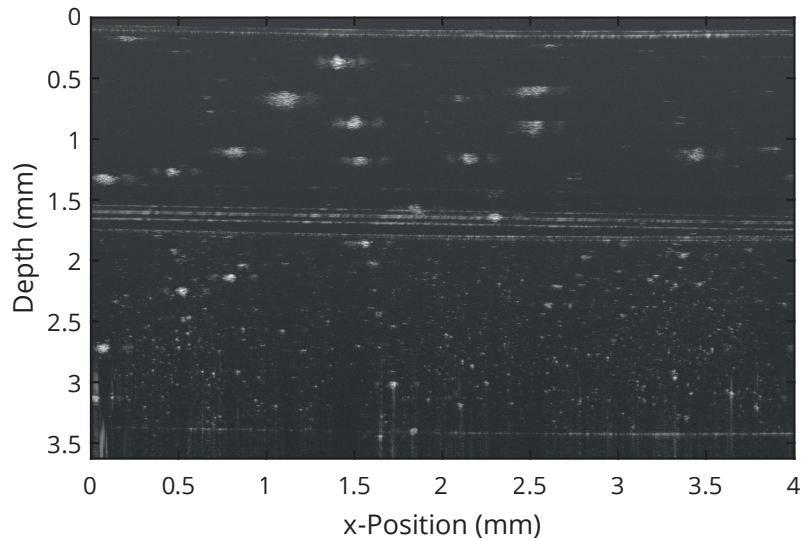


Figure 4.5: OCT measurement of a stacked PVA hydrogel phantom with two layers of different melanin concentrations. The focal plane is in the lower part. For a better index matching the space between the layers is filled with demineralized water.

4.3 Layer thickness and refractive index

The layer thickness determination, in general, requires the knowledge of the refractive index and vice versa. On the one hand this gives easy access to these quantities of samples where either the refractive index or the sizes are known, on the other hand it is challenging to extract quantitative information for samples where preliminary knowledge is not feasible. For example a refractive index determination of the semi-infinite liquid samples mentioned before is not possible because the layer thickness is not resolvable with OCT. But for the PVA samples with a suitable thickness the relevant dimension is known or easily measurable by design. A possible solution is to measure a medium with the same dimension and known refractive index. Therefore, it is appropriate to use the air gap of the glass plates forming the samples presented in Section 4.2.2 as reference. In Figure 4.6 the measurement principle is illustrated. To account for the sample geometry (e.g. varying thicknesses) multiple measurement points are recommended to extract the correct thicknesses. The optical distances of the glass plates with one of the two media in between, d_{air} and d_{PVA} , are measured with OCT. Assuming $n_{\text{air}} = 1$ the refractive index of the PVA phantom is given by:

$$n_{\text{PVA}} = \frac{d_{\text{air}}}{d_{\text{PVA}}} \quad (4.1)$$

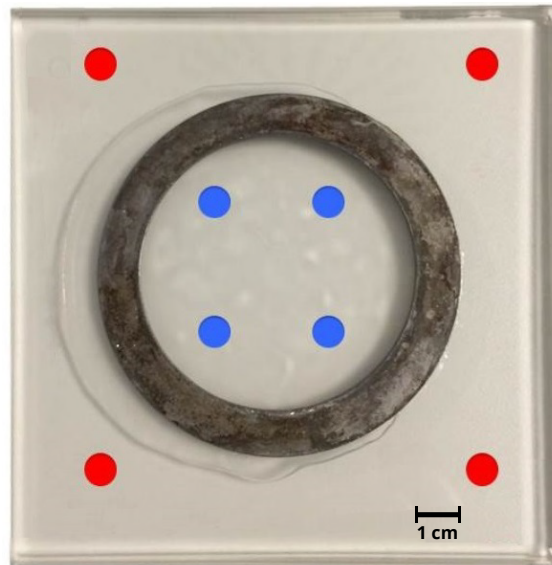


Figure 4.6: PVA phantom with spacer ring (6 cm inner diameter) and glass plates as described in Section 4.2.2. The measurement points to calculate the refractive index of the phantom are marked red for d_{air} (optical distance between glass plates in air) and blue for d_{PVA} (optical distance between glass plates in PVA).

This value is necessary to correct the OCT measurements of a particular PVA phantom regarding the measured axial dimension or thickness, respectively (see *Optical path vs. real path* in Chapter 3.3.1).

4.4 Scattering coefficient

According to Chapter 3.2 the scattering coefficient μ_s can be extracted directly from the depth profile (A-scan). In this section the general process is discussed neglecting effects like multiple scattering which has influence of the measured scattering coefficient. This is a central point of Chapter 5. The measured coefficient represents an effective scattering due to the design and the principle of OCT. Note that in this context a real scattering coefficient is not defined since the underlying scattering mechanisms are still investigated by the scientific community. Contrary to that, theoretical models may indeed provide a defined scattering coefficient. In this work these issues are only outlined to certain extent supporting the goal of measuring skin and extracting quantitative information beyond size and thickness of simple specimen. Skin, however, is far more complex and an applicability of the findings concerning scattering to medical applications is not straight forward. Nevertheless, it helps to understand fundamental processes of signal generation and signal shaping.

Homogeneous liquid phantoms

As an example, a set of the previously described liquid milk phantoms was prepared, measured and processed according to Chapter 3.2. In Figure 4.7 the acquired A-scans are plotted with their particular fitting functions (dashed cyan lines). Here the focal contribution was not removed since it is accounted for by the fit function. The data is normalized to the signal level after the first peak of the air-sample interface to make the curves more comparable. The focal contribution decreases with increasing scatterer concentration. Reflections on the air-sample interface (≤ 0.4011 mm) as well as data points corresponding to the deep parts where artifacts dominate the signal (≥ 2.4331 mm) are excluded for fitting. Only values > 0.4011 mm and < 2.4331 mm, given by the indices 151 to 909, are used for fitting, where the OCT z-Axis is ranging from 1 to 1024 pixels (as indices) with a spacing of $3.5 \mu\text{m}$ per pixel in air. The axis values are corrected by the refractive index of water n_{water} which is valid even for high milk concentrations. In total, the following formula maps and corrects the A-scan depth $x(i)$ to the pixel indices i :

$$x(i) = 3.6/1024 \times i/n_{\text{water}} \quad \text{for } i = 1 \text{ to } 1024 \quad (4.2)$$

This axis definition is denoted as *geometrical path length/2* in relation to the optical path length of the photons traveling twice the distance in the medium after being

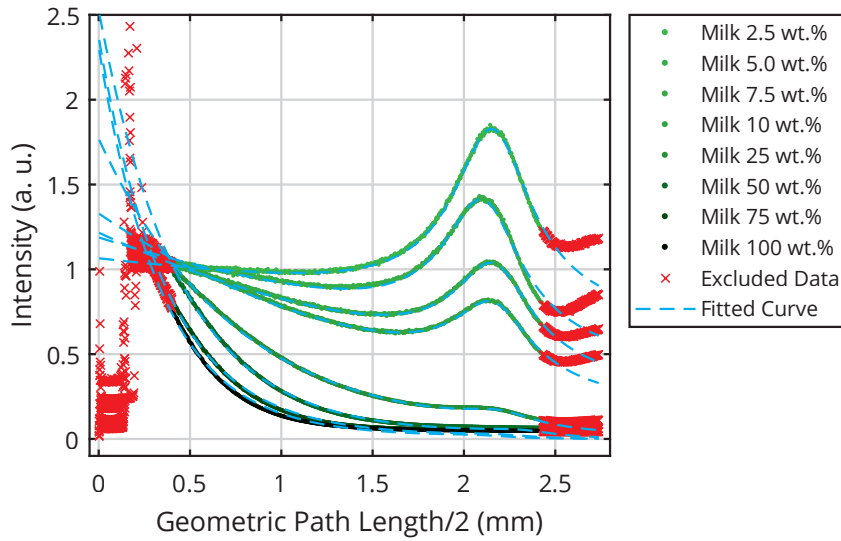


Figure 4.7: Measured OCT depth profiles (A-scans, green) of milk phantoms with different milk concentrations. The dashed cyan lines are the fitting functions.

reflected by an interface or a scatterer. All OCT depth measurements of this work share this axis definition which is also important to get the correct fit results.

The extracted values for the effective OCT scattering coefficient μ_s^{OCT} are shown in Table 4.1. The ability to measure the scattering coefficients provides additional

Table 4.1: Overview of extracted effective scattering coefficients μ_s^{OCT} acquired from the prepared phantoms (ratio of milk/water is given by weight percent). R-squared is the coefficient of determination indicating the fit quality.

milk/water (wt. %)	μ_s^{OCT} (cm^{-1})	R-squared
1	0.5017	0.9995
2.5	1.185	0.9994
5	2.834	0.9943
7.5	4.247	0.9968
10	5.722	0.9976
25	13.46	0.9994
50	22.49	0.9985
75	28.13	0.9938
100	31.13	0.9930

4 Quantitative measurements of optical properties

information and elevates OCT to a more quantitative tool, at least for homogeneous samples.



These measurements are also used for the comparison with the numeric simulations in Chapter 5.

“Computers are useless. They can only give you answers.”

— Pablo Picasso

5

Chapter 5

Numerical OCT simulations

During the last decade, strong efforts have been made to elucidate the mechanisms underlying OCT imaging for single-layer as well as multi-layer samples and scattering low-absorbing media. Also, there is an increased interest in both analytical and numerical models to extract optical properties of the sample under study from the recorded image. All these aspects have not been satisfactorily solved yet and advances in this field are promising as they might enable the application of OCT as a precise quantitative measurement tool. One approach towards determination of optical properties is to utilize the intensity decay of an OCT signal in low- or non-absorbing media to derive the scattering coefficient of the studied/probed tissue. Since a real OCT measurement of highly scattering media cannot be described by ballistic photons alone, a central question arising is how to quantify the contribution of single and multiple scattered photons to the OCT signal.

On the modeling side, significant advances were reported by various groups in the last years. Simulation activities focused more and more on taking into account additional parameters relevant for real applications such as realistic geometric and interferometric conditions and requirements for detection in an OCT setup [50]. Most numerical approaches so far are based on the Monte Carlo (MC) method which, in biomedical optics, represents the gold standard approach for simulating light propagation in biological tissue, both due to its accuracy and its flexibility in modelling realistic, heterogeneous tissue. For example, Smithies et al. [45] developed an MC OCT model taking a geometrical implementation of the OCT probe with low-coherence interferometric detection into account. They found that OCT, in general, detects only minimally scattered photons. Alerstam et al. [51] describe a highly optimized MC code package for simulating light transport developed on NVIDIA graphics processing units (GPUs). It is built for general-purpose computing Fermi GPU micro-architecture.

In addition to numerical MC methods alternative analytical and semi-analytical models were developed to describe the OCT signal in scattering media theoretically, taking various physical effects into account. For instance, μ_s is reduced as a result of

interference effects, and the phase function of the scattered light and, thus, the OCT signal is modified. The effects of this so-called dependent scattering on the OCT signal are well described by the analytical extended Huygens-Fresnel (EHF) model as presented in [52].

As both multiple scattering and dependent scattering can have a strong effect on the OCT signal, it is useful to quantify the two effects in simulations, e.g. by using OCT in reflection and transmission mode [53]. For a dynamic case, signal attenuation rates for a Doppler OCT were studied and an increasingly distorted flow profile and a strong non-linear decrease of the scattering coefficient μ_s were found as the concentration of scatterers increased [54]. The influence of the anisotropy factor g on the scattering coefficient measured by OCT and the deviation for large anisotropy factors and multiple scattering from the linear case are discussed in [55]. An analytic approach considering multiple and dependent scattering as well as extrinsic experimental parameters such as OCT beam shape is presented by Almasian et al. in [56], which shows a good agreement between measurement and theory. The numerical results in [56] show that the non-linear behavior of the scattering coefficient is not only caused by dependent scattering but also as a result of a broadening of the OCT beam due to light scattering inside the tissue.

Concerning numerical simulations, MC methods were used to simulate OCT signals from several blood layers and different concentrations of constituents such as haematocrit and intralipid as well as from upper skin layers with various thicknesses [57]. These examples indicate that an adequate description of multiple scattering is crucial to a conclusive and realistic simulation of OCT signals. Numerical approaches such as Monte-Carlo (MC) simulations are inherently different from analytical approaches such as the extended Huygens-Fresnel (EHF) simulations. As shown in [45] and [52] both approaches are well suited to simulate OCT signals. While MC provides the spatial distribution of photon packages travelling in the scattering media, the EHF describes the radiative transport and the mutual coherence [58]. The EHF approach is the most comprehensive approach and assumes a partial interference of fields caused by multiple scattering. As stated in [56] and [58] the applicability of EHF on real tissue is limited but helps to understand and interpret the numerical results. A hybrid approach is presented in [58].

Within the scope of this work a simple and efficient MC model was implemented which is able to predict the scattering coefficients and the influence of multiple photon scattering with increasing concentration of scattering centers from measured OCT data. While the model reliably estimates optical sample parameters for a broad range of concentrations, it does not require inclusion of more complex phenomena such as dependent scattering. Instead, it relies on a particular weighting function which is introduced to describe various orders of multiple scattering events. In weakly scattering homogeneous media the measured scattering coefficient μ_s depends linearly on the concentration of scattering centers. In the case of strong scattering,

the dependence becomes non-linear. The model is able to accurately predict this non-linearity and can be applied to extend the OCT studies of biological tissue towards determination of optical properties in the future.

5.1 Simulation of an OCT A-scan

From a general point of view, the extended MC simulation launches photon packages, which travel through a virtual sample and undergo scattering processes. In case of absorption the so-called weight of the package is reduced mimicking a decreasing photon intensity or energy deposition, respectively. For the trajectories of the photon packages launched into the tissue the Henyey-Greenstein phase function

$$p(\theta) = \frac{1}{4\pi} \frac{1 - g^2}{[1 + g^2 - 2g \cos(\theta)]^{3/2}} \quad (5.1)$$

provides the angular dependent scattering probability $p(\theta)$ with respect to the anisotropy factor g and varying scattering angles θ . Only the coherent backscattered photons reaching the detector are contributing to the simulated OCT signal. Also, geometric selection rules like numerical aperture of the detection system are considered (see Figure 5.1). When modeling photon propagation in tissue, the MC method is used to determine photon distribution inside the medium. In this work, the GPU based MC Code from [51] is extended to generate further output data by storing not the absorbed photon energy but the backscattered photon packages with an exit angle matching the numerical aperture (NA) of the scan objective. As input source, an infinitesimally small laser beam is assumed, entering the medium perpendicular to

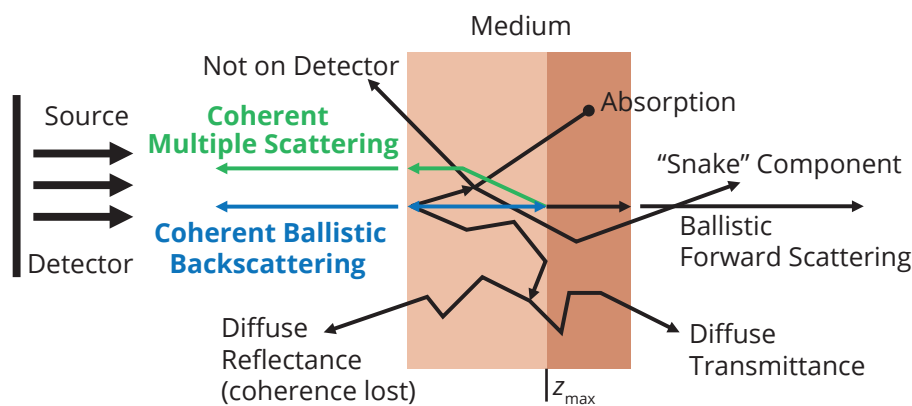


Figure 5.1: Light propagation scheme of simulated photons in a scattering medium. The contributing trajectories are highlighted in blue and green. The black paths are also calculated but do not contribute to the OCT signal simulation.

the surface with x, y, z coordinates equal to zero. A virtual non-absorbing specimen with a plane air-sample boundary and scattering properties which correspond to a specific concentration of milk is used as sample.

In this numerical model, the exact position in Cartesian coordinates x, y, z and its direction cosines $u_x(\theta), u_y(\theta), u_z(\theta)$ for each backscattered photon package are stored along with the number of occurred scattering events N_{se} and the maximal geometrical depth z_{max} reached in the tissue. Initially, θ is the angle between the substrate normal and the scattering direction of each incident package. Subsequently, θ always refers to the current deflection angle. In addition, the path length s for each photon package is recorded. To increase the performance of the Compute Unified Device Architecture (CUDA) code and to limit the size of the output-data, a maximal N_{se} can be set in the input file to limit the scattering events to be considered. This parameter omits further calculation of photon package trajectories beyond a preset value. For this work, photon packages with a scattering order larger than 10 are assumed as completely decorrelated with respect to the reference beam of the OCT such that these photons do not contribute to the OCT signal. The refractive indices of the surrounding medium n_1 and of the sample n_2 , the sample scattering coefficient μ_s and its absorption coefficient μ_a as well as the anisotropy factor g and the sample thickness D are used as input parameters for the simulation.

In experimental OCT signals, the measured depth at a given position in an A-Scan corresponds to the total optical path L_p or, equivalently, to the time a backscattered photon package travels inside the medium before impinging on the detector. More precise: Each photon package reaches a certain maximal depth z_{max} and has the total path length L_p , as well as a corresponding expected depth $d_{\text{max}} = L_p/2n_2 = s/2$ and a number of scattering events N_{se} . s is the total geometrical path provided by the MC simulation. Again, all these values are recorded for post-processing.

5.1.1 Modeling of the coherence condition

The key feature of OCT measurements is the coherence gating (see Chapter 3.3.2). This particular photon selection has to be modeled to mimic OCT signal generation. To contribute to the signal i_D , the difference between the recorded L_p and the minimal optical path $2 \times n_2 \times z_{\text{max}}$ corresponding to the depth reached by each photon package inside the tissue must be within the coherence length L_c of the OCT system. The following expression formulates the coherence condition for symmetrical case:

$$|L_p - 2n_2z_{\text{max}}| = |2n_2d_{\text{max}} - 2n_2z_{\text{max}}| < L_c/2 \quad (5.2)$$

Otherwise the photon package can be considered as decorrelated. Note that, in general, $z_{\text{max}} \leq d_{\text{max}}$.

Each coherence gate is valid for a certain depth. Accounting for that, the depth is divided into intervals of the size L_c with a number matching the simulated maximal depth. All MC photon packages corresponding to a certain depth and fulfilling the particular coherence condition are counted according to their specific interval bin. The histogram of the interval bins is similar to an OCT A-scan.

In case of weak scattering media with mainly ballistic photons this might be already considered as a simulated A-scan. However, for the calculations, multiple scattered photons are also taken into account which contribute to the OCT signal, especially for highly scattering media. These photons fulfill Equation 5.2 and might not be backscattered from the expected depth d_{\max} but from a different depth. The selection of these photons is modeled in the following Section 5.1.2.

5.1.2 Modeling of multiple scattering

One important aspect for OCT systems is that scattering events generally lead to a decrease in the degree of coherence of the OCT photons and consequently degrade the OCT signal. Therefore, to quantify this degradation, an adequate description of multiple scattering is crucial to a conclusive and realistic simulation of OCT signal generation. Yao and Wang [59] used the MC technique with angle biasing to simulate the OCT signal from homogeneous turbid media. The photons contributing to the OCT signal were categorized into different classes which are very distinct in their spatial and angular distributions as well as the numbers of scattering events experienced. The influence of the different photon categories to the OCT signal was studied systematically for samples with different optical properties.

Similar to [59], Wang et al. [60] studied the combined effect of the least scattered photons (LSP) and multiple scattered photons (MSP) on the OCT signal and quantified the degradation of the signal by multiple scattering events. For highly scattering media, the assumptions that mainly single scattering events contribute to the OCT signal and that the scattering coefficient μ_s is concentration independent can be invalid. Multiple scattered photons may still be detected and can significantly affect the OCT signal when their path length is within the OCT coherence length.

In accordance with [59] and [60] detected photons backscattered from the observed layer with coordinate z and those backscattered otherwise but fulfilling Equation 5.2 are distinguished, see schematic in Figure 5.2. The photons of the first group are expected to scatter with very small angles and to perform only few scattering events or to be even ballistic with a single backscattering event. Here, the recorded maximal depth reached is similar to the expected depth:

$$z_{\max} \approx \frac{L_p}{2n_2} = d_{\max}. \quad (5.3)$$

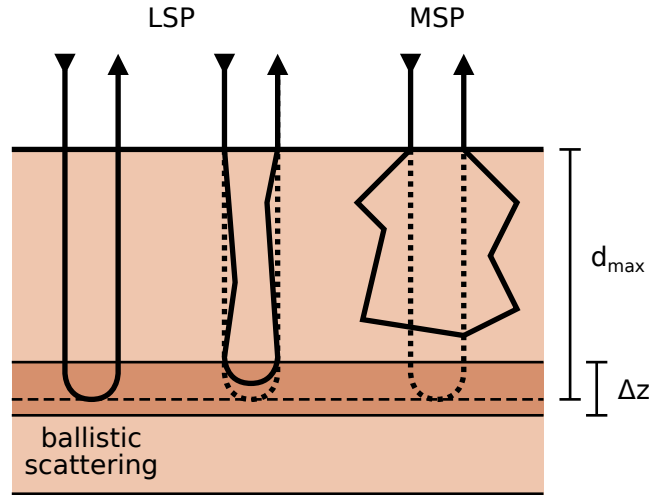


Figure 5.2: Schematic of different photon scattering orders. The left and the middle photon trajectories represent the least scattered photons (LSP), which include the ballistic case. The trajectory on the right shows an example for multiple scattered photons (MSP). Δz is the depth interval of the current bin. [61]

These photon packages provide information about the targeted depth inside the tissue. This work adopts the designation of these photons as LSP, while those photons that satisfy Equation 5.2 but are backscattered from a depth other than the targeted layer are labeled as MSP:

$$z_{\max} < \frac{L_p}{2n_2} = d_{\max}. \quad (5.4)$$

The MSP undergo wide-angle scattering and lead to a degradation of the detected OCT signal. The scattering coefficient μ_s is determined from a single exponential fit to the simulated data. Taking the numerical aperture

$$\text{NA} = n_1 \times \sin(\varphi) \quad (5.5)$$

of the whole optical system into account, only photons that exit the medium with an emergence angle α smaller than the acceptance angle φ of the detector are recorded (angles relative to the substrate and detector normal, respectively).

The signal intensity is determined by the amount of backscattered light, i.e., the number of collected photons. Thus, it depends on the concentration of the scatterers in the sample and is calculated from the summed weight of LSP and MSP photons normalized to the maximum of the smoothed region of interest (ROI) for better comparison to the normalized measured OCT signal.

While all coherent photons contribute to the OCT signal, the coherence might actually get lost due to scattering. Multiple scattered photons undergo a dephasing and may lose coherence, thus, contributing less to the OCT signal. To mimic this statistical process a heuristic weighting function based on the number of undergone scattering events is defined, similar to the Fermi-Dirac distribution [62, 63]:

$$F_w(N_{se}) = \frac{1}{1 + \exp[a \times (N_{se} - b)]} \quad (5.6)$$

Each recorded photon is weighted by a factor F_w which depends on its respective number of scattering events N_{se} . This weighting function affects the decay of the signal, where a describes the slope of the weighting curve corresponding to the sharpness of the cutting edge and b the inflection point corresponding to the number of considered scattering events. In Figure 5.3 several resulting functions with different parameters a and b are plotted.

The total simulated normalized reflectivity profile R_{sim} is determined by:

$$R_{sim}(z_s) = \sum_{N_{se}=1}^{N_{max}=10} F_w(N_{se}) \times [LSP(z_s, N_{se}) + MSP(z_s, N_{se})] \quad (5.7)$$

$LSP(z_s, N_{se})$ denotes all photons belonging to the LSP group which were scattered N_{se} times with a path length corresponding to the depth z_s and $MSP(z_s, N_{se})$ the

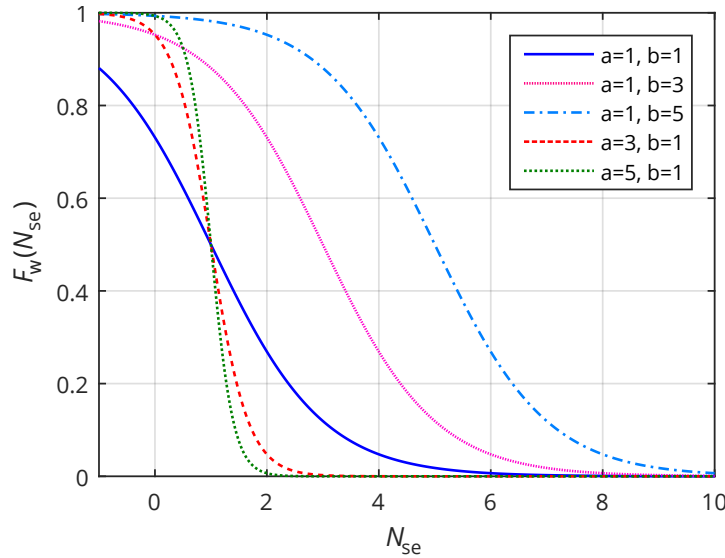


Figure 5.3: Weighting function F_w for different combinations of parameters a and b as function of the number of scattering events N_{se} (see also Equation 5.6). [61]

multiple scattered photons, respectively.

A reasonable selection of the constants a and b is central to the interpretation of the OCT signal and the extraction of the optical properties of the sample. In the next section the correct parameters are investigated to fit simulations and measurements.

5.2 Simulations and Measurements

In order to verify the applicability of the model to real OCT measurements, a number of experiments on well characterized semi-infinite liquid phantoms (presented in Chapter 4.2.1) were conducted. After preparation, the optical properties of the phantoms, namely refractive index n , scattering coefficient μ_s and anisotropy factor g , were determined experimentally and then used as MC model parameters for the simulations. The contribution of absorption to the total attenuation within the milk samples can be considered negligible. The effective refractive index of the mixtures was measured by OCT in a glass cuvette of well-defined thickness and found to be 1.32 at a wavelength of 1300 nm, similar to the value of water. The anisotropy factor g and the scattering coefficient μ_s^{GON} were measured with a goniometer (GON360, Instrument Systems, see Appendix A.2). There the dependence of μ_s^{GON} on the milk concentration is linear for low concentrations from 2.5 % up to 10 %. For higher concentrations ($> 10\%$) the goniometer detector signal was too low to measure. In the OCT measurements a non-linear behavior of μ_s^{OCT} at high concentrations above 25 % is observable, similar to measurement results reported by Kalkman et al. [54].

The model is based on the linear scattering coefficient μ_s^{LIN} as an input variable. The effective behavior of the scattering coefficient due to multiple and dependent scattering is covered later on by the weighting function as described in Section 5.1.2. Accordingly, values for the simulations were linearly extrapolated from measurements in the low scattering regime (see Table 5.1).

For the simulation a virtual sample is modeled on the real liquid milk sample. A one-layer non-absorbing phantom of 8 mm depth, with anisotropy factor $g = 0.96$, refractive index $n_2 = 1.32$ and $\mu_a = 0$ is designed to match the experimentally used milk phantoms. The scattering coefficient μ_s^{LIN} varies between 2.7 cm^{-1} and 54 cm^{-1} in agreement with the measured (low concentration) or linearly extrapolated scattering coefficients of the samples used in the experiments. For the presented OCT device an estimated effective $\text{NA} = 0.04$ and a coherence length $L_c = 7.5 \mu\text{m}$ according to the manufacturer data sheet (see Appendix A.1) are assumed. Note that the effective NA, in this case, is specified by the scanning beam itself. The light source channel and the spectrometer channel share the same geometric path and the same fiber coupling. Thus, only the backscattered light matching the mode field diameter is detected.

As described previously, it is distinguished between LSP and MSP taking into

Table 5.1: Overview of prepared phantom (ratio of milk/water is given by weight percent). Values for μ_s^{LIN} were used as input for the simulations and are either measured by goniometer (m) or extrapolated (e). The value for 7.5 wt. % is interpolated (i).

milk/water (wt. %)	μ_s^{LIN} (cm ⁻¹)
2.5	1.35 (m)
5.0	2.70 (m)
7.5	4.05 (i)
10	5.40 (m)
25	13.5 (e)
50	26 (e)
75	40 (e)
100	54 (e)

account photons that underwent up to 10 scattering events. This limitation to 10 scattering events is reasonable because it ensures short simulation times and is justified by the fact that photons scattered more often are not expected to contribute to the OCT signal because of a significant decrease in the degree of coherence. Each photon is weighted according to the number of scattering events using Equation 5.6. Since both categories, LSP and MSP, contribute to the OCT signal, their weighted sum is used for further analysis, see Equation 5.7. A comparison of the simulated signal with the measured OCT signal shows that for the case of stronger scattering and higher concentration, respectively, the contribution of the multiple scattered photons to the signal increases, as shown in Figure 5.4. The simulated signal is fitted with a single exponential decay function (Equation 5.8) in the ROI:

$$R_{\text{sim}}(z_s) = C \times \exp\left(-\mu_s^{\text{SIM}} \frac{z_s}{n_2}\right) \quad (5.8)$$

where C is an arbitrary scaling factor and z_s is the geometric path. The refractive index n_2 accounts for the optical path in the medium. μ_s^{SIM} is the desired simulated coefficient modified for multiple scattering. It is compared to that found by curve fitting of the measured OCT signal μ_s^{OCT} according to Chapter 3.2.

The decay of the summed intensity is smaller than the decay of the single scattered (ballistic) photon intensity, as can be seen in Figure 5.4. The strength of the decay is also influenced by the choice of the weighting parameters a and b in Equation 5.6. To obtain the best fit of simulated to measured data the contribution of the parameters a and b were investigated systematically. For this purpose, the sum of the LSP and MSP was calculated and the influence of the multiple scatter weighting function

5 Numerical OCT simulations

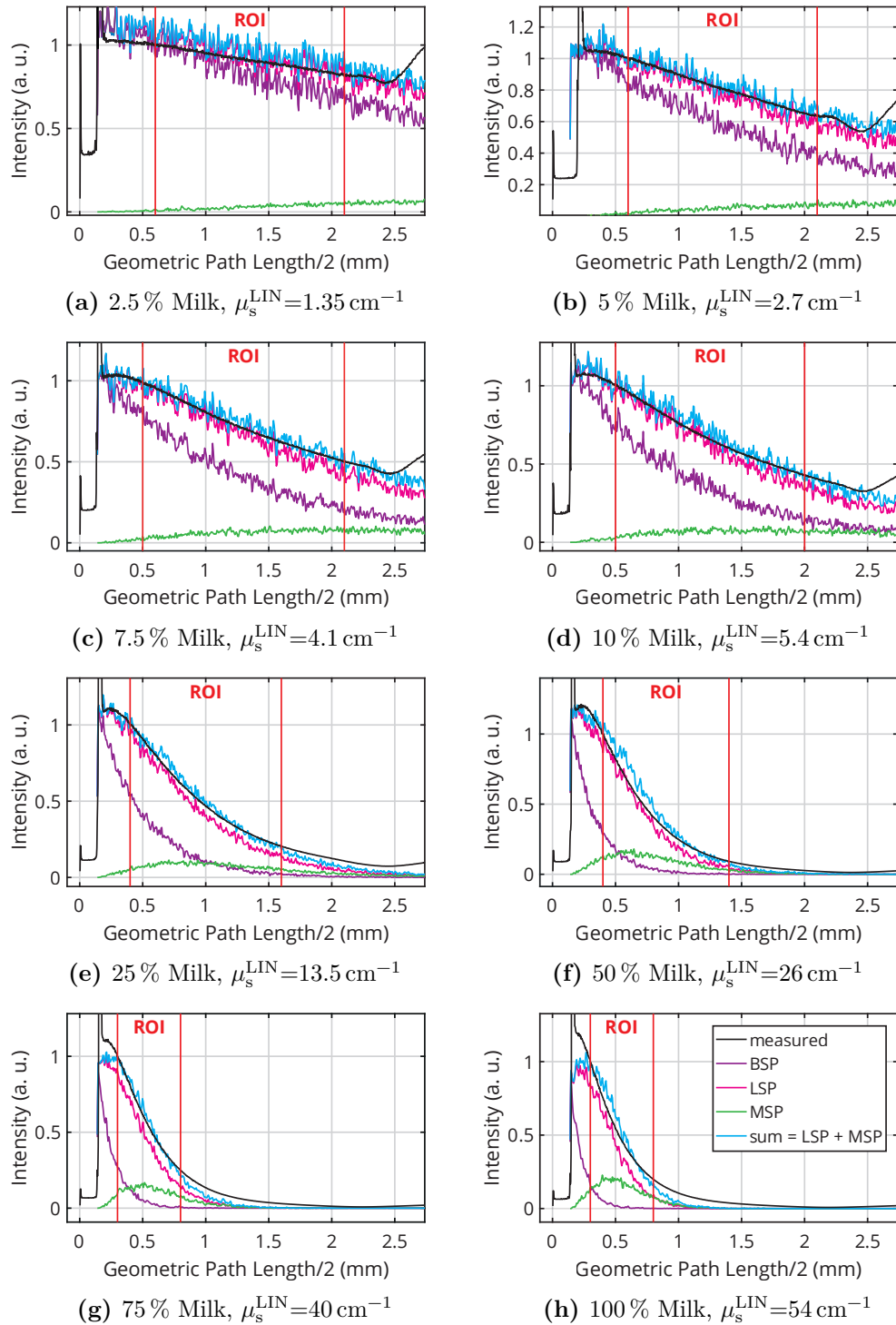


Figure 5.4: Contribution of MSP (green) and LSP (magenta) to the simulated OCT signal (cyan) for μ_s^{LIN} ranging from 2.7 cm⁻¹ to 54 cm⁻¹. Comparison to ballistic signal (BSP, purple) and deconvolved OCT signal (black) in the ROI (red vertical lines). The legend for all panels is depicted in the lower right panel. [61]

(Equation 5.6) was quantified by varying a in the range from 1 to 10 in steps of 0.5 and b again from 1 to 10 in steps of 0.1. Then, after fitting the simulated and the measured A-scans as described in Chapter 3.2, the difference of the coefficients corresponding to μ_s^{OCT} and μ_s^{SIM} was computed and also the goodness of fit represented by R-square was considered as quality indicator (see also Table 4.1). The simulations shown in Figure 5.5 are examples for two particular sets of a and b with different goodness of fit. Optimal values for the parameters a and b should be characterized by a minimum in the difference between values for μ_s^{SIM} calculated from the simulation and the μ_s^{OCT} deduced from measurement. These minima are presented in Figure 5.6. With regard to the progression of this minimum (dark blue region in Figures 5.6(a) and 5.6(b)), a saturation effect is present: The value for parameter b does not depend on that of parameter a for large enough values of a .

If the parameter a is kept constant, e.g. at $a = 5$, a linear dependence of parameter b on the linear scattering coefficient μ_s^{LIN} is found for all concentrations as shown in Figure 5.7. This allows a prediction of parameter b for all values of μ_s^{LIN} between 2.7 and 54 cm^{-1} and therefore the possibility to simulate the OCT signal of not yet measured concentrations of samples, in this work of milk phantoms. This is analogous to a training of the weighting function with a few measurements. Note that this has to be done only once for a particular sample type.

Setting $a = 5$ is a reasonable choice since the calculation of the above minimum difference between measured and simulated values of μ_s is not yet stable for $a < 5$ and the value for parameter b still varies (ripples in Figure 5.6(a)). For $a \geq 5$ parameter b , which is responsible for the relevant number of scattering events to be considered (see Equation 5.6), is saturating. In effect, the parameter a describes the weighting range for a particular number of events (slope of the curve, see Figure 5.3).

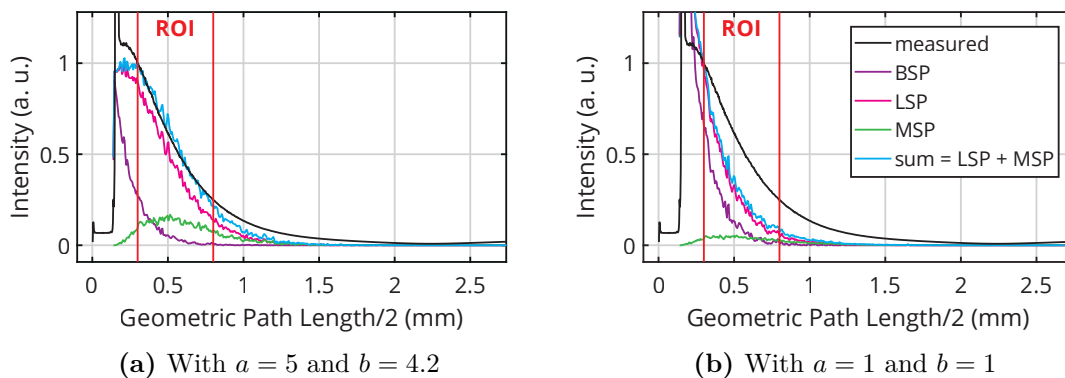


Figure 5.5: Intensity profile of ballistic photons, LSP (always including ballistic photons), MSP, and sum of LSP and MSP (all backscattered photons) for $\mu_s^{\text{LIN}} = 40 \text{ cm}^{-1}$. (a) best fit with $a = 5$, $b = 4.2$, (b) fit with $a = 1$, $b = 1$. Red vertical lines indicate the ROI. [61]

5 Numerical OCT simulations

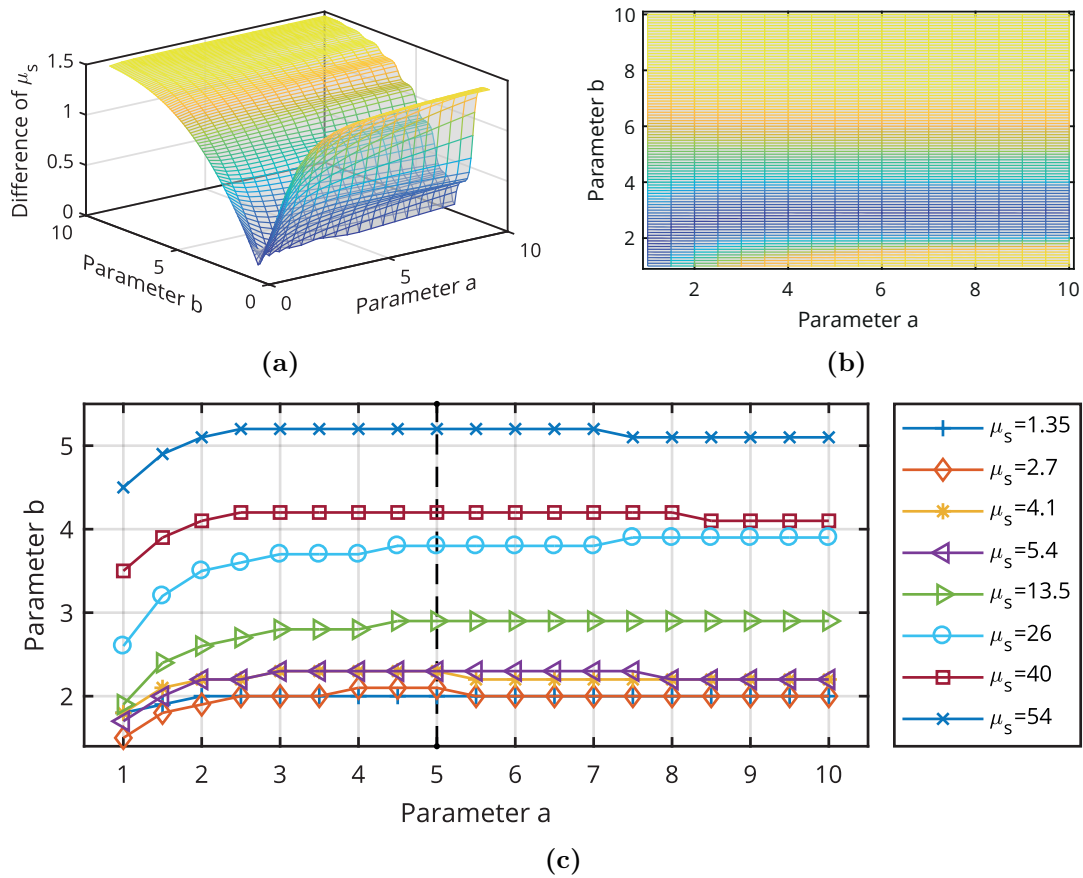


Figure 5.6: Best fit parameters: (a) 3-D surface and (b) 2-D intensity plot of the difference of fitted and measured μ_s as function of parameters a and b (for 25% milk, $\mu_s^{\text{LIN}} = 13.5 \text{ cm}^{-1}$) and (c) minimal difference for various μ_s^{LIN} ranging from 2.7 (bottom line) to 54 cm^{-1} (top line). The dashed vertical line indicates the parameter $a = 5$, which is chosen as working point for the model. [61]

Therefore, the smallest value for a common to all concentrations is chosen as best value. For $a > 5$ the weighting function (Equation 5.6) becomes more and more box-shaped, which means that all scattering events up to the value b are counted with weight one, b scattering events are counted with weight 0.5 and all others are not counted. With these parameters determined, the fits of simulation and measurement data are compared. The ROI, which essentially is the pure exponential part (see Equation.3.15), decreases with increasing μ_s . This makes the fitting procedure difficult for high scattering coefficients. For example, while for $\mu_s^{\text{LIN}} = 5.4 \text{ cm}^{-1}$ the ROI is relatively wide and the simulated and measured data are in good agreement (see Figure 5.8(a)). The ROI for $\mu_s^{\text{LIN}} = 54 \text{ cm}^{-1}$ is much smaller and the overlap of measured and simulated data decreases (see Figure 5.8(b)). Still, both cases

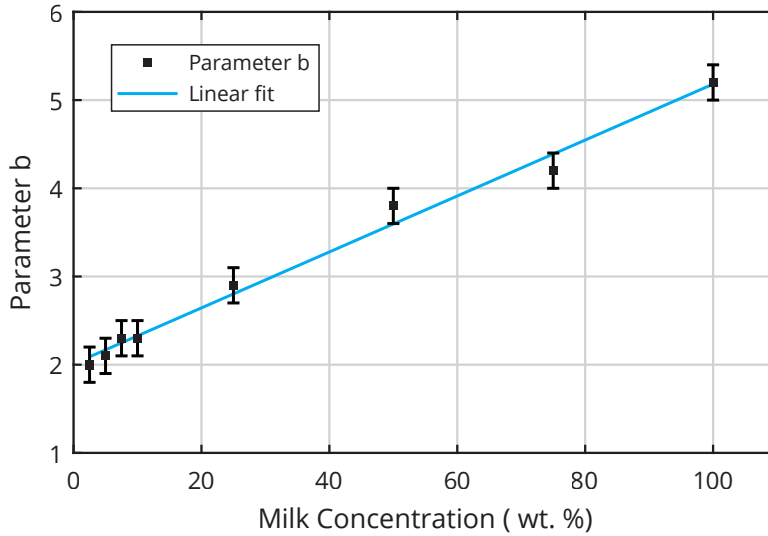
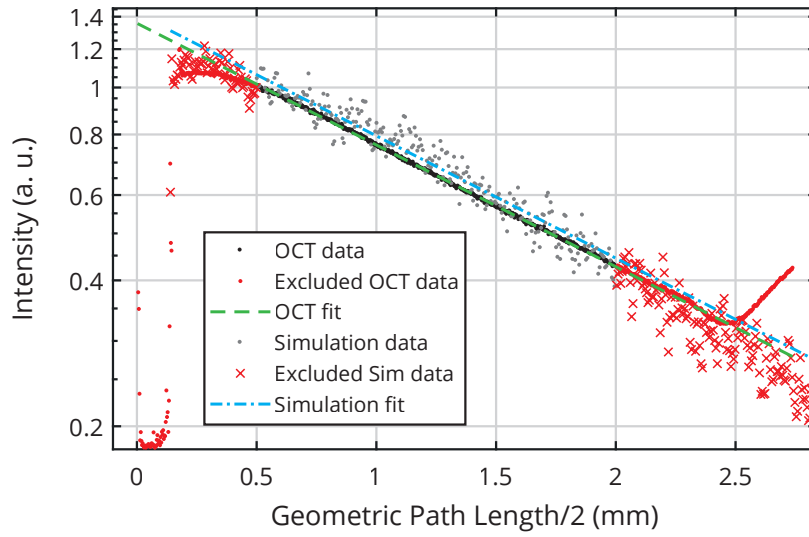


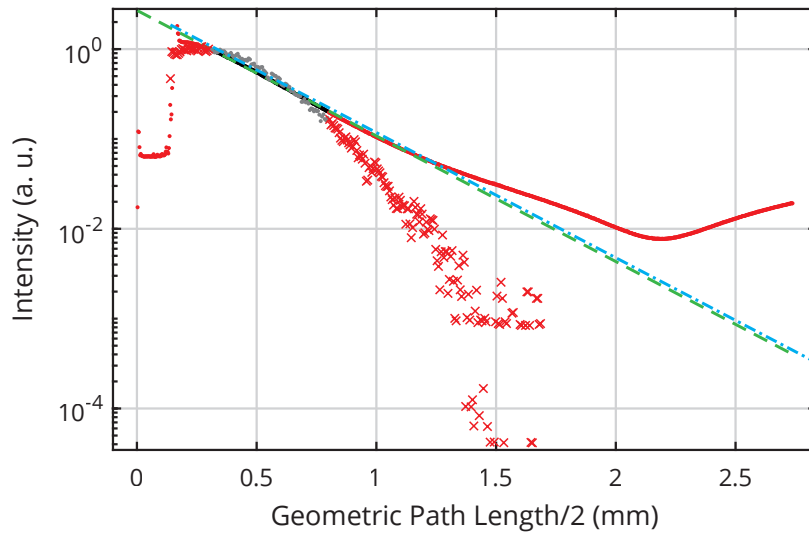
Figure 5.7: Linear dependence of parameter b (considered scattering events) on concentration of scatterers for fixed $a = 5$ (sharpness of the number of scattering events, see Figure 5.3), proving the predictability of μ_s^{OCT} . [61]

lead to good agreement of the respective fit results, but the quality of the fit drops significantly.

The fit of the simulated and measured OCT signal slopes differ from the initially assumed linear dependence between μ_s and the milk concentration and rather show a non-linear behavior. In Figure 5.9, the final result of the simulations in comparison to the measured OCT data is presented. Although dependent scattering is not explicitly considered in the physical model, it is possible to obtain a good estimate of the expected μ_s for an OCT measurement at a certain concentration and a given anisotropy factor g due to the introduced and trained weighting function F_w .



(a) 10 % Milk, $\mu_s^{\text{LIN}}=5.4 \text{ cm}^{-1}$



(b) 100 % Milk, $\mu_s^{\text{LIN}}=54 \text{ cm}^{-1}$

Figure 5.8: Comparison of fitted measurement (OCT data, black) and fitted simulation (Sim data, gray) and their fits (green dashed line for OCT, cyan dash-dotted line for simulation data) for a milk concentration of 10 % (top) and of 100 % (bottom). The ROI, where a good fit of the simulated data can be achieved, is reduced for larger concentrations. [61]

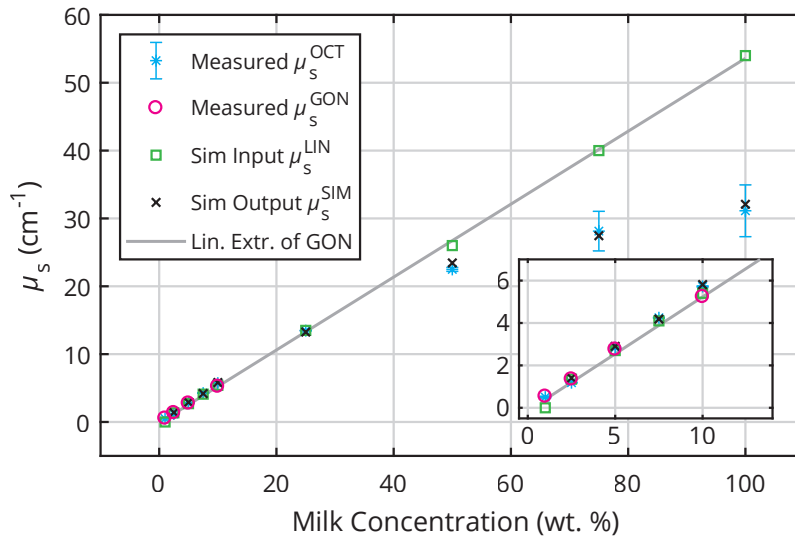


Figure 5.9: Comparison of goniometer measurements μ_s^{GON} , simulation input data μ_s^{LIN} (green) linearly extrapolated from these measurements, Sim output μ_s^{SIM} (black) and OCT measurements μ_s^{OCT} (cyan). The gray line is a linear extrapolation from the goniometer measurements as a guide to the eye. The inset shows a magnified part of the data for low milk concentrations where μ_s^{OCT} and μ_s^{GON} similar. The scattering coefficients obtained by simulation are in good agreement with the OCT values, which are more and more differing from the linear extrapolated values for larger concentrations. [61]

5.3 Discussion

The freely available GPU MCML code was optimized for detection of backscattered photons. Due to the fact that the number of detected photons decreases significantly for very weakly scattering media, further photon accumulation was implemented in the code. In the framework of the presented model, light scattering is described by Mie-scattering of photons inside a turbid medium with given scattering coefficient μ_s and anisotropy factor g . In addition, multiple scattering is taken into account but dependent scattering is explicitly omitted within the presented physical model as described in [54]. Instead, a new simulation approach which is based on a weighting function reducing the weight of multiple scattered photons according to the number of scattering events is introduced.

This approach implicitly accounts for dependent scattering while reducing the numerical effort compared to more complex physical models such as the extended Huygens-Fresnel approach. By investigating the simulation results with different parameters of the multiple scattering weighting function, this method is able to reproduce OCT measurement results with minimal assumptions. A suitable choice of

weighting function with a shape similar to the well-known Fermi-Dirac distribution in statistical quantum mechanics depends on only two simulation parameters a and b . When parameter a is fixed, parameter b shows a linear dependence on concentration. This makes the degradation of the measured μ_s^{OCT} predictable for higher concentration.

Although the presented experimental and numerical results are in good agreement, the deviation between OCT measurement results and simulations increases slightly for higher concentrations. However, the difference is well within the standard deviation of the OCT measurements, which also increases for higher concentrations as shown in Figure 5.7. This is caused by a decrease of the ROI's length used to determine the exponential decay as μ_s increases. In addition, the model is limited since it deliberately does not include dependent scattering or the influence of OCT beam broadening due to scattering. Both effects can be included by Percus-Yevick based models [64] or the extended Huygens-Fresnel approach [56], respectively. However, even when omitting physical effects included in the latter models but leading to a tremendous numerical effort, the model presented in this work yields a good agreement between numerical results at low numerical costs. Also, the model requires knowledge of the anisotropy g and, hence, its measurement is needed. This is easily feasible for low concentration, e.g., via a goniometer as done in Section 5.2. A more crucial point is the training of the weighting function which has to be done with a few OCT measurements. Note that no big variation for a and b for similar anisotropies g are expected.

At the current stage, by using this model, it is possible to simulate OCT A-scans obtained on a multilayer phantom with different anisotropy g for each layer. However, the measurement of such a structure is not feasible with a goniometric setup. It would lead to an effective anisotropy g_{eff} which is a compound of the different anisotropies. On the other hand, mixed samples with different scatterers (e.g. beads with different sizes) can only be modeled with the MCML approach by using an effective g . Nevertheless, real OCT measurements only detect the difference in μ_s , even though different values for g could influence the predictability of the signal.

However, as the model is kept very simple, i.e., based on simulations with given parameters within the range of scattering coefficients shown the reproducibility and predictability should be preserved.

This simplified Monte-Carlo based numerical model to describe light transport in biological tissue is capable of simulating OCT A-scans in homogeneous scattering semi-infinite media in various scattering regimes. In summary, using this approach, it is possible to predict the non-linear concentration dependence of the scattering coefficient μ_s for different concentrations of a homogeneous sample with specified anisotropy g . For that, it is only necessary to measure μ_s in the linear regime and use that as input value for the simulation at higher concentration once the weighting function is known. As far as it is known, this approach for the first time allows to

utilize the well-established MCML software to implicitly include dependent scattering without the need for complex changes to the software. This enables to easily simulate scattering in strongly scattering tissue using the MCML software.

“By three methods we may learn wisdom: First, by reflection, which is noblest; Second, by imitation, which is easiest; and third by experience, which is the bitterest.”

— Confucius



Chapter 6

Preclinical studies

6.1 Histopathology, a gold standard

In dermatology, histopathology is used as the gold standard for ex-vivo determination of skin infiltration depth of malignant melanoma and analysis of many other skin diseases. It is invasive since a biopsy of the skin is needed to prepare a specimen for examination. First, the tissue is fixed by chemical agents (e.g. formaldehyde) to stop all biological processes of the cells. After dehydration and clearing up all chemicals the tissue is infiltrated by and embedded in paraffin. This paraffin block is cut and sliced by a so-called microtome into thin sheets with a thickness of few micrometers. Due to poor contrast the biological tissue has to be stained to emphasize the pathologically relevant cell structures. For skin, mostly hematoxylin and eosin (H&E) stain is used to dye the cell nuclei and collagen fibers. The stained slice is analyzed with a microscope by a histopathologist or a histotechnician to retrieve information about pathogen anomalies, i.e. the cell morphology.

In the following, histopathology is used as reference to compare the performance of the presented devices.

6.2 Thickness determination of melanocytic lesions with OCT and high frequency ultrasound

The past decades have seen rapid progress in the development of non-invasive methods for skin cancer diagnostics and tumor margin detection. Particular interest is drawn to cutaneous melanoma, as it is by far the most aggressive and deadliest skin cancer [1], and easily accessible. Early diagnosis and rapid and complete surgical excision of melanoma are essential for survival as a metastasized melanoma is still not curable. Today, melanoma diagnostics consists of initial visual inspection, usually resulting in numerous false positive diagnoses, and post-excisional histopathological verification.

Both stages rely on well-trained and experienced medical staff. Histopathology is invasive, time consuming and does not provide information about longitudinal dimensions of the lesion, but it can identify tumor tissue morphologically and measure the infiltration depth of the tumor. The depth is the main criterion for determination of the appropriate safety margin for curative surgery (see Table 2.1): 1 cm for a thickness of 1.01 mm to 2.00 mm, 2 cm for a thickness between 2.01 mm to 4 mm [2]. If this thickness could be determined before the first excision, the number of repetitive surgeries may be reduced. Thus, there is an urgent need for a fast, non-invasive, and objective technique for preoperative melanoma depth assessment, in particular, in view of the rapidly increasing incidence of melanoma.

Several non-invasive techniques have been applied to melanoma margin detection and differential diagnosis so far: high frequency ultrasound (HFUS) [3–6], as well as a variety of optical methods such as fluorescence spectrometry, Raman spectroscopy, confocal microscopy, OCT and reflectance spectrometry, see [7], as they are all non-invasive and, therefore, potentially superior to the current gold standard. Out of all these modalities, HFUS and OCT have been shown to be the most useful in depth detection, despite the fact that they cannot help to distinguish an atypical nevus from a thin melanoma. In this study melanocytic nevi suspicious for malignancy were investigated. Albeit not specifically employed as diagnostic tools, both techniques may improve preoperative planning (appropriate safety margin, necessity of sentinel node biopsy) and prevent repetitive surgical interventions.

Note that statistically only roughly 5% to 10% of all suspicious lesions are malignant melanomas. In the remainder it is referred only to suspicious melanocytic lesions without further assessment of malignancy. With OCT and HFUS as used in this work it is not possible to distinguish between malignant melanoma, basal cell carcinoma, dysplastic nevi or other skin cancer types or benign skin lesions.

In 2003 a related work was published by Vogt and Knüttel [65] where measurements using 100 MHz HFUS and OCT at a central wavelength 1300 nm were compared but, in contrast to this work, without histopathology as reference. Furthermore, measurement and imaging techniques evolved significantly since 2003 improving resolution and contrast. Hence, these recent advances demand for new studies on the comparison of HFUS and OCT with histopathology as the gold standard.

Today, HFUS is a well-established, frequently used technique for preoperative assessment of melanocytic lesion thickness. In dermatology, high-frequency scanners of 10 MHz to 50 MHz are usually used to image the skin morphology [3, 5, 6, 66, 67]. Scanners of 75 or 100 MHz have hardly been evaluated so far. The image contrast is generated by the relative difference in the acoustic impedance of different tissue types. Interpretation of images needs to be performed by well experienced medical staff in order to interpret hypoechoic and hyperechoic tissue correctly. For quantitative measurements of lesion depth, the run-time of the ultrasound signal is multiplied by the speed of sound in the tissue (for the ultrasound frequency used). Ultrasound

scanning heads have been inferior to OCT imagers in measuring thin melanocytic lesions due to their lower depth resolution, which resulted in overestimation of the depth of thin lesions (< 1 mm) [4, 6] and would lead to excessive surgical margins in case of a melanoma. However, recently developed 100 MHz ultrasound scanners perform considerably better [4] and have the potential to challenge OCT in thin lesion thickness determination.

Thus, OCT is a rival to HFUS for preoperative non-invasive melanoma margin assessment. Recent improvements of OCT technology enable cellular resolution at the cost of scanning depth [68]. This so called high definition optical coherence tomography (HD-OCT) facilitates a path to an all-optical diagnostic device [69–72]. However, with regard to infiltration depth OCT is working well for thin lesions due to higher depth resolution, but usually failing for thick lesions (> 1.0 mm) because of its insufficient penetration depth [65–67]. The OCT contrast results from relative changes in the refractive index of the tissue and measures an optical path length (see Chapter 3.3). This quantity needs to be divided by the skin tissue refractive index to calculate the actual lesion thickness, while for HFUS the depth estimation is determined by the implemented (fixed) speed of sound.

Despite rapid progress in OCT development in the past decade, the technique is still not convincing enough to become popular in clinical dermatology. More and more systematic studies are emerging to quantify the accuracy and reproducibility of OCT measurements.

In general, the different techniques utilized for non-invasive depth assessment of melanocytic tissue so far have complimentary capabilities with regard to penetration depth, resolution or range of operation. Currently, it can be assumed that one technique alone will not be able to reliably determine the lesion depth for a wide range of thicknesses non-invasively, and, therefore, a combination of such techniques might be a more promising route to realize such a system as presented in Chapter 8.

This chapter presents an initial preclinical study comparing two up to date devices for *in vivo* presurgical determination of melanocytic skin infiltration depth. Measurements by a 1300 nm spectral domain OCT and a 100 MHz HFUS device were validated and their performance was compared with histopathology. The clinical value and applicability of the methods for future non-invasive melanoma depth detection is discussed, contradicting the findings in previous studies with lower frequency HFUS [6] and with 930 nm OCT [67].

6.3 Materials and methods

6.3.1 Patients

A group of 14 female and 10 male patients with a total of 32 melanocytic skin lesions, suspicious for malignancy, was recruited for a first pilot study. The patients were scheduled for surgery after initial visual inspection at the Clinic for Dermatology, Venereology, and Allergology of University Medical Center Göttingen and at the Clinic for Dermatology and Venereology, University Medical Center Rostock. Suspicious lesions were imaged by OCT and HFUS after patients had given their informed consent. Image planes for OCT and HFUS B-scans were defined by the histopathologist before surgery to ensure optimal agreement of the image planes with the expected histopathological section.

The imaged lesions underwent subsequent routine histopathology examination: fixation in formaldehyde, paraffin-embedding, slicing into 4 μm sections, and staining with haematoxylin and eosin (H&E). Two experienced dermatopathologists (S.M.C. Broekaert, S. Schäd-Trcka), blind to the imaging results, provided the histopathology diagnosis, including melanocytic skin infiltration depth or Breslow lesion thickness, respectively.

The study was approved by the Ethics Committee of the University Medical Center Göttingen (3/3/15) and the Ethics Committee of the University Medical Center Rostock (A 2016-0115) and met the principals of the Declaration of Helsinki.

6.3.2 Imaging devices

A spectral domain OCT imaging system (Telesto-II, 1300 nm central wavelength, Thorlabs GmbH, Germany), equipped with an LSM-03 objective (axial and lateral resolution of 5.5 μm and 13 μm in air, respectively) was used for recording both B- and C-scans of the melanocytic lesions. The scanning beam is of laser class 1M and is not invasive to human skin. The maximal penetration depth of the signal in skin is approximately 1.3 mm, highly depending on the skin structure (e.g. a thick stratum corneum layer results in a high reflection attenuating the signal in the layers below). An attachment to the OCT head was designed to fix the distance between the OCT objective and the patient's skin and to eliminate skin movement artifacts (see Chapter 8, Figure 8.4). It was held by hand and aligned to the excision marks of the lesion using the built in CCD camera.

The real-time HFUS images were recorded with a high-resolution 100 MHz linear ultrasound probe DUB 100-12Bit (tpm taberna pro medicum GmbH, Germany) with axial resolution of 16 μm and sound penetration depth of 0.8 mm to 1.5 mm. The ultrasound device is classified by the MPG (Medizinproduktgesetz) as IIa medical

device. The average power of the ultrasound beam is specified at $<100 \text{ mW cm}^{-2}$. The pulse energy is $< 1 \mu\text{J/pulse}$ with a pulse duration of 2.3 ns and a repetition rate of $< 1 \text{ kHz}$. With correct use no significant heating or damage to the tissue occurs. The probe was held manually perpendicular to the skin surface and moved with minimal possible pressure over the whole lesion recording real-time B-scans. The B-scan corresponding to the excision mark was recorded and the thickness was measured at the point of the visually highest lesion depth.

The probe had to be filled with water as acoustic medium between transducer and skin. The maximal field of view is limited to 10 mm for OCT and 12.8 mm for HFUS. The maximal scanning depth of the OCT depends on the refractive index and amounts to 3.5 mm for air and 2.7 mm for skin. It is thus superior to HFUS (2 mm in tissue). However, in practice the light penetration depth for OCT is less ($\approx 1.3 \text{ mm}$) and comparable with the sound penetration depth of HFUS.

6.3.3 Image processing

Image processing is often required for better determination of the infiltration depth of the melanocytic lesion in OCT and favorable even if the tissue structure already appears quite clearly in live-view imaging. Figure 6.1 shows OCT images for two different cases: in the left column (I), image processing is necessary to find lesion margins whereas in the right column (II), the margins can be well discriminated even without any image processing. Arrows point to the dermoepidermal junction or the lesion margins, respectively. The image processing was based on the approach described in [73] and performed in several steps. First, contrast was enhanced by means of histogram equalization as shown in Figure 6.1, (row b), then the rotating kernel transformation [74] was applied to the contrast enhanced images, see Figure 6.1 (row c). In the last step, thresholding was applied to remove noise and improve clarity and contrast of diagnostically relevant image features for the eye, Figure 6.1 (row d). The bottom images of Figure 6.1 show a clear improvement in image quality and contrast in comparison to the raw images. All image processing routines were implemented in a MATLAB script.

No additional post-processing was needed for the HFUS images since the standard HFUS signal processing and image enhancement is already implemented in the proprietary measurement software. However, a slight Gaussian smoothing was applied to the acquired image to soften the pixel noise.

OCT images were corrected for the mean refractive index of skin, $n = 1.36$ for a wavelength $\lambda = 1300 \text{ nm}$ taken from [75] to obtain the true depth dimensions for later assessment of lesion depth. For HFUS images, distances and depths dimension could be adopted directly from the ultrasound probe, as they were already calculated with the speed of sound in skin of $c = 1580 \text{ m s}^{-1}$, which is in good agreement with

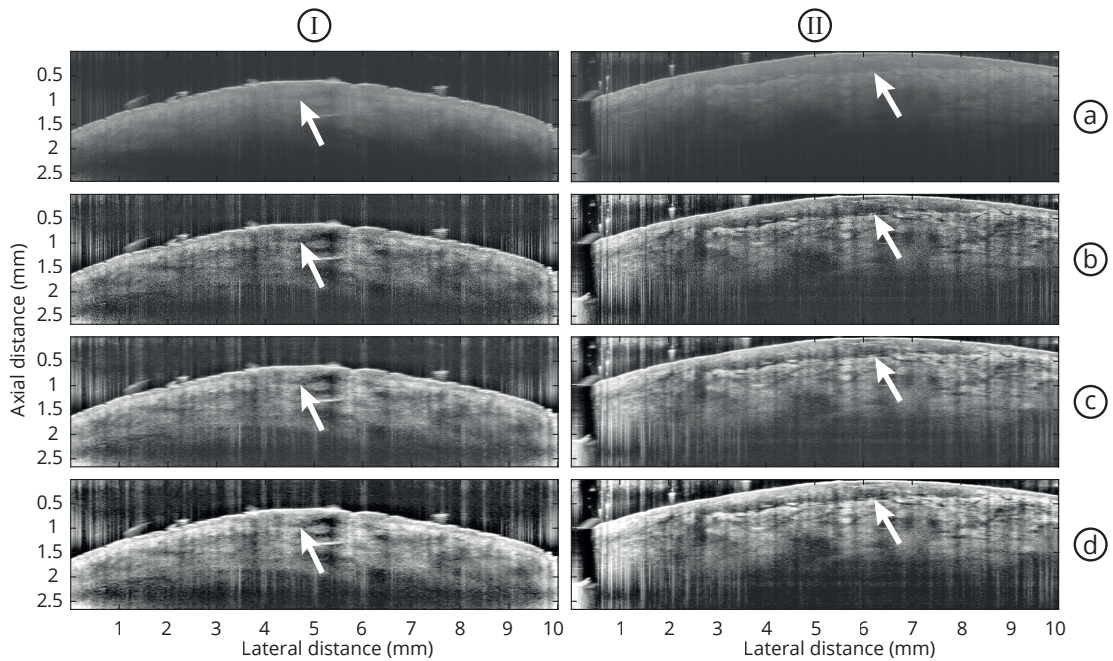


Figure 6.1: Consecutive OCT image post-processing of two representative lesions (columns I (poor contrast) and II (good contrast)). Row (a) unprocessed, (b) after contrast enhancement by CLAHE, (c) after rotating kernel transform, (d) after thresholding. The dermoepidermal junction is marked by arrows, respectively. [8]

the reported values for epidermis and dermis [76, 77]. A separate MATLAB script was used to determine lesion thickness by measuring the pixel distance where one pixel in z direction (in skin) corresponds to $2.6 \mu\text{m}$ for both OCT and HFUS. The pixel resolution is higher than the axial resolution of the devices ($5.5 \mu\text{m}$ for OCT and $16 \mu\text{m}$ for HFUS). The error due to the pixel measurement is up to ± 3 pixels, depending on the magnification of the image on the screen. The processed OCT and ultrasound images were given to several independent researchers who were asked to measure the lesion thickness using the data exemplified in Figure 6.2.

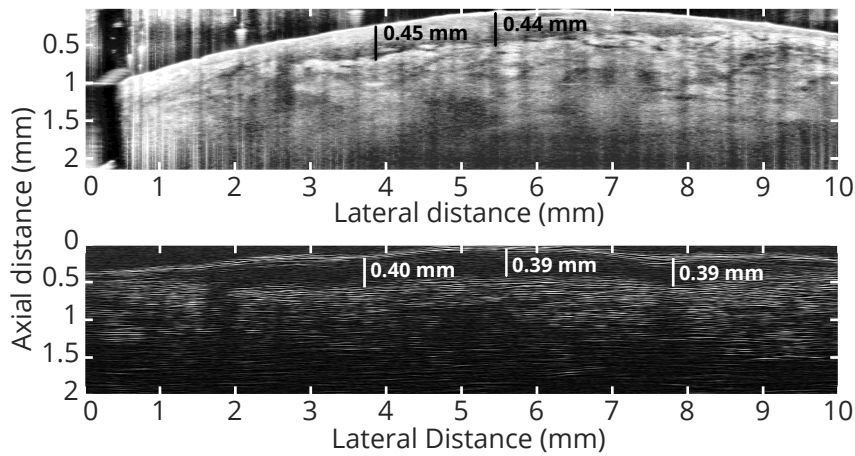


Figure 6.2: Example of the depth determination of a representative melanocytic lesion (same as Fig. 1 II): (top) post-processed OCT image, (bottom) Gaussian smoothed HFUS image. [8]

6.4 Results and discussion

Histopathology of skin is the reference standard to which both modalities, HFUS and OCT, are compared to. However, it has to be kept in mind that the whole process of histopathological preparation (excision, fixation, paraffin embedding and slicing) is error-prone. Typically a 10% error is assumed for thickness assessment. A recent study of uncertainty of Breslow thickness measurements is presented in [78]. The following estimation of the skin infiltration depth with HFUS and OCT follows the principles and rules of histopathology measuring the maximal vertical distance from the interface of stratum corneum and stratum granulosum to the dermal epidermal junction.

In contrast to the histopathology with dying agents, no cellular resolution is achieved, since small clusters of melanocytes with sizes below the axial resolution are not detected. Thus, small branches of melanocytes might not be detected correctly. Note that axially grown branches are detectable, at least partially, once their axial dimension exceeds the OCT and HFUS resolution limits. Nevertheless, the dimensions of a skin lesion can be determined by HFUS and OCT preoperatively by detecting the visible boundaries and evaluating their axial distance. This enables for risk evaluation based on lesion thickness similar to histopathology. In particular, these techniques are able to measure if the Breslow thickness exceeds the 1 mm safety limit [1].

The HFUS image of a melanocytic lesion (see Figure 6.2, bottom) shows a homogeneous hypoechoic mass with no internal structures and well-defined margins created by hyperechoic stratum corneum and healthy dermis tissue [3, 67]. Images of

benign lesions are similar to melanoma sonograms. The OCT image of a lesion shows a blurry but well recognizable dermoepidermal junction zone with patchy reflectivity of the papillary dermis. The researchers assessing the lesion depths in the images reported no difficulties in recognizing structures relevant for the depth determination for both imaging modalities, as long as the dermoepidermal junction was visible. Examples of the processed OCT and HFUS images with lesion depths measurements are presented in Figure 6.2, (top) and (bottom), respectively.

As in histopathology, the maximal vertical distance between the topmost skin layer and the dermoepidermal junction was taken as the lesion depth for each image. The lateral dimensions of the lesions are of subordinate relevance, as the Breslow thickness is the main criterion for safety margins for the excision. In addition, the lateral field of view is limited, such that for wider lesions multiple measurements might be necessary.

For the lesion shown in Figure 6.2, the largest measured distance between stratum corneum and the dermoepidermal junction is 0.45 mm (OCT) and 0.4 mm (HFUS), respectively. Figure 6.3 shows the histopathologic section corresponding to the OCT B-scans in Figure 6.1 (II) and Figure 6.2 stained with H&E (top) and Melan-A (bottom), respectively. In this example, the histopathologically determined penetration depth is 0.5 mm (H&E stained), which is in good agreement with OCT and HFUS. Melan-A stained samples were not available for all excised lesions, and thus not used for infiltration depth measurement in this work. Slight differences between the lesion

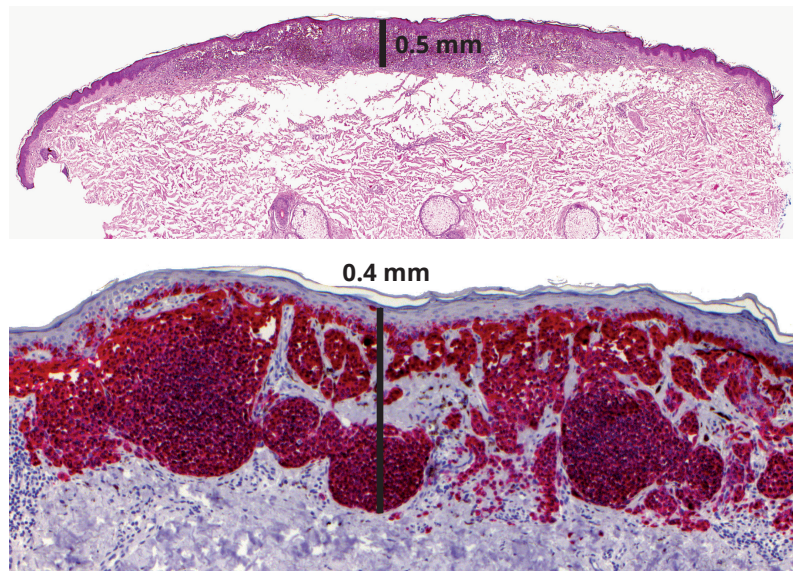


Figure 6.3: Histology of the melanocytic lesion shown in Figures 6.1 II and 6.2: (top) H&E stained (x40), used for histopathological measurement of infiltration depth in this work and (bottom) after staining with Melan-A (x100). [8]

depth determined by H&E or Melan-A stains as shown in Figure 6.3 are mainly caused by the different contrast of the dyes. In addition, every histopathological step modifies the sample dimension mechanically and chemically, whereas *in vivo* measurements rely on known parameters like refractive index or speed of sound in skin. As mentioned in section 2.1 it was tried to image the same region, or the same slice in particular, for all three modalities. However, histology, HFUS and OCT measurements do not match exactly but are similar in structure and layer thicknesses. Nevertheless, in histopathology, a particular representative slice is chosen as well. In addition OCT provides 3-D images where the slice with the thickest lesion part can be chosen.

Figure 6.4 shows the OCT measurement and histology of a lesion with a thickness of about 1 mm. There, the previously described mechanical deformation of the histology can be seen when compared to the *in vivo* image. The dermoepidermal junction is clearly visible which means that this important region (1 mm) for the thickness assessment is covered very well.

The results of all evaluable lesion measurements (21 of 32) performed in this study are presented by Bland-Altman plots for the OCT measurements (Figure 6.5(a)) and the HFUS measurements (Figure 6.5(b)). These plots show the difference and mean difference between melanocytic cell infiltration depth deduced from histopathology and lesion margins measured using OCT and HFUS, respectively. Six lesions from the data set were too thick (1.29, 2.49, 2×2.7 , 3.4 and 3.55 mm, respectively) for the depth detection for both OCT and 100 MHz HFUS, and were excluded from the dataset presented in Figures 6.5 and 6.6. One lesion was not excised and three other lesions (including one 3.4 mm thick melanoma) were not accessible with the HFUS applicator. Another lesion was diagnosed as basal cell carcinoma with a thickness

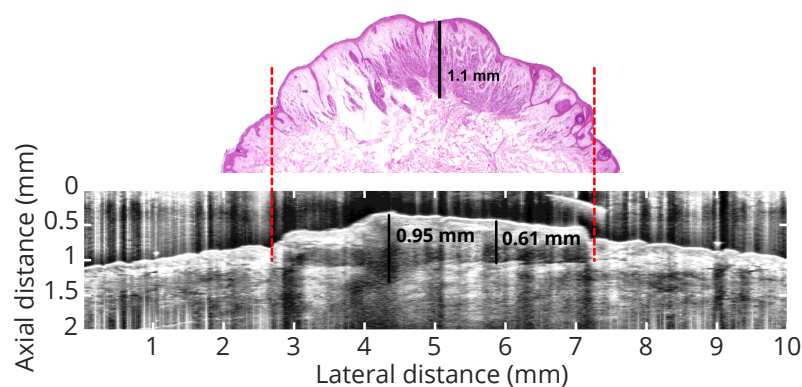


Figure 6.4: Comparison of histology and OCT measurement of a lesion with a thickness of approximately 1 mm. The corresponding region is marked by the red dashed lines. [8]

of 0.67 mm. There the dermoepidermal junction was not visible with HFUS so that this measurement was excluded. Out of 31 excised lesions three were diagnosed by histopathology as malignant melanomas with thicknesses of 3.4, 0.14 and 0.50 mm, respectively. The latter is also included in Figures 6.1-6.3, 6.5 and 6.6. In this case the melanoma showed the best contrast for both modalities, which is why it was chosen here as example. In Figure 6.1, left column, the lesion with the poorest OCT contrast is shown as well. However, a general statement if the contrast for melanomas is better than for non-melanoma lesions is not possible at this stage. Nevertheless, these measurements prove the applicability of the presented modalities for thickness assessment of melanocytic lesions in general (e.g. nevi and melanomas). For comparison, Figure 6.6 shows the measured lesion thickness using OCT, HFUS and histopathology containing the non-melanoma and the melanoma cases. The measurement data are sorted according to increasing thickness which was determined from histopathology as the gold standard. The determined thickness is in good agreement for all three modalities up to a lesion thickness of 0.6 mm. For small thickness (< 0.2 mm) both, OCT and HFUS, overestimate the thickness slightly. For larger thickness (> 0.7 mm), OCT as well as HFUS underestimate the thickness compared to histopathology.

The speeds of sound and light in human skin are crucial for the correct estimation. They were adopted from literature [75–77] as mean values. Even though this assumption leaves some space for variance, the difference from overestimation in other publications with lower ultrasound frequencies, previously cited, is significant. On average, the mismatch between OCT and histopathology is -0.020 mm while the average deviation between HFUS and histology (-0.071 mm) is slightly higher but still in good agreement. Also, the 95 % limits of agreement estimated by the mean difference and standard deviation (SD) of the respective difference values are shown. The region of agreement for OCT (0.48) is slightly smaller than of HFUS (0.72). So, OCT is slightly more accurate than 100 MHz HFUS in depth determination of melanocytic lesions. For both modalities, the measured data suggest that underestimation increases with thickness. However, this observation is not statistically significant based on the measurements presented in this work so far and needs to be substantiated or rejected based on data from more lesions thicker than 0.8 mm.

HFUS images display better contrast and skin lesion imaging capabilities and do not need further image post-processing, which is often required for the OCT images. OCT has the additional benefit of being combined more easily with other optical and non-contact modalities with complimentary capabilities such as optoacoustics, to also enable accurate depth determination of thicker melanomas, and Raman spectroscopy as a potentially relevant diagnostic tool (see Chapter 8). From the data, it is concluded that OCT and HFUS might be suited for reliable *in vivo* preoperative tumor depth determination, improve preoperative planning (size of

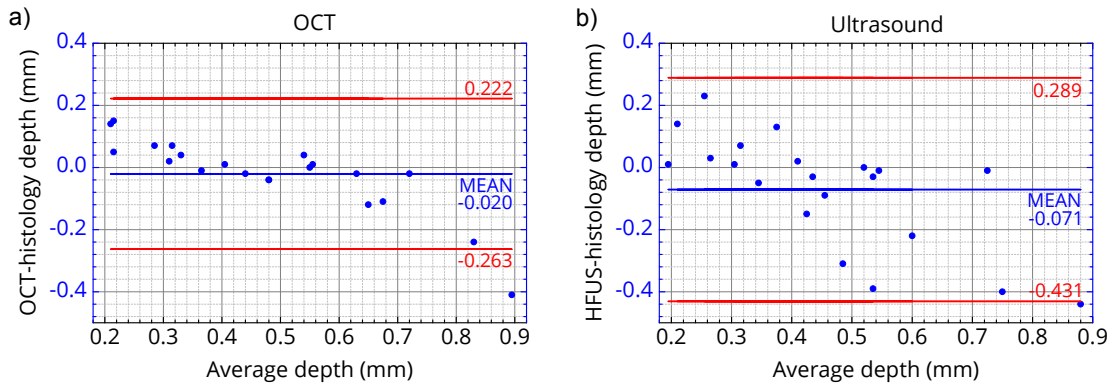


Figure 6.5: Bland-Altman plots: a) OCT measurements, b) HFUS measurements. Blue lines: mean difference between measurement and histology, respectively. Red lines: 95% limits of agreement estimated by mean difference \pm standard deviation (SD) of the difference. [8]

safety margin, necessity of sentinel node biopsy) and prevent repetitive surgical interventions. However, the implications of this pilot study have to be confirmed by larger clinical studies focusing on thickness determination of lesions or melanomas utilizing OCT and/or HFUS which will be conducted in future work.

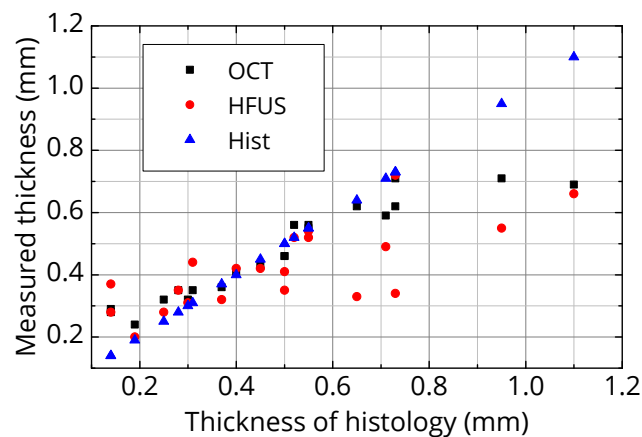


Figure 6.6: Measured lesion thickness as determined by OCT, HFUS and histopathology; data is sorted according to increasing thickness measured by histopathology (gold standard). [8]

6.5 Conclusions

For a comparison of the applicability of HFUS and OCT for lesion thickness determination a preclinical pilot study with 21 different lesions was presented, where 19 non melanoma and two melanoma cases are included.

OCT has a slightly better axial resolution than 100 MHz HFUS (5.5 μm and 16 μm , respectively). The OCT lateral resolution depends on the optics used for scanning and is by far better than the lateral scanning resolution of HFUS. However, the contrast of the lesion to surrounding tissue is better with HFUS. OCT images require post-processing to extract desired features and enhance contrast. With appropriate processing the contrast of OCT is increased and can keep up with HFUS.

100 MHz HFUS has limited penetration depth, similar to OCT, and both cannot determine the thickness of a lesion (such as nevi or invasive melanomas) reliably if it is larger than 1 mm.

The good performance of the 1300 nm spectral domain OCT in terms of thickness determination contradicts the poor performance of the OCT at 930 nm reported in [67]. OCT systems with higher wavelength (≥ 1300 nm) have higher penetration depth and a better sensitivity in skin, and therefore are better suited for thickness determination of lesions than 930 nm OCT. Also, in [67] a different refractive index of 1.33 was used to correct the depth signal (instead of 1.36 as in this work). The former is closer to the refractive index of pure water than to skin tissue at the used wavelength underscoring the importance of a careful choice of this scaling parameters in OCT – the same is true for the a correct speed of sound in HFUS.

Reliable *in vivo* measurements of skin lesion infiltration depth could provide an additional reference for tumor thickness evaluation in the future. Combining these *in vivo* data and the histopathology standard could help minimizing errors in tumor assessment. This work substantiates the suitability of OCT for reliable depth measurement of melanocytic lesions like nevi or melanomas below 1 mm. In addition, being an optical method, it lends itself for combination with other optical and in particular non-contact methods which appear more suited for thicker melanomas such as optoacoustics and, in addition, with Raman spectroscopy in order to add a diagnostic tool. HFUS cannot easily be combined with those methods, since the ultrasound transducer is not transparent.

Therefore, in the light of the presented results, Chapter 8 will focus on combining OCT with optoacoustics and Raman spectroscopy and use the hybrid method to establish an all-optical biopsy for suspicious skin lesions such as melanocytic dysplastic nevi or cutaneous melanoma in order to reduce the number of surgical interventions as well as unnecessary wide surgical margins for primary excision.

“I use a computer. I don’t know if that qualifies me as a techie, but I’m pretty good on the computer.”

— Leonard Nimoy



Chapter 7

Lesion segmentation

In the preclinical study in Chapter 6 the thickness assessment of the lesion was performed visually on cross-sectional OCT images. The match between histopathologic slice and OCT slice is not guaranteed, neither is it certain that the histopathologic slice shows the thickest lesion part. During the clinical measurements not only OCT lesion slices were obtained but also volumetric data. In this chapter an automated layer detection algorithm is presented for 2-D and 3-D image segmentation and thickness assessment.

Various segmentation algorithms were reviewed to find the most appropriate tool for the problem of lesion segmentation. The first approach was to use algorithms proven to work for retinal or corneal segmentation in ophthalmology [79]. However, the contrast differences of the different layers are much less for skin, in addition the skin layers have significant structures themselves intervening in this kind of algorithms. The next step was to use different image enhancement techniques and standard methods like e.g. Canny edge detection [73, 80, 81]. Again, the different structures of skin layers and skin types were disturbing. On the other hand, algorithms for tissue feature detection as in [82] lack for proper layer detection, which is clear due to a different focus. A very promising work showed a volumetric segmentation of skin [83], but it required realignment of the A-scans and a plano-parallel skin structure, which is mostly not given for lesion like melanoma.

The obvious result was to implement a custom algorithm inspired by Koozekanani et al. [84] for segmentation suited for the purpose of thickness assessment of lesions with a varying thickness of the epidermal layer. In the following sections the algorithms for 2-D and 3-D OCT image segmentation are presented.

7.1 2-D-segmentation of cross-sectional OCT lesion data

2-D OCT data used in this work is stored as x-z-matrix in a binary Thorlabs format (*.oct). Each data point is a 10 bit value representing a scattering intensity at a certain lateral (x) and axial (z) position. When the matrix is plotted as image with the data points as gray scale pixel a cross-sectional image of the specimen is revealed as presented in the previous chapters. In the following the algorithm is described and used to retrieve the upper skin interface and the dermoepidermal junction (DEJ) layer as 2-D curves. The whole program is implemented in MATLAB and consists of multiple script files containing different functions. The essential parts will be explained thoroughly.

First, the acquired OCT data is loaded by a customized script based on the Thorlabs software development kit (SDK) provided together with the Software of the measurement device. Not only the image but also relevant measurement properties (sizes and spacings) are stored to a container structure (so called `struct`) `OCT`. With

```
handle = OCTFileOpen(OCT_file)
```

a reference handle to the OCT file is opened for reading. Different properties can be retrieved via

```
OCT.prop.SizeX = str2double(OCTFileGetProperty(handle, 'SizeX'))
```

and stored to variables in the `struct` (here `SizeX`). `SizeX` and `SizeZ` give the matrix dimensions and the spacings (`SpacingX` and `SpacingZ`) are needed for the correct transformation of the axes to real units. The cross-sectional image is read by the command

```
OCT.data = OCTFileGetIntensity(handle)
```

Finally, the reference to the file is closed by `OCTFileClose(handle)`. The full code is printed in Appendix B.1.

Having the data stored in a workplace variable further processing is performed by the function `LayerDetection2D` on the OCT structure (see Appendix B.2). First it calls the `boundary_detection` (see Appendix B.3) function to detect and collect all boundaries from the data referred to as `Image`.

```
nhood = 55;  
boundaries = boundary_detection(Image, nhood);
```

`nhood` is a comparison parameter denoting the pixel size of the neighborhood and will be relevant later on. To begin with the detection all peaks (local maxima), are searched and stored within a loop through all A-scans or image columns (`col`), respectively.

```
[peaks,p_locs] = findpeaks(col);
```

Since the A-scan of specimen like skin is very noisy, smoothing is required for proper peak detection. It is achieved by the implementation:

```
sAScan = smooth(AScan,51,'sgolay',5);
```

where `sAScan` is the smoothed A-scan and the parameters of the Savitzky-Golay algorithm are a span of 51 and a degree of 5. Note that in the final implementation an input prompt (the function `sgolay_prompt` is called) asks for the parameters where the given mentioned parameters are preset. Figure 7.1 shows the four most prominent peaks as candidates for boundary detection. This set of peak values (`peaks`) and locations (`p_locs`) is filtered by following successive rules to select the peaks most probably belonging to the interfaces:

1. Select only peaks with positive values $\geq 0.1 \times \max(\text{col})$.
2. Select only peaks with a distance > 10 points to avoid multiple selection of same (double) peak.
3. Select only peaks with an index \geq the index of the global maximum (most probably first layer).
4. Sort peaks by value and take the two highest peaks (`o1` and `o2`).

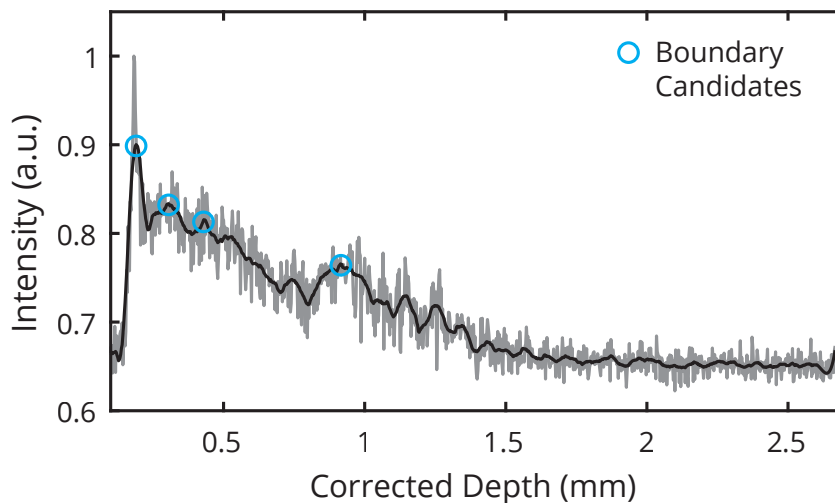


Figure 7.1: Exemplary peak detection on one A-scan. The raw signal (gray) is smoothed (black curve) before peak detection. The peak candidates for boundaries are marked by cyan circles.

Each step uses the data remaining after previous steps. The resulting set of peaks (`o1` and `o2`) is most probably populated by positions of the first boundary (`boundary_1`): the horny layer. The second highest peaks (`o2`) will be considered later.

Now the peak set for the second boundary (`boundary_2`), namely the DEJ, has to be found:

1. Differentiate all A-scans (`col`)
2. Select only peaks with positive values.
3. Select only peaks with a minimal distance to the first boundary `thick_min`.
4. Take each peak location as pivot point and sum all values of left and right hand side within the neighborhood `nhood`. Select only peaks where the right value is larger. The dermis is stronger scattering material and produces larger signal than the epidermis. However, this also might be true for other regions since the tissue is not homogeneous.
5. Select only peaks with a reasonable maximal thickness of the epidermis `thick_max`.
6. Sort peaks in descending order. Select only peaks with values $\geq 0.1 \times \max(\text{col})$.
7. Select only peaks with a distance > 10 points to avoid multiple selection of same (double) peak.
8. Append the global maximum.
9. Sort peaks in descending order. Select at least one peak with the maximal value. If available, select the peaks with the four highest elements (`i1`, `i2`, `i3` and `i4`).

The collected points as candidates for boundaries are depicted in Figure 7.2 with different colors. Note that `o2` and `i1` correspond quite well. Again, `o1` and `o2` belong to a peak detection performed on a smoothed A-scan, which is sufficient for first boundary, whereas `i1` to `i4` were derived from a differentiated smoothed A-scan to highlight the change in scattering. This process is performed for all A-scans as columns of a B-scan such that the resulting set corresponds to one B-scan as presented in the previously shown figures. The function `boundary_detection` ends here and provides the boundary candidates `boundaries` containing `boundary_1` and `boundary_2` for further classification:

```
B = classification3(boundaries,zTol);
```

Here `B` is the container of the detected boundaries and `zTol` is the allowed maximal variation in axial pixel distance between stratum corneum and DEJ from one A-scan to the next one. This is necessary to avoid wrong interpretation of discontinuities of the boundaries and will become clearer during the next steps.

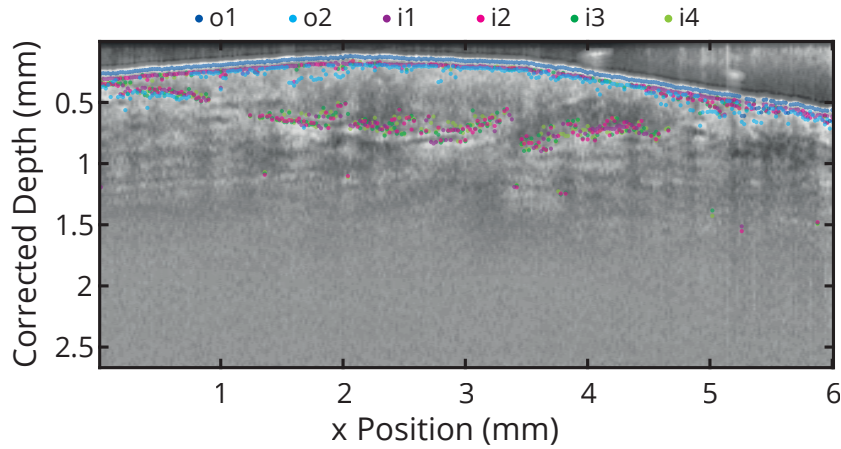


Figure 7.2: First step of boundary detection. Boundary candidates `o1`, `o2` and `i1` to `i4` are printed with different colors (see legend on top).

The classification function (for full code see Appendix B.4) is sorting the candidate points dependent on context, i.e. the positions and values of the adjacent points. Therefore, the following steps are performed, initially for the first boundary (stratum corneum or outer interface):

1. Unify all candidates to an $n \times 6$ array with columns `o1`, `o2`, `i1`, `i2`, `i3` and `i4`.
2. Sort all values of `B` row-wise by ascending order from left to right.
3. Take only values from first column of `B` if z-index not higher than neighbors + threshold while comparing it with a moving average of the column and write them to a new array `B1`.
4. Replace these points in `B` with `NaN`.
5. Sort all values of `B` row-wise by ascending order from left to right. (The `NaN`s are moved to the right.)

The points of the first boundary (air - stratum corneum) now are stored in `B1`. Analogously, this applies to `B2` containing the interface of stratum corneum and epidermis. For the third boundary, the DEJ, the procedure is slightly different. As can be seen in Figure 7.2 most of the points `i1` and `i2` are distributed over both interfaces: stratum corneum - epidermis and DEJ. Thus, a separation of these points in two classes is necessary: `B3_top`, which corresponds to `B2` and `B3_bot` which marks the real DEJ. This is achieved by constructing an upper and a lower hull. All points are categorized depending on the nearest hull: outer boundary `bo`, first inner boundary `bi1` (unifying `B2` and `B3_top`) and `bi3` (`B3_bot`). In Figure 7.3 this classification is shown.

The final segmentation is done by a smooth fit of the classified points:

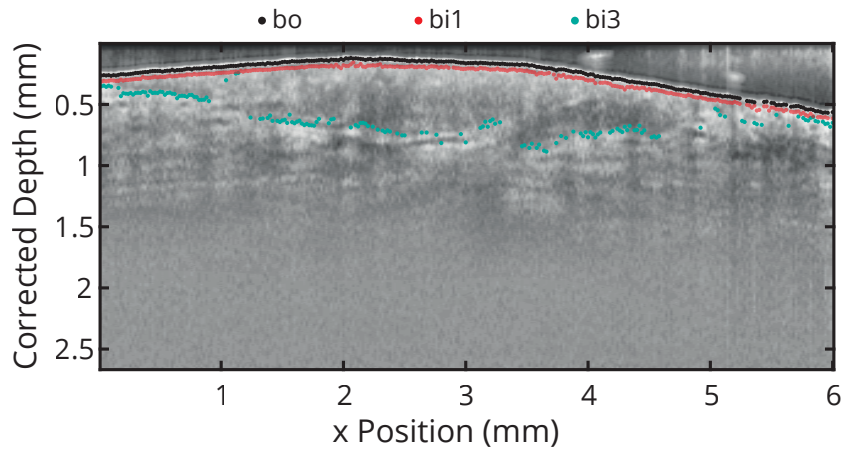


Figure 7.3: Classification of the points to correspond to the different interfaces (see legend on top).

```
% smooth fit of bo
B_out.o_smooth = [outer(:,1),smooth(outer(:,2), 0.15, 'rloess')];
% smooth fit of bi1
B_out.i_smooth1 = [inner1(:,1),smooth(inner1(:,2), 0.15, 'rloess')];
% smooth fit of bi3
B_out.i_smooth3 = [inner3(:,1),smooth(inner3(:,2), 0.15, 'rloess')];
```

The result of the segmentation is presented in Figure 7.4.

The described algorithm for lesion segmentation was applied on B-scans by starting with an iteration over the image columns as A-scans. Based on the neighbors'

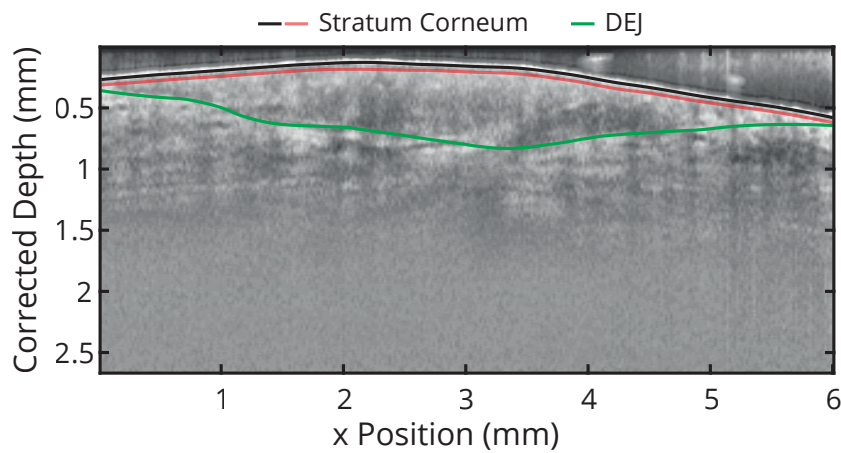


Figure 7.4: Segmentation of stratum corneum (between black and red line) and epidermis (between red and green line).

coordinates the points were classified to match the boundaries. Values like `nhood` and `zTol` might require further tuning depending on the lesion geometry. With `nhood = 55` a good value was found to obtain proper results. Nonetheless, it depends on the lateral field of view and the pixel spacing of the image. For lesion with a strong curvature the `zTol` value most probably needs to be increased. Alternatively, `zTol` can also be described by a function allowing more tolerance where the thickness increase is very steep, e.g.

```
zTol = (sin(linspace(0,pi/2,b_len)).^2*120+30)';
```

see also comments of the full code in Appendix B.4. The smoothing parameter for Savitzky-Golay and RLOESS (robust local regression using weighted linear least squares) smoothing are also variable and can be tuned according to the demands of the measurement data.

As a future step, these parameters might be used to train a machine learning algorithm.

7.2 3-D-segmentation of volumetric OCT lesion data

Segmentation of 2-D-data (B-scan) only gives a correct thickness estimation of the lesion if the slice is chosen which contains the thickest part of the epidermis. A 3-D-segmentation not only provides all slices within the lateral field of view of the OCT measurement but also gives access to the full lesion geometry.

Therefore, the 2-D-segmentation is looped through all slices of the volumetric OCT measurement data along both lateral dimensions (see Appendix B.5 for full code). The gathered boundary points are fitted by the three-dimensional `gridfit` function (version 1.1, by John D'Errico) providing a surface fit as applied in Figure 7.5. From the two surfaces a thickness map can be calculated by simple subtraction of the axial values (depth). In Figure 7.6 the resulting thickness map, an 2-D-array of thickness values, is plotted. The maximal lesion thickness is the global maximum of the 2-D-array or the thickness map, respectively. After binarization of the image

```
ThickBin = imbinarize(Thickness, M/2);
```

with the threshold $M = \max(\text{Thickness})$ and measuring the region properties of the binary image via

```
ElSel = regionprops(ThickBin, 'Orientation', 'MajorAxisLength', ...
    'MinorAxisLength', 'Eccentricity', 'Centroid');
```

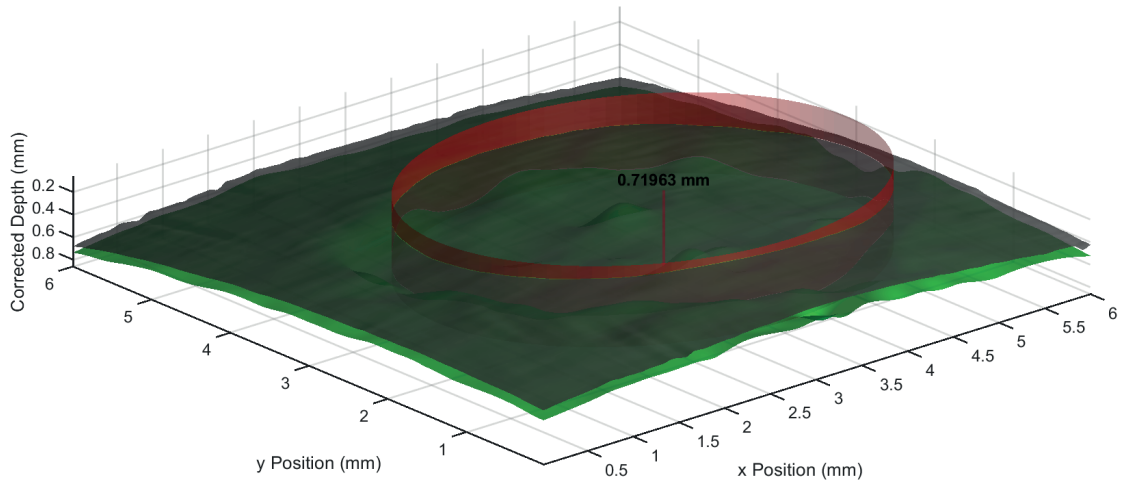


Figure 7.5: 3-D-segmentation of a melanocytic lesion corresponding to Figure 7.4. The gray surface corresponds to the outer boundary. The green surface is the DEJ. The red elliptic cylinder marks the lesion dimensions. A vertical line is drawn at the thickest point annotated with the thickness.

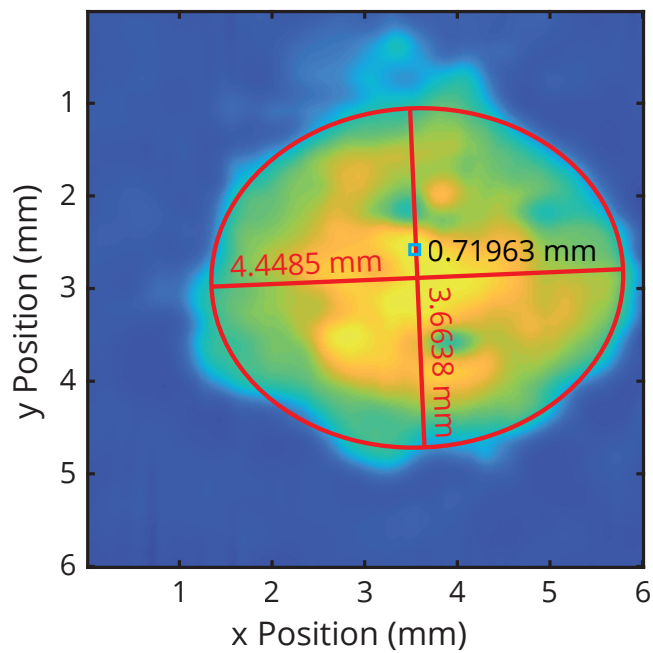


Figure 7.6: Thickness map of the lesion presented before. The red ellipse and its major axes indicate the lesion dimensions. The red annotations contain the sizes of the axes. The global maximum is marked by a cyan box annotated with the thickness value.

MATLAB returns an ellipse with two major axes corresponding to the lateral lesion dimensions (see red ellipse in Figure 7.6).

As summary, the whole process is depicted in a work-flow scheme in Figure 7.7. Additional code examples are presented in Appendix B.6.

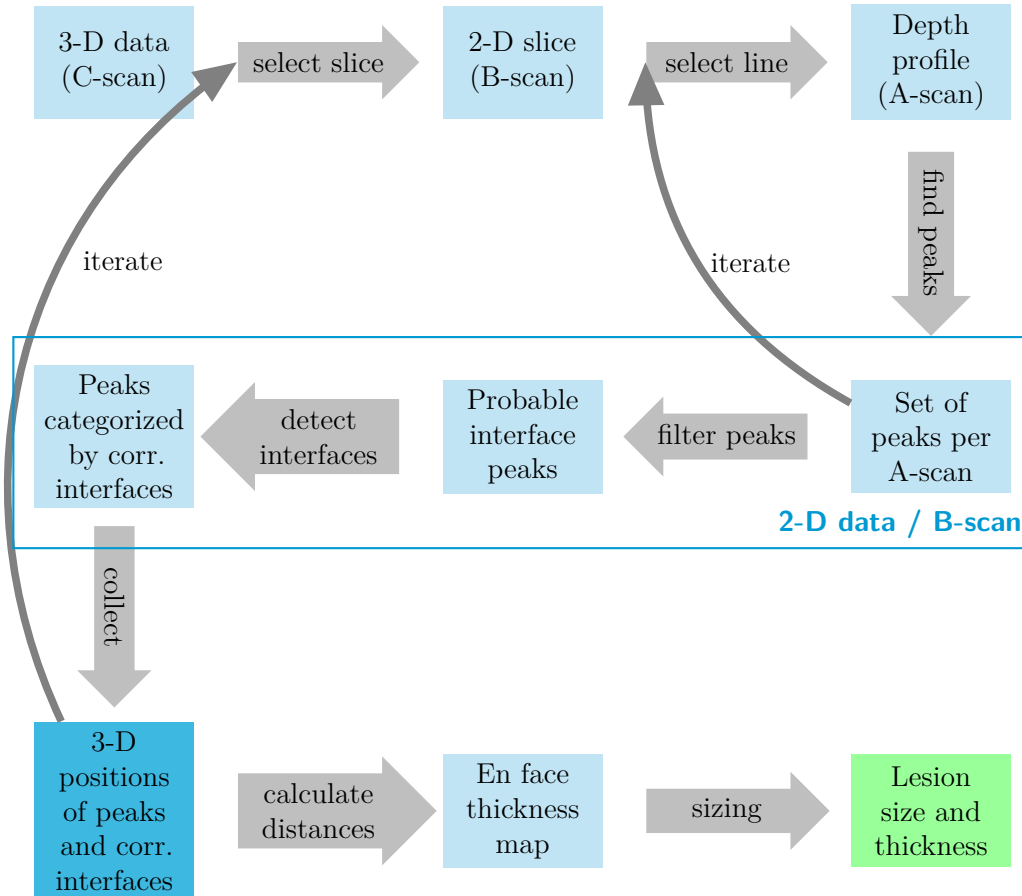


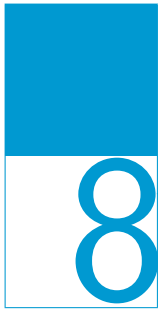
Figure 7.7: Work-flow scheme of the segmentation and thickness assessment algorithm.

The presented automated segmentation is capable of calculating the whole geometry of the lesion when applied on three-dimensional OCT data. With this tool the growth of a suspicious lesion can be tracked without surgical intervention. However, an evaluation of the data is only possible in post-processing so far, since, e.g. for the presented lesion, the processing time using the MATLAB script is 7 min to 10 min on a fast office machine (Intel® Core™ i5-4440 @ 3.10 GHz with 16 GB RAM). An implementation as a live volumetric image segmentation for *in vivo* OCT measurements would be even more convenient. With a patient database containing all tracked nevi the skin cancer screening could be highly improved, at least for lesions with a thickness < 1.5 mm.

This technique is also used in a multimodal context as presented in the next chapter.

“The science of today is the technology of tomorrow.”

— Edward Teller



Chapter 8

Multimodal approaches including optical coherence tomography

Optical coherence tomography has evolved to a powerful tool for medical applications. Yet, often there are insurmountable limits arising from physical properties of this measurement technique. E.g. the penetration depth of OCT is limited due to signal degradation (see Chapter 3). In other cases additional information is required or would be helpful to allow robust conclusions. In the project *MeDiOO*, where this work was performed, the goal was to build and evaluate multimodal approaches for the thickness assessment of lesions and, in particular, melanoma. The limited penetration depth was tried to be overcome by optoacoustics which potentially has much larger axial field of view at the cost of resolution. With (resonance) Raman spectroscopy a qualitative measurement instrument was added for the determination of chemical fingerprints to distinguish pathological markers.

In this chapter a brief overview of these approaches is presented with focus on the work within the project *MeDiOO*.

8.1 Optical coherence tomography with optoacoustics

The basic idea to combine the two modalities optical coherence tomography and optoacoustics is to achieve a penetration depth of up to several centimeters (OA) [85] and the high lateral and axial resolution of OCT for smaller depths (as shown in Chapter 6: ≤ 1.5 cm).

Another important point is that the two modalities have complementary contrast mechanisms. OCT detects changes in refractive indices and scattering on particles and interfaces, whereas optoacoustics relies on energy deposition by light absorption of the medium generating an acoustic signal. Both, scattering and absorption are

complementary as well as optical and acoustic signal propagation. This can be used to mutually correct the acquired data increasing the accuracy of the measurement.

8.1.1 Optoacoustics

Alexander Graham Bell has described the optoacoustic effect, also called photoacoustic effect, as phenomenon of light-matter interaction in 1880 [9]. Long time no attention was spent to possible applications of this effect. The invention of short pulse lasers gave raise to a wide range of new tools utilizing the optoacoustic effect. Concerning biomedical applications of OA Beard et al. give a comprehensive review, see [85].

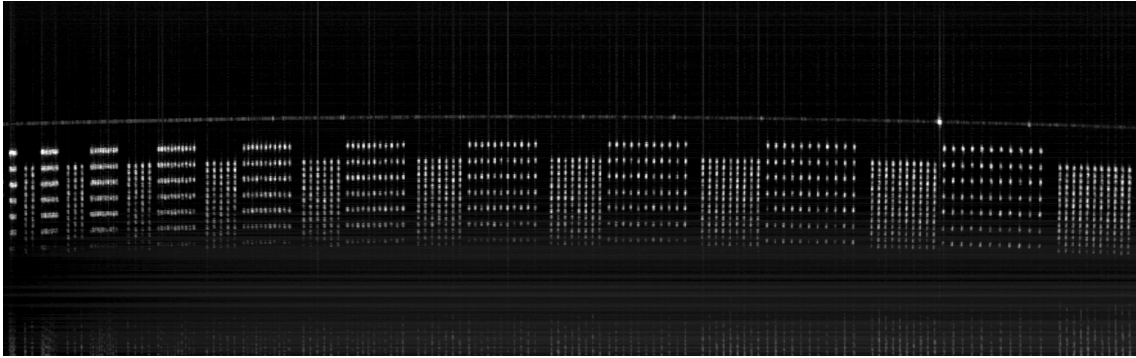
8.1.2 Preliminary multimodal OCT-optoacoustics measurements

Maintaining the compatibility of both modalities is crucial for combined applications. Therefore, preliminary investigations are required. As mentioned before, there are different approaches of combining OCT and OA.

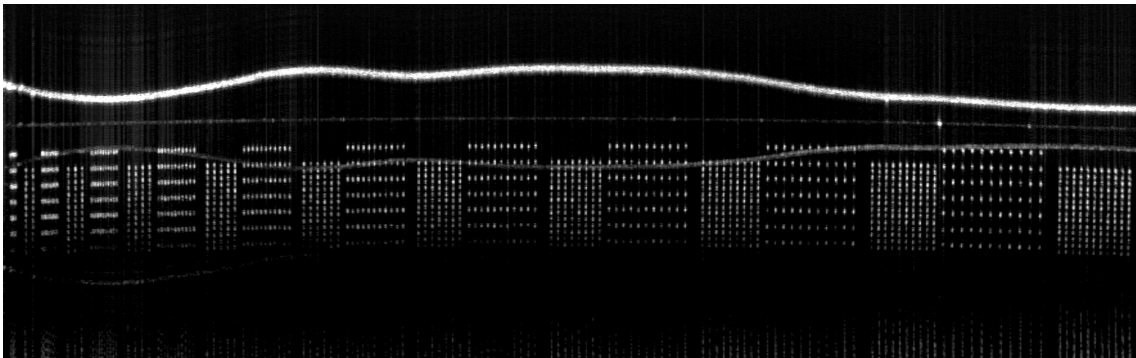
In addition to the techniques of photoacoustic tomography (PAT) and photoacoustic microscopy (PAM) presented in [85], another possible solution is to use an acoustic one dimensional sensor transparent for OCT, which was chosen in the context of *MeDiOO*. The piezoelectric polymer polyvinylidene fluoride (PVDF) acts as an ultrasound transducer where the signal is obtained by sputtered indium tin oxide (ITO) conductors and connected fast acquisition electronics. The details of this promising approach is beyond the scope of this work. Nonetheless, the compatibility of this particular technique to the present OCT system has to be considered, especially the optical draw-backs of the PVDF detector foil.

The impact of the optoacoustic foil on the OCT measurements was investigated by using the sensitivity pattern (S) of the calibration sample *APL-OP01 OCT Phantom* (Arden Photonics). The PVDF foil produces a strong OCT signal leading to an intensity decrease of 10 % reflected by the pattern (see Figure 8.1(b)). It also produces an artifact image due to the reflection on the phantom surface. However, the resolution and the contrast is conserved proving that simultaneous measurements with OA and OCT through the detector foil are feasible.

The design and construction of an OCT suited transparent OA detector system was performed within the project *MeDiOO* by Elias Blumenröther. It was found that the detector system based on a PVDF foil requires a backing layer for acoustic impedance matching. This layer is fixed on the back side of the detector foil and has to have a thickness larger than the depth to be measured. Without the backing layer the acoustic signal is reflected multiple times on the detector-air interface producing



(a) Sensitivity pattern without detector foil.



(b) Sensitivity pattern with detector foil on top.

Figure 8.1: Comparison of the sensitivity pattern with and without the optoacoustic detector foil on top of the phantom measured with OCT. The vertical lines crossing the uppermost interfaces originate from dust particles at the surface and interference effects due to signal intensity saturation. The vertical and horizontal lines at the bottom of the images are mirror artifacts due to reflection on the bottom interface (not on the image).

huge artifacts burying the real signal for defined PVA skin phantoms as well as for real human skin. A 3 mm thick acrylic glass plate was chosen as backing layer to improve the OA signal. This, however, reduces the contrast of OCT for simultaneous measurements due to reflection on the surface of the acrylic glass.

As an example Figure 8.2 shows a combined multimodal measurement of a PVA phantom with melanin as an absorber acquired simultaneously. The first slope of the first peak (top to bottom) of the optoacoustic signal (cyan) represents the beginning of the absorbing PVA layer. A much smaller second peak protruding to the right shows the end of the layer. The refractive index, and thus the thickness of the layer, can be determined as shown in Chapter 4.3. By stretching the acoustic signal to match the interfaces the speed of sound in this phantom can be calculated (here $\approx 1530 \text{ m s}^{-1}$). Vice versa it is also possible to calculate the refractive index with

known speed of sound.

However, optoacoustic measurements of real skin are much more complicated, especially in terms of thickness determination. In contrast to the PVA phantoms, for *in vivo* skin measurements no good trade-off was found such that the combined OCT-OA measurements had to be done successively.

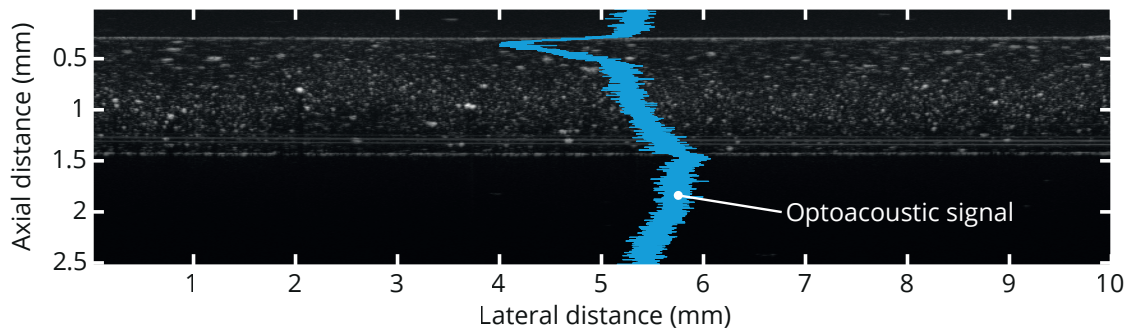


Figure 8.2: Example of a combined measurement with optoacoustics and OCT. The OCT depth is corrected by the refractive index of the PVA sample containing melanin as an absorber for optoacoustics.

8.2 Combined OCT-Raman and co-localized optoacoustic measurements

All standalone modalities have severe drawbacks with regard to reliable melanoma detection which is why they are not yet fully established in dermatology for this purpose. Currently it appears that one technique alone will not be able to reliably determine the surgical margins for a wide range of melanoma thicknesses non-invasively, and, therefore, a combination of such techniques is a more promising route to realize such a system in future. In some cases, co-localized measurements with a combination of OCT and Raman modalities have been applied for cancer diagnostics, [86–91] and have shown substantial increase in sensitivity and selectivity compared to both these modalities used separately [86].

This section presents the design and preliminary results of first clinical tests made with a combined skin cancer screening system, comprising Raman spectroscopy as a diagnostics modality as well as optoacoustics and optical coherence tomography as margin depth detection modalities [92]. While the Raman spectroscopic modality is integrated to the OCT measurement head, the OA detector system used follows the approach of a piezoelectric PVDF transducer but with transparent electrodes made of ITO [93], which are advantageous because of their high sensitivity and reliability. In the following, this chapter showcases measurements performed on human skin in preclinical studies on different skin lesions including melanocytic nevi.

8.2.1 Experimental setup

The schematic of the clinical setup for multimodal *in vivo* skin cancer screening is shown in Figure 8.3.

The Raman and OCT measurements were performed with a combined OCT-Raman probe, based on a scientific, cage mounted OCT measurement head (Thorlabs) as presented in Figure 8.4 (red frame). An optical arm for the detection of Raman signal was designed and built onto the OCT measurement head (Figure 8.4, green frame) for simultaneous skin measurement. Details on the performance of this setup part are described in Mazurenka et al. [94].

As OCT imaging device the same spectral domain OCT system was used as in Chapter 4 (Telesto-II, 1300 nm central wavelength, Thorlabs GmbH, Germany, equipped with a LSM-03 lens and an axial and lateral resolution of 5.5 μm and 13 μm in air, respectively). For the lesion depth determination presented below, the OCT B- and C-scans of the lesions marked for incision by the dermatologists were recorded. The acquired images have a size of 500 x 500 pixels in lateral x-y-direction with a pixel size of 20 μm and 1024 pixels in axial z-direction with a spacing of 3.54 μm (in air). This configuration requires storage space of approximately 1 GB per volumetric

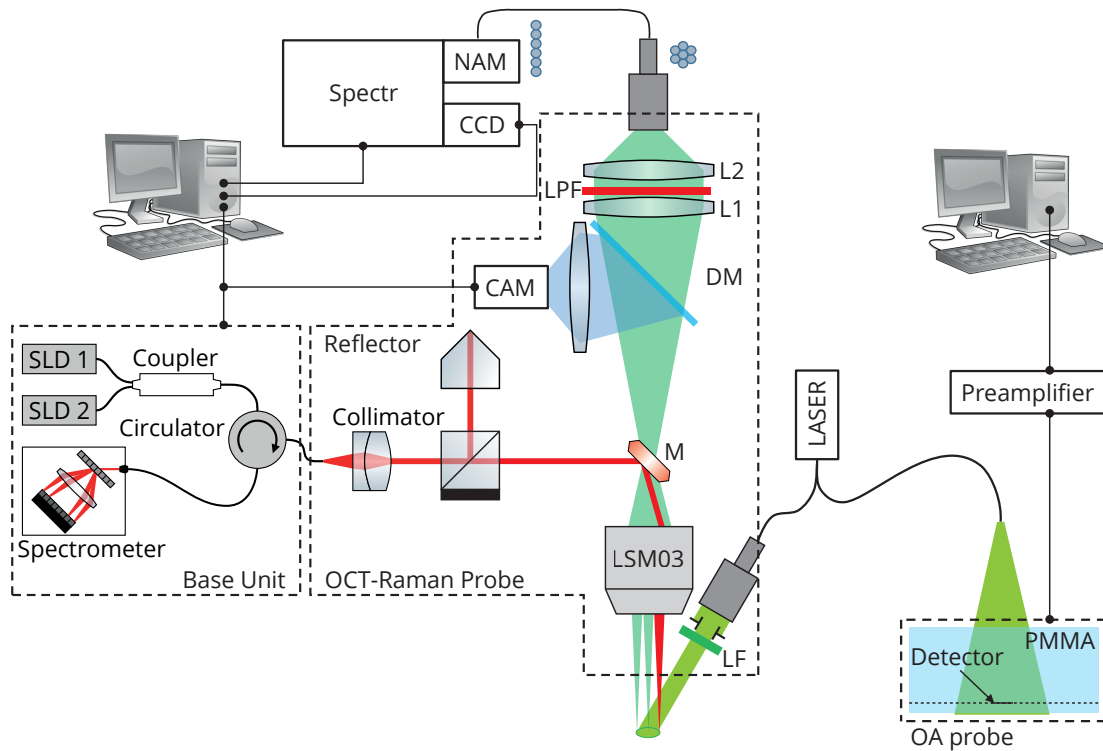


Figure 8.3: Experimental setup of the combined OA-OCT-Raman system. Laser line filter (LF), long-pass filter (LPF), lens(L), scanning mirrors (M), spectrometer (Spectr) [92].

image.

For the excitation of both, the Raman and the OA signal a pulsed laser (Ultra 50, Quantel, 532 nm, 7 ns pulse duration at 20 Hz repetition rate) was used as common light source. In case of the Raman modality the light was provided via a delivery fiber (Thorlabs, MPH910L02). After collimation, an elliptical beam spot of $9 \text{ mm} \times 7 \text{ mm}$ area was produced which nearly matches the field of view of the OCT scan lens ($10 \text{ mm} \times 10 \text{ mm}$). The laser beam was filtered from the luminescence and Raman signals generated in the delivery fiber using a 532 nm laser line filter (Thorlabs). With an iris, the laser spot area was reduced for the measurements on smaller lesions to minimize the contribution of the surrounding healthy skin to the Raman signal. The laser spot position and area were monitored and adjusted with the use of a removable CCD camera mounted on a separate socket on the OCT head. The camera detects the light of the white illumination LEDs, built into the OCT head, which is reflected from the skin and directed to the camera passing the dichroic mirror (DM, Figure 8.3).

For the Raman part, the backscattered light is likewise collected by the OCT

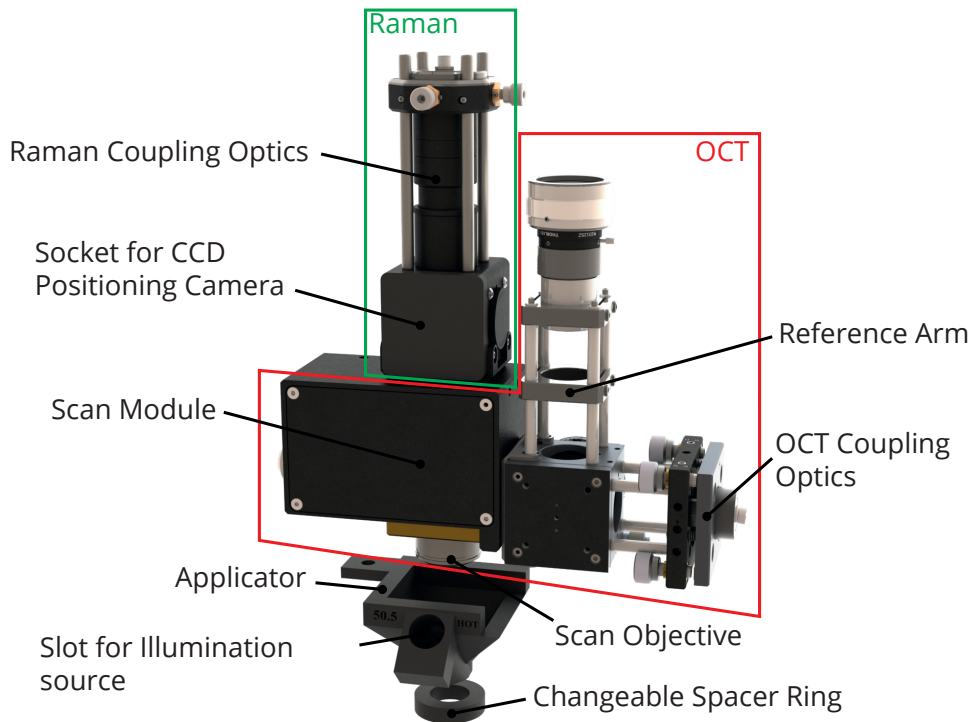


Figure 8.4: Rendered image of the combined OCT-Raman probe with an applicator and a spacer ring. The OCT part is framed red and the Raman part is highlighted with a green frame [92].

scanning lens and imaged onto a detection fiber bundle by two lenses. Their foci of 125 mm and 25.4 mm, respectively, are chosen to maximize the light coupling into the fiber bundle. Rayleigh scattered light is blocked by a long-pass filter (532 nm RazorEdge ultrastep long-pass Edge filter, Semrock Inc.) to avoid contamination of the signal by the intense Rayleigh peak (i.e. the elastic scattering). The coated galvanometric scanning mirrors of the OCT are transparent for visible light (95% transmission at 532 nm) and have maximum reflectivity around the working wavelength spectrum of the OCT at 1300 nm. One end of the custom-made detection fiber bundle (CeramOptec) consists of 18 linearly arranged fibers (each \varnothing 200 μm and $\text{NA} = 0.22$) designed to fit an NA matcher attached to a spectrometer (Shamrock SR-500i-D2, Andor) equipped with a CCD camera (Newton DU940P-BU, Andor). The other end is arranged into a circle with a diameter of 1.2 mm to fit the collection optics.

To prevent the room light from entering the Raman path and influencing the signal all arms and potential intrusion points were isolated with black tape (not shown in Figure 8.4). In addition, an adaptor, which also holds the Raman excitation

light optics, blocks the light from propagating to the environment when the head is applied on a lesion. The adaptor was printed with a 3-D printer (MakerBot Replicator 2X with Strong Black Premium ABS filament, 3Ddimensionals). The height of the adaptor was chosen to bring the skin surface to the working distance of the scan lens, primarily for the OCT measurements. The laser beam was aligned to the center of the field of view of the OCT lens. To ensure the detection of the Raman signal from the top of the lesion and the correct axial position of the lesion for the OCT imaging, a set of rubber ring spacers was also printed and applied (NinjaFlex filament, 3Ddimensionals). In total, 19 rings were produced with the height offset ranging from 0 mm to 7.6 mm with a step size of 400 μm . The rubber was chosen due to its mechanical flexibility which allows for better contact with the skin on parts of body with different topography, thus, preventing the room light from leaking into the detection arm of the Raman setup and improving the comfort for the patients during the measurements.

The OA detector (see Figure 8.5) consists of a 9 μm thick piezoelectric polyvinylidene fluoride (PVDF) film (Precision Acoustics, UK), with sputtered indium tin oxide (ITO) electrodes, forming a circular active area with a diameter of 1 mm. As backing layer, a 5 mm thick acryl glass, namely polymethyl methacrylate (PMMA), block is glued to the detector, also providing the thin film with the needed rigidity. To protect the film from mechanical forces during the measurements and to ensure a small but fixed distance to the sample, a front layer of 0.5 mm PMMA is applied. These elements (foil, electrodes and front/backing layers) are mostly transparent for wavelengths in the visible spectrum such that the excitation wavelength for the optoacoustic setup at 532 nm is sufficiently transmitted. The optical transmission of the PVDF film for 532 nm is 91.41 %. The circular detector part sputtered with ITO on both sides (ITO+PVDF+ITO) has a transmission of 72.18 %. For the PMMA support the transmittivity is similar to that of PVDF. For all parts the main loss occurs due to interface reflection. Considering the acoustic properties of the relevant detector area, no acoustic impedance mismatch of the ITO layer is expected. With a thickness of 50 nm the layer is much thinner than any relevant acoustic wavelength and can be considered as acoustically transparent.

The detector system is held by a self-designed, 3-D-printed frame which also holds the electrical preamplifier, as well as the illumination multimode fiber (WF 600/660N, CeramOptec). During the clinical measurements, the fiber facet was positioned 18 mm above the sample, yielding a spot diameter of 6 mm at the skin surface. For the illumination, the same laser source (Ultra 50, Quantel) as for the Raman measurements was used. The illumination was perpendicular to the detector plane and centered around the active detector area, as can be seen in Figure 8.3, OA probe (right part) and Figure 8.5.

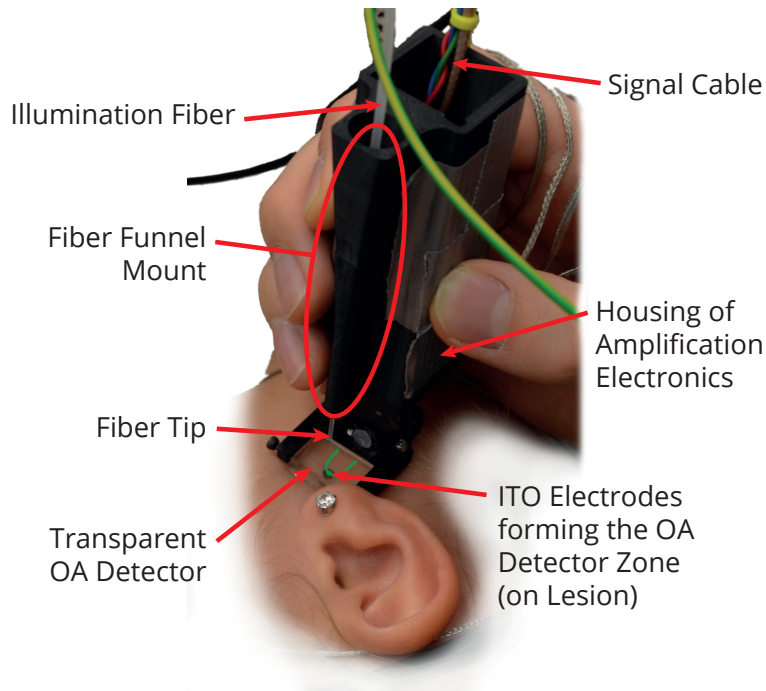


Figure 8.5: Photo of the OA handheld applicator on a nevus. The illumination fiber is aligned coaxially with the detection point. The ITO electrodes and the detector zone are highlighted in green [92].

8.2.2 Ethics and Maximum Permissible Exposure compliance

The performed measurements were approved by the Ethics Committee of the University Medical Center Göttingen (3/3/15) and the Ethics Committee of the University Medical Center Rostock (A 2016-0115) and met the principals of the Declaration of Helsinki.

In general, instruments used for *in vivo* measurements with direct illumination of the patient's skin by the laser light should comply with MPE requirements by means of exposure power and time, limiting the incident laser beam energy or power density, fluence and the accumulation time [94]. This is not relevant for the OCT system since the power of the scanning beam is far below MPE. The performance of the OCT part in the combined OCT-Raman probe was demonstrated earlier in Chapter 6 and the Raman instrument part was reviewed in [94]. Concerning OA, the acoustic signal intensity is proportional to the energy deposited through absorption of the excitation laser pulse, which is also limited in energy by MPE regulations. The ANSI standard Z136.1 [95] for skin exposure to a 10 ns pulsed laser with 532 nm is 0.02 J cm^{-2} per pulse. For a pulse train with $N = 2,000$ pulses the MPE pulse

energy is limited to:

$$\text{MPE}_{\text{train}} = \text{MPE}_{\text{single}} \times N^{-0.25} = 20\text{mJ cm}^{-2} \times 2000^{-0.25} \approx 2.99\text{ mJ cm}^{-2} \quad (8.1)$$

For Raman spectroscopy, the MPE limitations usually result in low Raman signal and particularly in a poor SNR. In this setup, higher Raman signals are achieved by the collection of the integrated signal from the full surface area of the lesion under investigation which is enabled by using the OCT scan lens for the Raman signal light collection. It is also important to characterize and optimize the Raman optical setup to minimize light losses within the instrument itself. The suitability of the OCT-Raman probe for efficient collection of the diffused light emitted by turbid media was shown in [94].

8.2.3 Measurement protocol

With all three modalities, the measurements were performed on 10 patients with human Caucasian skin. In total 13 lesions were examined with the combined OCT-Raman-OA system capable of simultaneous OCT-Raman measurements. However, for better monitoring and documentation of the measurement process, OCT and Raman measurements were obtained sequentially at this stage. Due to the separate OA applicator the laser source had to be switched to perform a subsequent OA measurement.

The protocol for the clinical measurements consists of the laser energy and spectrometer wavelength calibration, the Raman, OCT, and OA measurements on the lesions marked for excision, and post-measurement spectrometer wavelength calibration. The laser pulse energy is adjusted by changing a laser Q-switch delay and is set right below the MPE limit. During the clinical measurements, *in vivo* Raman spectra were recorded for 100 seconds corresponding to calculated values of MPE of 3 mJ cm^{-2} . This results in a maximal laser pulse energy of $\approx 1.48\text{ mJ}$ per pulse for the illuminated area of elliptic shape with axes of 9 mm and 7 mm, respectively.

The calibration of the spectrometer was performed by a linear fit of the recorded positions of seven prominent aspirin (Bayer) Raman lines within a Raman window of 800 cm^{-1} to 1800 cm^{-1} to the positions given by literature [96]. The Raman setup response function was also recorded by placing a diffuser (Thorlabs) as a measurement object in front of the combined OCT-Raman setup, thus, providing a measure of the luminescence and Raman signals generated by scattered incident laser light in the Raman setup optics.

For the measurements on subjects, the OCT-Raman head was positioned on the top of a lesion in such a way that the lesion was in the center of the field of view of the OCT lens. The positioning was performed by observing the lesion via both camera and three-dimensional OCT preview scans. Depending on the skin and lesion

thickness, skin elasticity, and the exact body area under study, a different amount of skin is covered by the adapter aperture moving the lesion top away from the work distance of the OCT lens. The distance between the top of a lesion and the OCT lens was corrected by means of suitably arranged rubber spacers (see Figure 8.4). Additionally, these spacers maintained the fixation of skin relatively to the applicator to avoid motion artifacts for OCT and Raman measurements. They also served as a mount for a black blanket which in some cases was needed to minimize the influence of ambient light. When the alignment was optimal, a B-scan was recorded with 48 kHz A-scan rate averaging over 20 scans per final A-scan with a total number of 1000 A-scans per B-scan resulting in an acquisition time of < 0.5 s. It was followed by a C-scan consisting of 1000×1000 A-scans but without A-scan averaging, thus, taking approximately 30 seconds.

After the OCT measurements, the combined head remained on the nevus for the Raman measurement. The iris diameter of the illumination optics of the Raman setup and hence the laser spot diameter was then adjusted to mainly illuminate the lesion and not the surrounding healthy tissue. Subsequently, a measurement for an accumulation time of 100 s took place. The combined head was not moved during the whole measurement procedure. To find differences between healthy skin and the lesion, a reference measurement on a healthy skin part of each patient was performed. Due to the fact, that the Raman spectrum of skin at different body parts is different, the reference measurement was done next to the lesion and not more than 2 cm apart. For the reference measurement, the iris diameter and accumulation time remained the same. If the patient had more than one nevus classified suspicious the OCT and Raman measurements were repeated for every nevus as described above.

After Raman measurements, the OCT-Raman measurement head was replaced by the OA head. A strong electromagnetic noise pickup was produced by the laser source and received by the sensitive OA transducer foil. To avoid this kind of distortion the patients as well as the measurement operator had to be grounded properly by a cable connected to the building ground level. Depending on the location of the lesion on the body this was achieved by winding the grounding wire around the patient and the operator or by building a flexible cuff made of aluminum foil, thus, increasing the contact area and the grounding effect. In case of homogeneous lesions, the detector was centered on the lesion, whereas for inhomogeneous pigmented lesions different distinct measurement spots were selected. The OA measurement was performed in a single laser pulse shot with a pulse energy of 1 mJ illuminating an area of minimum 27 mm^2 . Thus, the energy exposure remained far below the MPE with 5.4 mJ per pulse or 3 mJ pulse energy for a pulse train of 10 pulses on the illuminated area. As for comparison and increase of statistics, 5-10 measurements were performed in quick succession (≈ 1 s per shot) at the same position, which, however, are not part of the presented data here.

Similar to the Raman measurements, data of regular skin tissue located in the

vicinity (< 2 cm) of the lesion was acquired as reference.

8.3 Data processing

8.3.1 OCT

Before lesion depth assessment, recorded OCT image depths were corrected for the mean refractive index of skin, $n = 1.36$ for $\lambda = 1300$ nm [75]. Due to unknown real feature geometries, a separate refractive index determination as for example in [97] was not feasible. Further corrections i.e. for geometry [98] were not needed, since the skin is deformed anyway during measurement and only the thickness of the epidermis is required. OCT data were processed and evaluated in two ways: The first approach was to enhance the contrast of cross-sectional B-scan images for better determination of the lesion margin depth by manually setting markers by eye as described in Chapter 6. First, the contrast was enhanced by means of contrast limited adaptive histogram equalization (CLAHE) [99]. Then the rotating kernel transform [74] with a kernel size of 7 pixels was applied to the contrast enhanced images. The last steps were the individual thresholding by setting the minimal and maximal values for the gray scale and reducing the pixel noise using a 2-D Gaussian filter ($\sigma = 1$). Image processing was performed in a custom written MATLAB application also determining the lesion thickness from the manually set markers.

The second approach is a fully automated thickness assessment based on two- and three-dimensional image segmentation. There, the upper horny skin layer (stratum corneum) and lower boundaries of the epidermis (DEJ) are detected by a custom classification algorithm inspired by Koozekanani et al. [84]. On each A-scan peak detection is applied producing a set of points with a high probability to belong to a boundary. The total amount of sets of the whole volumetric data is then refined slice by slice (B-scan) extracting the boundary surfaces (see Chapter 7.2). As an example, Figure 8.6(a) shows an enhanced cross-sectional image as described previously, and the automatically detected boundaries (green and red line). The boundary detection itself does not require the image enhancement, which is here applied as guide to the eye. Using the algorithm on all slices in both lateral dimensions and averaging the results 3-D surfaces are calculated not only representing the boundary geometrics but also the volumetric dimensions of the lesion (see Figure 8.6(b)). From this, a thickness map is calculated where the maximal thickness of the lesion can easily be assessed by means of size and lateral position (see Figure 8.6(c)). A thorough description of the algorithm was presented in Chapter 7.

Both methods have the natural drawback of needing a DEJ interface to work properly. This is limited by the penetration depth of the OCT and the morphology of the lesion.

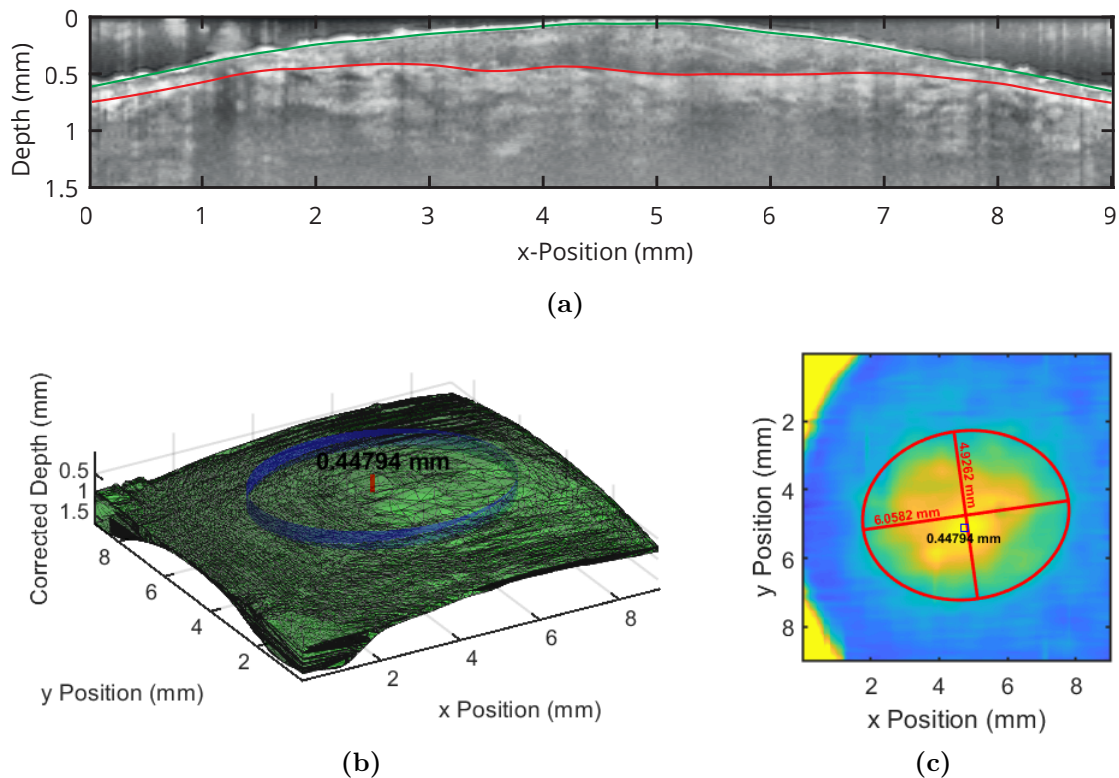


Figure 8.6: a) Cross-sectional image of a processed melanoma. The contrast is enhanced as guide to the eye. The green line shows the upper skin layer (stratum corneum), whereas the red line denotes the detected DEJ. b) The green volume represents the segmented lesion, similar to a) (region between green and red line) but in three dimensions. c) Thickness map of the lesion. The maximum is marked by a black square. The blue ellipse in b) corresponds to the red ellipse in c) [92].

8.3.2 Optoacoustics

The recorded OA signal is connected to the time evolution of the ultrasonic pressure waves detected by the transducer. Due to the finite absorption of the detector and the induced thermal voltage a pyroelectric signal is produced which overlays the OA signal [100–102].

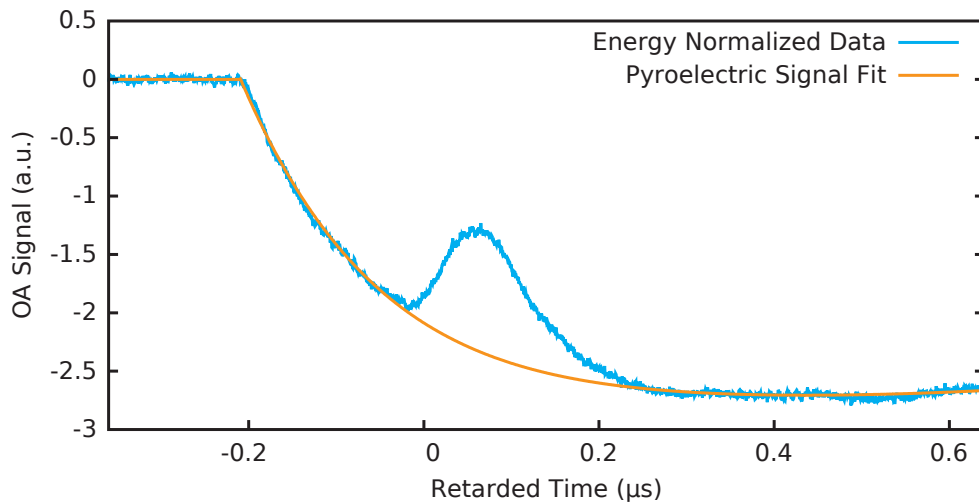
Due to the longer time scale and characteristic exponential decay of this thermal effect compared to OA pressure waves the pyroelectric signal can be fitted by an exponential curve and removed from the measured signal (see Figure 8.7(a)). A reliable benchmark for the successful removal of the pyroelectric signal is to check whether the total signal recorded reaches the zero level outside the OA signal region (Figure 8.7(b)). This is motivated by the fact that after the OA ultrasound waves have passed the front layer and detector layer and have propagated into the backing

layer, they can be considered as vanished such that no additional OA signals should be detected in the above time windows. In addition to the pyroelectric signal the instrument response function affects the measurements. To mitigate its effect, the instrument response function is measured by using black tape faced to a glass substrate as sample and deconvolved from the skin measurements (see Figure 8.7(b)) [49]. However, in general, the deconvolution amplifies parasitic signals, often making the resulting curve unusable. This can be avoided by removing acoustic frequencies above 20 MHz, where the parasitic signals mainly reside, producing a suitable signal, although, with reduced bandwidth. An extensive description of the theory of inverse signal reconstruction is presented by Stritzel et al. in [103]. Details of the OA detector system and OA signal processing are outside the scope of this work.

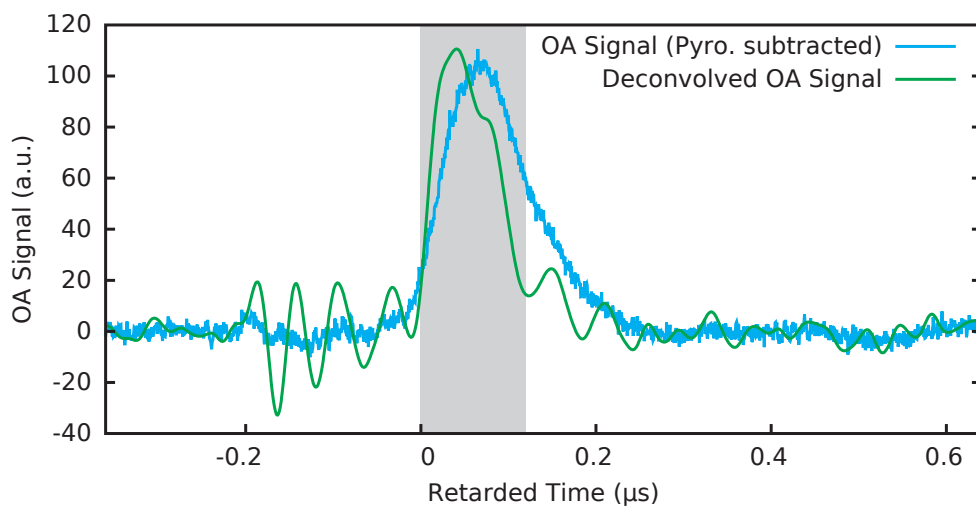
8.3.3 Raman

Raman spectra were accumulated over 100 seconds which corresponds to 2000 pulses. The intensity is initially indicated by counts on the CCD sensor. Figure 8.8 shows a recorded spectrum as a representative example. The spectra are contaminated by the strong photoluminescence background as can be seen in the raw signal (Figure 8.8(a), blue curve). To remove the luminescence background an Improved Modified Multi-Polynomial Fitting (I-Mod-Poly) [104] method was used. In Figure 8.8(a) the background fit is shown as red line, and was performed by using a polynomial parameter of 9. After baseline subtraction, the skin Raman spectrum is obtained, showing an unusual modulation due to an etalon effect, as shown in Figure 8.8(b), probably originating from the back-illuminated CCD chip of the Andor camera or the Rayleigh filter built in the spectrometer. This effect predominantly appears for weak Raman signals (low SNR) and a large fluorescence background. This contribution can easily be removed via FFT-notch filtering which is possible without taking more advanced instrument transfer functions into account. The resultant *in vivo* spectra, as shown in Figure 8.8(c), are very similar to the *in vitro* skin Raman spectra reported previously [105], although, as expected, with lower SNR. Spectral lines, i.e. the resonant carotenoid lines (orange) and some skin lines (gray), were assigned according to [106]. Slight shifts of the wavenumber were corrected with a well-known aspirin spectrum, taken on each measurement day.

A Savitzky-Golay (S-G) filter [107] with a polynomial degree of 2 was applied to further increase the SNR and the smoothness of the data. For the presented graphs in Figures 8.8(c) and 8.10 the chosen smooth window size was 30 data points. The spectra were normalized to the peak at 1800 cm^{-1} . Figures 8.7, 8.9 and 8.10 were obtained from the same lesion: a thin benign melanocytic junction nevus located at the left forearm of the patient, see Figure 8.9.



(a)



(b)

Figure 8.7: a) Plot of the acquired, energy normalized OA signal (blue) from a lesion and the according fit for the pyroelectric contribution (Pyro, orange), b) OA signal after subtraction of pyroelectric contribution (cyan) and the deconvolved, Fourier filtered signal (green). The histopathologic lesion thickness (gray frame) corresponds well to the distance of the main slopes of the deconvolved OA signal. This OA measurement corresponds to the lesion presented in Figure 8.9. The corresponding data was produced by Elias Blumenröther [92].

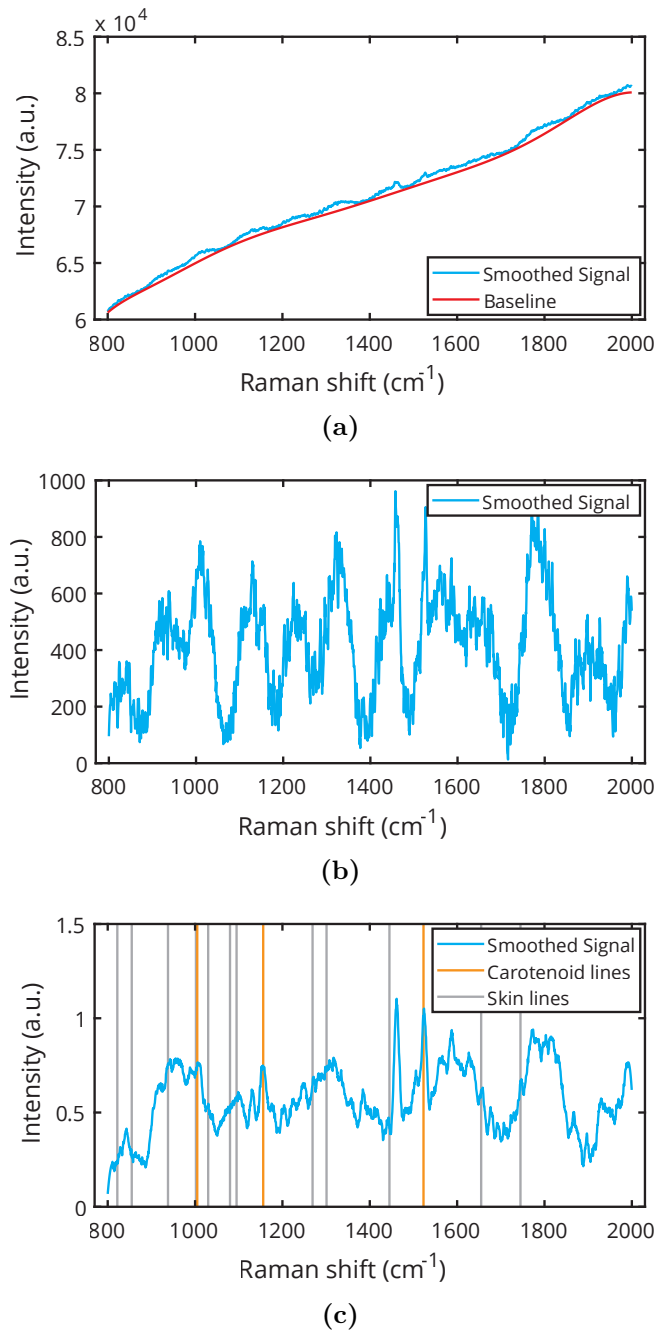


Figure 8.8: a) Acquired Raman spectrum (cyan) from a skin lesion. The intensity is represented by CCD camera counts. The baseline (red) is a polynomial fit of 9th order. b) After baseline correction and smoothing, the signal shows a periodic modulation distorting the Raman signal. This is probably from an etalon effect of the back illuminated CCD sensor or the Rayleigh filter. This effect can be removed by an FFT notch filter rendering the skin Raman lines visible. c) The resulting data shows a representative Raman spectrum with distinct peaks, notably the resonant carotenoid peaks (orange) [92].

8.4 Results and discussion

8.4.1 OCT

Figure 8.9(a) shows a typical image of a suspicious lesion obtained with the combined OCT-Raman setup. This image was processed with the previously mentioned manual thickness assessment including image enhancement. As can be seen, the obtained OCT thickness of 0.18 mm corresponds to the thickness assessed via histopathology of 0.179 mm (see Figure 8.9(c)). In this case it is a very thin lesion suited for a co-allocated OCT-OA measurement (see Figure 8.9(b)). The thickness of such thin lesions is often overestimated by the automated thickness assessment, since the difference between the epidermal layer thickness of normal skin and melanocytic lesion can be very small. Then the algorithm chooses the thickest part of the epidermis which is not necessarily part of the lesion. The automatically calculated thickness of the thin lesion underlying Figures 8.7, 8.9 and 8.10 is 0.21 mm. For better presentation of the automated assessment, a thicker lesion was chosen, as shown in Figure 8.6. A more detailed description of the OCT modality and its suitability for thickness detection of skin lesions including melanocytic lesions in comparison with high frequency ultrasound HFUS was reported in Chapter 6.

8.4.2 Optoacoustics

In this section OA measurement obtained with the single transparent detector of a benign lesion located on the lower arm of a patient are discussed. Even though the extremities are relatively easy to ground, significantly large parasitic signals are picked up by the detector as can be seen in Figure 8.7 for the time window from $-0.2 \mu\text{s}$ to $0 \mu\text{s}$ corresponding to the time after the trigger but before the arrival of the leading OA signal flank. Analyzing the pre-trigger time $< -0.2 \mu\text{s}$ reveals that the source for the unwanted oscillations originates from the laser. The influence of the pickup increases after deconvolution, especially close to the cutoff frequency of 20 MHz. Assuming a homogeneous absorber, the OA signal would follow a Beer-Lambert curve. Due to the limited frequencies, however, the rising slope of the OA signal is smoothed out. The shape of the exponential Beer-Lambert decay is altered by both the Gibbs phenomenon, which describes the oscillations produced by Fourier transformation of discontinuities [108], and by remaining oscillations from parasitic signals. However, around the retarded time of $0.1 \mu\text{s}$ a clear drop is observable corresponding to a strong decrease of absorption (see Figure 8.7(b)). Biological tissue in general is not homogeneous which is also obvious from the histology for the case of the presented lesion in Figure 8.9(c). As a non-focusing OA detector is used, the signal is integrated over a certain region of absorption. A decrease of the

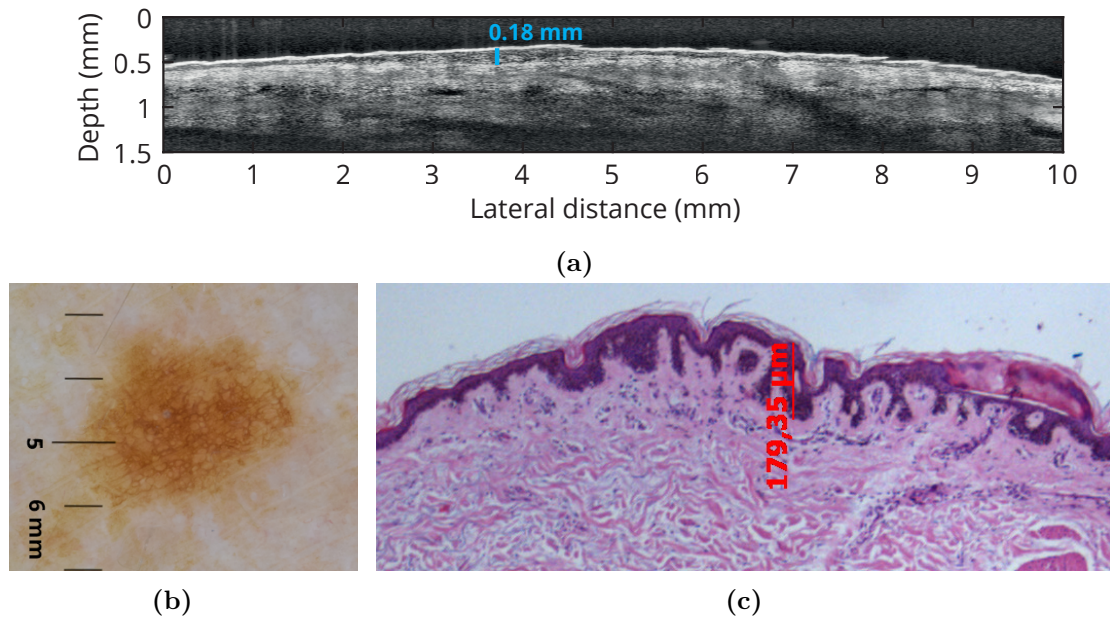


Figure 8.9: a) Enhanced OCT image of a thin lesion (benign melanocytic junction nevus) with manual thickness assessment of 0.18 mm. b) Dermatoscopic image (left, 1 mm per line distance). c) Histopathology with an assessed lesion thickness of 0.179 mm. The lesion corresponds to the lesion obtained with OA in Figure 8.7 [92].

OA pressure exceeding the Beer-Lambert law results from a decreasing absorption. In Figure 8.7(b) the lesion thickness obtained through histology is indicated by a gray frame, assuming a sound velocity of 1500 m s^{-1} . In comparison, the thickness is matching the area between the large slopes well. A crucial point is the definition of the thickness in the OA signal. While the rising slope (left boundary of the frame) is unambiguous, the falling slope (right boundary of the frame) is harder to determine. After deconvolution with the device transfer function the main contribution of the absorptive layer, i.e. the skin lesion, becomes visible. Due to the strong light absorption of the melanocytic tissue at 532 nm the penetration depth is limited, such that only thin lesions ($< 200 \text{ }\mu\text{m}$), could be evaluated by means of a reliable detection of the lower dermo-epidermal boundary. In addition, the non-melanocytic tissue also yields finite absorption producing an OA signal and impairing the contrast, i.e. signal amplitude, at the interface of the melanocytic lesion and the non-melanocytic normal skin tissue. These drawbacks can be circumvented by using larger wavelengths which is planned for future versions of the system.

For the presented example, a good result is obtained by measuring the distance between the rising slope and the end of the falling slope of the deconvolved OA signal (Figure 8.7(b), green curve).

8.4.3 Raman

In vivo Raman measurements on human skin are very challenging due to low Raman scattering cross sections, especially complying with the MPE levels. Nonetheless, the measurements in this study show significant changes in the Raman signal between lesion and normal skin as reference. Exemplarily, in Figure 8.10 such a measurement is shown. The cyan curve represents the lesion and the red curve is a reference measurement on nearby normal skin. Three Raman lines from carotenoids are clearly visible in the spectra which are resonant for 532 nm (orange lines). The right peak ($\approx 1520 \text{ cm}^{-1}$) is overlapping with a peak of the room illumination lamp, which also produces a peak at $\approx 1480 \text{ cm}^{-1}$. Light contamination from the environment could not be completely avoided but was minimized as much as possible, depending on the location of the lesion. For the example shown, as well as for many other lesions, the carotenoid signals increased compared to the reference measurements on the close normal skin areas. The other skin lines stemming from proteins and lipids (gray lines) cannot reliably be detected at this point, due to the low SNR in the current version of the system. However, noticeable changes in the regions 1200 cm^{-1} to 1400 cm^{-1} and 1530 cm^{-1} to 1630 cm^{-1} were observed for different lesions including melanomas. Still not quantifiable, this is a hint for systematic changes of the skin structure which is to be confirmed in future studies with more statistics. On the other hand, differences between different body parts were much larger than differences between lesions and normal skin areas, making it hard to extract reliable information or to distinguish lesion types by Raman signature in general. With a larger set of Raman spectra, it is feasible to investigate regularities of the signatures, e.g. via machine learning algorithms like principal component analysis. Being a proof-of-principle, these preliminary results facilitate further studies with more Raman measurements which are proposed for future work.

8.4.4 General

The laser source for Raman and OA was chosen as a compromise on versatility, price and compactness, and the fact of being resonant (and, thus, providing a reasonable SNR) at least for the carotenoid Raman signal. Since the MPE levels are a limiting factor and the Raman cross-section is proportional to $1/\lambda^4$, a wavelength of 532 nm is a reasonable choice. In addition, for the OA measurements it was aimed at stronger tissue absorption, and thus a larger acoustic signal, which is given for 532 nm. For a future system for this application, a wavelength of 660 nm is probably more suited as a compromise between OA and Raman requirements (see Tfaili et al. [106]).

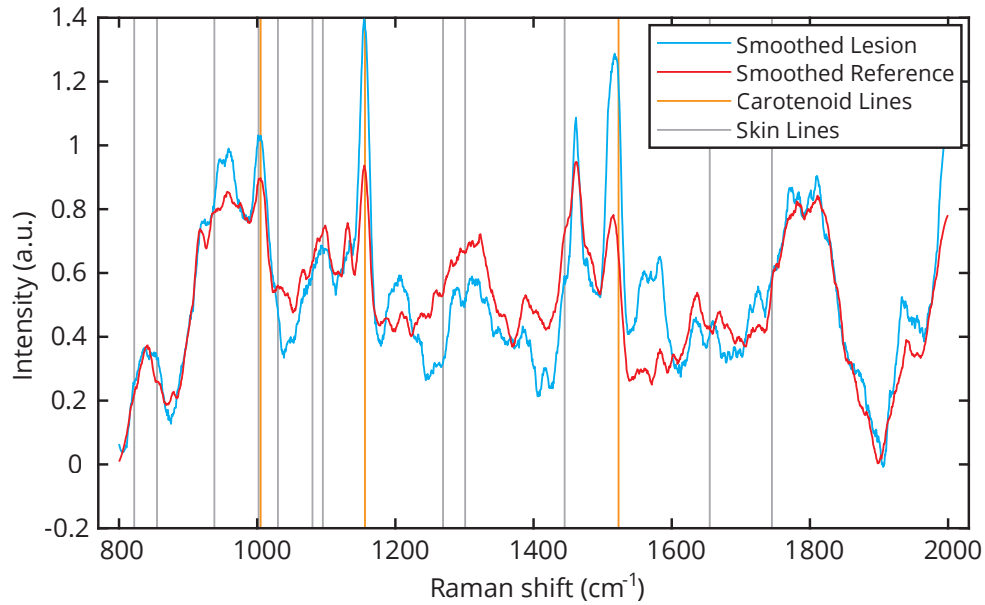


Figure 8.10: Smoothed spectra of a melanocytic lesion (cyan) and of normal skin from the same patient as reference (red). The spectra are normalized to the band at 1800 cm^{-1} . Typical skin lines are represented by gray vertical lines and the resonant carotenoids by orange vertical lines. The lesion corresponds to Figure 8.7 and 8.9 [92].

8.5 Conclusions

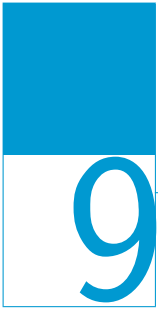
A trimodal system intended for skin cancer detection which consists of a combined OCT-Raman modality and an optoacoustics modality was presented. The Raman excitation and detection were incorporated in the OCT measurement head such that the OCT functionality is not affected. In addition, a transparent OA probe was designed to include a third modality based on optical contrast and acoustic signal propagation, potentially increasing the field of view for thickness determination of the lesion as well as the accessible lesion depth. For Raman and OA, the MPE compliance is ensured by the correct choice of the pulse energy provided by the illumination laser light source whereas the OCT modality is intrinsically below MPE levels.

In a proof of principle, it was demonstrated that the OA modality based on a transparent PVDF detector can be used for lesion thickness detection. In the current setup, the penetration depth and thus the maximal measurable thickness is limited by the laser wavelength of 532 nm due to absorption. An acrylic glass backing layer serves as mechanical support for the OA detector and increases the measurable thickness by avoiding acoustic reflection artifacts. In turn, however, it reduces the OCT contrast such that simultaneous measurements in a single device head are

not feasible with the current setup. Instead co-localized sequential measurements with OA and the combined OCT-Raman were conducted in this work. First *in vivo* measurements with the Raman modality show good performance and acceptable SNR that allows for detection of resonant carotenoid lines and characteristic skin Raman bands. After baseline correction and adequate signal filtering, the comparison of lesions with normal skin shows variations of the spectrum in distinct regions which is most likely due to the structural anomalies in the skin, i.e. the lesion morphology and cellular structure. The three modalities were combined for the first time to our knowledge to perform simultaneous (OCT, Raman) and co-localized (OA) measurements on skin lesions including malignant melanoma in preclinical trials. Data sets of three-dimensional lesion geometry were obtained using the OCT modality, in future potentially also morphological information, thickness determination based on the OA modality, and the chemical fingerprint, i.e. pathophysiological parameters by using the Raman modality. Further improvements have to account for a different OA and Raman laser wavelength, e.g. at around 660 nm, thus, increasing the OA penetration depth and the Raman scattering efficiency (the latter with respect to the fluorescent background), as well as for the enhancement of the Raman SNR by optimizing the light transport and collection optics. Following that, the system appears suited as a future medical tool to improve skin cancer screening and early diagnosis, in particular, as all measurements were performed below the admitted MPE levels.

“The saddest aspect of life right now is that science gathers knowledge faster than society gathers wisdom.”

— Isaac Asimov



Chapter 9

Conclusions and outlook

This dissertation investigates OCT on human skin, and particularly on melanocytic lesions, facilitating access to the basics and advanced knowledge centered on OCT. It was conducted as part of the project *MeDiOO* with its interdisciplinary and multimodal approach for clinical relevant thickness determination of melanomas utilizing optoacoustics and OCT, and additional capabilities for lesion classification with Raman spectroscopy. In the first place, the focus of the presented work was optical coherence tomography. Especially the role of OCT in the presented multimodal measurements was accentuated.

Since human skin is the main specimen which was investigated, not only the optical properties were discussed but also, inter alia, the physiology and the clinical relevance for presurgical thickness assessment (Chapter 2). This also gives the motivation for the project and this dissertation. The thickness estimation and screening of the evolution in depth opens up new horizons for preventive applications for skin cancer diagnostics, especially for, but not limited to, malignant melanomas.

Nowadays, OCT is a well-established technique in various application scenarios. In particular, the potential in biomedical applications is still not yet fully explored. New laser sources and other components allow for faster and more precise measurements and also the data processing became more and more important. This work is founded on a theoretical description of optical coherence tomography (OCT) on scattering media (Chapter 3) where the principles of signal generation for different OCT systems are presented. Preliminary measurements were made to investigate the capabilities and identify potential drawbacks (Chapter 4). Different phantoms with well-defined scattering properties were designed and measured to enable quantitative measurements with OCT. However, the ideal samples, starting with very simple designs and moving to more sophisticated ones, were still far behind the complexity of human skin by means of morphology and richness of detail.

The construction of a custom OCT setup was not necessary since for the acquisition of the OCT data a commercial device was used. Nonetheless, a deep understanding of the signal generation in scattering tissue was acquired including models for signal

degradation limiting the penetration depth. In particular, multiple and so called dependent scattering together lead to an additional dissipation of light and thus to a decrease of possible penetration depth or in-depth contrast (due to SNR), respectively. More and more models are emerging for the description of particular cases, but the field of scattering processes in highly turbid media still lacks for a unifying description of all occurring effects. A lightweight model was developed in the scope of this work to at least mimic the non-linear increase of scattering coefficients depending on the scatterer concentration of homogeneous samples (Chapter 5). This can be used to train an algorithm and to predict the scattering amount of known concentrations or to estimate the concentration for measured scattering coefficients.

The performance for skin measurements was examined and compared to other techniques as high frequency ultrasound and histopathology, the current gold standard (Chapter 6). The thickness assessment with standalone OCT already brought good results for lesion penetration depths up to 1.5 mm depending on the lesion type and morphology. In a certain region of thickness (below 0.8 mm) a good agreement between OCT and histopathology was reached. Notably, the relevant depth of 1 mm in most cases is detectable via the OCT system and data processing presented in this work. Lesions thicker than 1 mm are classified as high risk lesions recommended for immediate excision. However, larger penetration depths still demand for multimodal solutions with the additional benefit of data cross-validation as within the scope of projects like *MeDiOO*.

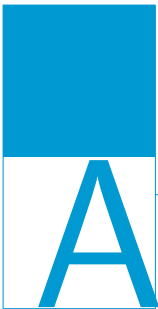
As successfully demonstrated here, the screening of melanomas is supported by cross-sectional OCT imaging. Even more promising is the three-dimensional imaging of the lesion showing the geometry of the epidermal layer, containing melanocytic tissue. The conducted measurements and the automated post-processing by means of segmentation (Chapter 7) are a proof of principal showcasing the options for further proceedings. For example, with fast scanning OCT system combined with improved in-time segmentation and a database would empower clinical operators to easily track the growth of a lesion in all directions without any surgical interventions.

Last but not least, the suitability of OCT as part of a clinical multimodal measurement system was investigated. As a result, OCT and Raman spectroscopy were successfully combined in one hand-held applicator capable of simultaneous OCT and Raman measurements (Chapter 8). The integration of optoacoustics failed due to the need of a backing layer on the transparent OA detector for acoustic signal clearing. This additional acrylic glass plate was responsible for a high loss of OCT signal reducing the SNR. However, co-localized measurements were conducted, demonstrating the integration of the data afterwards. *In vivo* Raman measurements are very challenging due to the small cross section of the Raman effect and the Maximum Permissible Exposure (MPE) limitations. In the community only few groups take MPE into account producing similar spectra with low SNR. With the presented setup, the measurements show hints for systematic changes of chemical

fingerprint due to different tissue types. But the changes between different body parts are even more significant. A larger, systematic study is required to clarify the correlations.

The main goal of the thesis, i.e. a reliable thickness determination of melanocytic lesions was achieved, as the full lesion geometry is extractable via an already well advanced algorithm as long as the lateral dimensions of the lesion are within the field of view and the thickness does not exceed the limit of 1.5 mm (Chapter 6 and 7). The second goal was the multimodal application of the OCT system in cooperation with the coworkers concerning optoacoustics and Raman spectroscopy. After evaluation of the suitability certain drawbacks with a combined OA system were found and simultaneous OA-OCT measurements are not possible so far. Instead, a co-localized approach was pursued. The integration of Raman spectroscopy was successful as a proof of principle, which still can be improved.

Based on the achieved results, the approach of this work has future potential to improve skin cancer screening providing additional lesion information, detect more melanomas at early stages and decrease the mortality due to skin cancer i.e. melanoma skin cancer. However, the findings of this dissertation need to be substantiated by further studies especially including a larger number of Raman spectra and e.g. different wavelengths for optoacoustics. Also other detection and geometry types of OA are possible as long as they are not interfering with other modalities. Especially the lesion characterization and classification with Raman spectroscopy demands for far more spectra to allow for data analysis and lesion type identification. A kind of Raman *in vivo* skin spectra database is recommended where data mining (e.g. via principal component analysis (PCA)) can give reliable results.



Appendix A

Device specifications

A.1 TELESTO-II - Spectral Domain OCT Imaging System

For all performed OCT measurements the commercial Spectral Domain OCT imaging system Telesto-II manufactured by Thorlabs GmbH, Germany was used. The following figures show the device and custom-made enhancements.

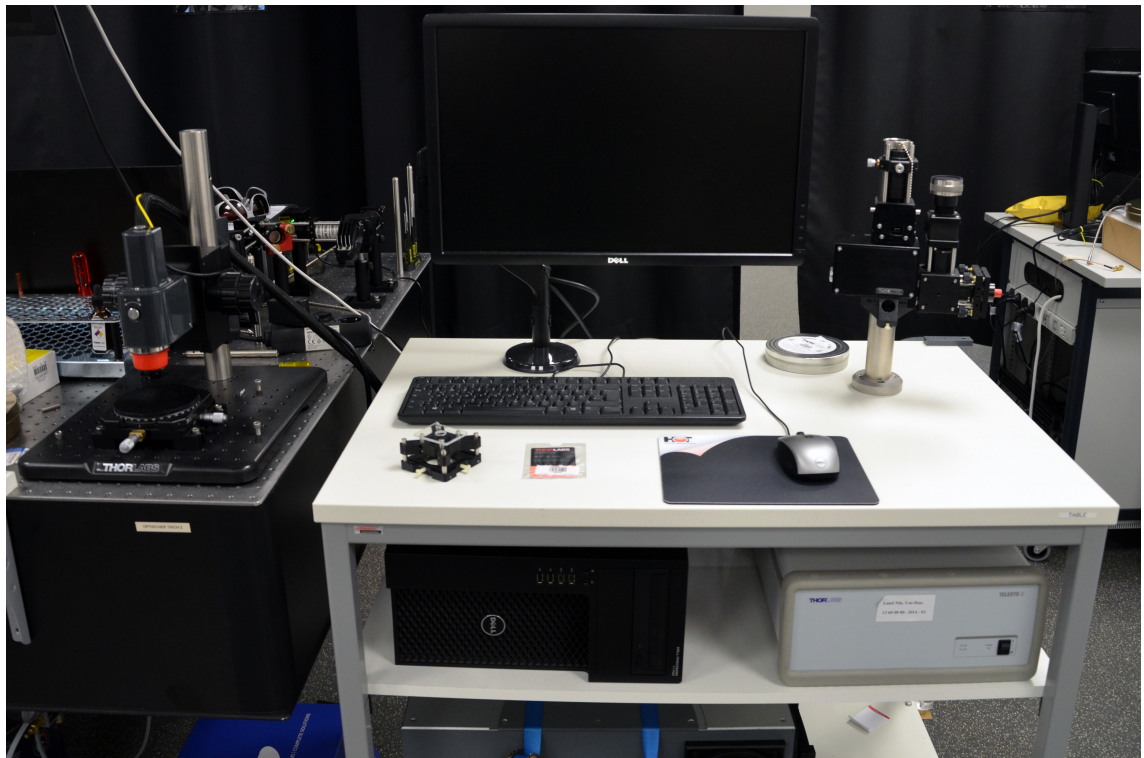


Figure A.1: Photo of the whole Thorlabs Telesto-II setup. The commercial probe (left) is attached on an optical table and the combined OCT-Raman probe (right) attached on the trolley. PC (black chassis) and spectrometer/source (light gray chassis) are placed on the second level below the table. The trolley with the equipment was also used as mobile setup in the clinical study.

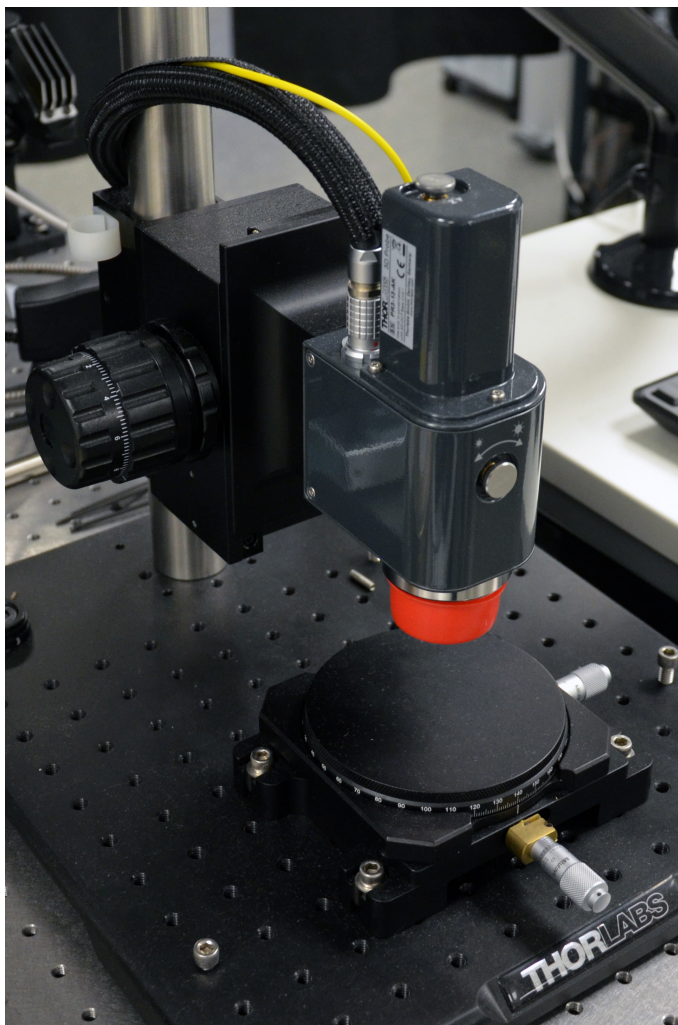


Figure A.2: Photo of the commercial Thorlabs probe. It was used for preliminary investigations.



Figure A.3: Applicator attachment to the commercial OCT probe. It was designed as a first attempt to fix the skin for OCT measurements. It was used during first clinical trials and the preclinical study in Chapter 6.

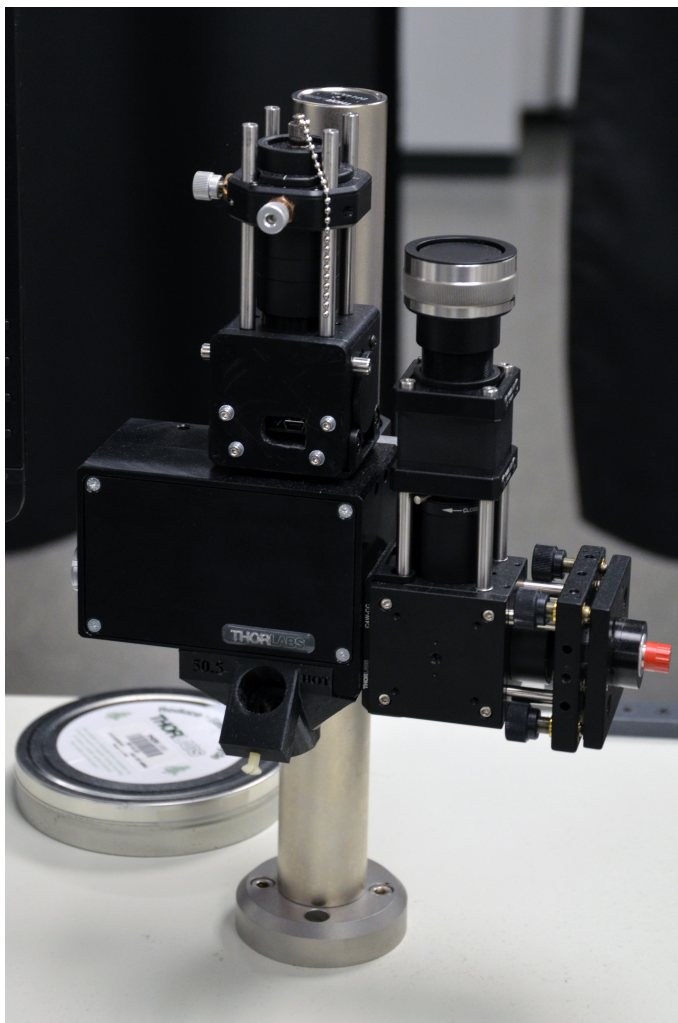


Figure A.4: Photo of the final modified scientific Thorlabs probe for simultaneous Raman and OCT measurements, denoted as OCT-Raman probe. It was used during the preclinical study in Chapter 6 and for the investigations in Chapter 8.

Table A.1: Optical performance specifications – TELESTO II. Source: Thorlabs

Specifications – TELESTO II	
Optical	
Central Wavelength	1.3 μm
Spectral Bandwidth	$\approx 100 \text{ nm}$
Axial Scan Rate	up to 76 kHz
Maximum Imaging Depth	3.5 mm
Axial Resolution Air/Water	5.5/4.2 μm
General	
Supply Voltage for base unit	100 V – 240 V / AC
Maximum Power Consumption	150 W
Weight base unit	12 kg
Weight Probe	1.5 kg
Storage/Operating Temperature	10 $^{\circ}\text{C}$ to 35 $^{\circ}\text{C}$
Dimensions of Probe Stand (L x W x H)	206 mm \times 305 mm \times 248 mm
Dimensions of base unit (L x W x H)	420 mm \times 320 mm \times 149 mm
Dimensions of Imaging Module (L x W x H)	60 mm \times 85 mm \times 187.8 mm
LSM03 - Scan Lens	
Effective Focal Length	36 mm
Lens Working Distance	25.1 mm
Maximum Field of View	9.4 \times 9.4 mm^2

A.2 GON360 - Instrument Systems

The goniometer GON360 manufactured by Instrument Systems, was used during the measurements of the anisotropy factor g and of the scattering properties of low scattering media in Chapter 5.

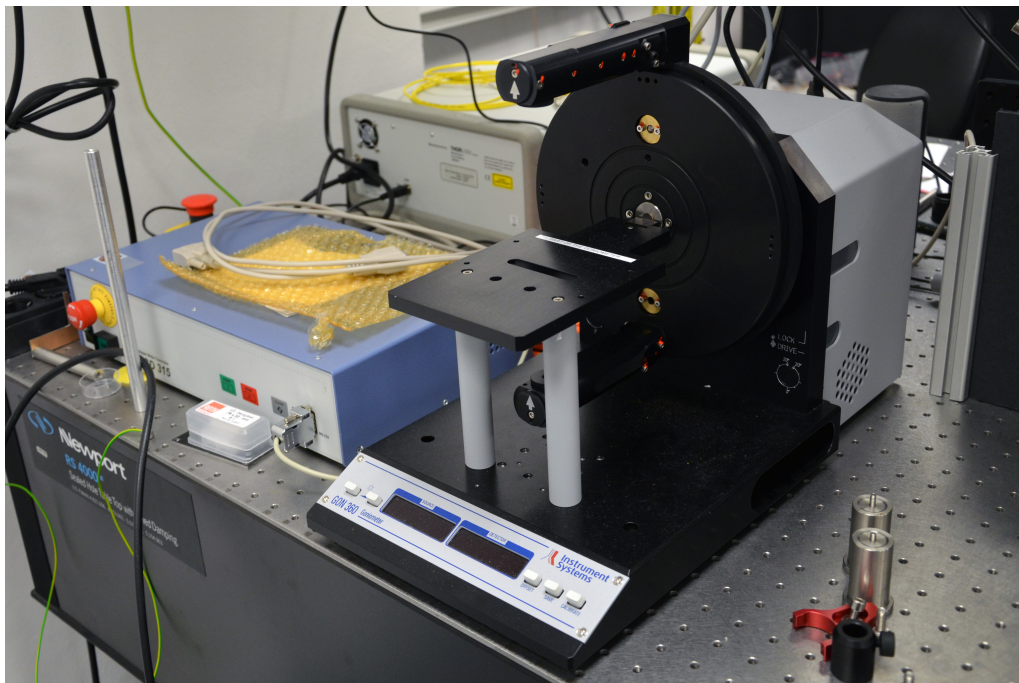


Figure A.5: Goniometer GON360 (Instrument Systems) was used to investigate the scattering profile of low scattering media.

Table A.2: Performance Specifications – GON360. Source: Instrument Systems

Specifications – GON360	
Optical	
Spectral Range	(190 nm to 2.3 μ m)
Measuring Spot	1 mm
Source	
Absolute Accuracy	better than $\pm 0.3^\circ$
Reproducibility	better than $\pm 0.05^\circ$
Adjustment Range	$360^\circ \pm 179.9^\circ$
Divergence of Illumination Beam	$\approx 4^\circ$
Detector	
Absolute Accuracy	better than $\pm 0.3^\circ$
Reproducibility	better than $\pm 0.05^\circ$
Adjustment Range	$360^\circ \pm 179.9^\circ$
for Reflection	from -7° to 187°
for Transmission	from 0° to 90°
Acceptance Angle	$\approx 4^\circ$



Appendix B

Layer segmentation

The source code of the performed automated layer segmentation presented in Chapter 7 and 8 is provided here.

B.1 EpiSeg_GetData.m

This file contains the code where the input data is read and the initial parameters are set. It calls functions delivered by Thorlabs (e.g. `OCTFileOpen` and `OCTFileGetIntensity`).

```

1 function [ OCT ] = EpiSeg_GetData( m_Path )
2 %EpiSeg_GetData Summary of this function goes here
3 %   Detailed explanation goes here
4 %
5 % Author: Arthur Varkentin, M.Sc., scientific staff member
6 % Leibniz Univerit"at Hannover, Hannover Centre for Optical
   Technology - HOT
7 % email address: arthur.varkentin@hot.uni-hannover.de
8 %
9 % Januar 2017; Last revision: 21-Juni-2017
10
11 %----- BEGIN CODE -----
12 % Add path to Thorlabs files
13 addpath('./OCT_Scripts');
14 addpath('./Functions');
15 % Make plots more beautiful
16 init_modplot;
17 % Create data container
18 OCT = struct;
19 % Measurement path

```

B Layer segmentation

```
20 OCT.m_path = m_Path;
21 % Get location of OCT measurement files
22 [OCT.filename, OCT.path] = uigetfile({'*.oct'}, 'Load OCT file.', OCT.
    m_path);
23
24 %%
25 % Prepare variables
26 OCT.origpath = OCT.path;           % store original OCT path
27 OCT.fileNR = length(OCT.filename); % get number of OCT files
28 OCT.Averaged_A = zeros(1024,OCT.fileNR);
29 OCT.IntensityScan = zeros(1024,OCT.fileNR);
30 OCT.IntensityScan_dB = zeros(1024,OCT.fileNR);
31 OCT.CorrectedScan = zeros(1024,OCT.fileNR);
32 OCT.CorrectedScan_dB = zeros(1024,OCT.fileNR);
33 %OCT.zAxisList = zeros(1024,OCT.fileNR);
34 OCT.legend_list = {};             % prepare legend
35 OCT.fname = {};
36
37 % Prepare z-Axis
38 OCT.zAxis=@(x)(3.62./1024.*x); % 3.62/1024 is the depth pixelsize
39 OCT.refIndList = zeros(length(OCT.filename),1);
40 OCT.refIndList(:) = 1.3222; % same refractive index for all datasets
41
42 %% Get data from file
43 handle = OCTFileOpen(OCT.filename,OCT.origpath); % read data from
    file
44
45 [OCT.pathstr,OCT.fname,OCT.ext] = fileparts(char(OCT.filename));
46 OCT.legend_list = OCT.fname;
47
48 %%%% read dataset properties %%%%
49 OCT.prop.SizeX = str2double(OCTFileGetProperty(handle, 'SizeX'));
50 OCT.prop.SizeY = str2double(OCTFileGetProperty(handle, 'SizeY'));
51 OCT.prop.SizeZ = str2double(OCTFileGetProperty(handle, 'SizeZ'));
52
53 OCT.prop.SpacingX = str2double(OCTFileGetProperty(handle, 'SpacingX')
    );
54 OCT.prop.SpacingY = str2double(OCTFileGetProperty(handle, 'SpacingY')
    );
55 OCT.prop.SpacingZ = str2double(OCTFileGetProperty(handle, 'SpacingZ')
    );
```

```

56
57 %%%% reading intensity %%%%
58 %Intensity = mat2gray(OCTFileGetIntensity(handle)); % load data to
    array
59 Intensity = OCTFileGetIntensity(handle);
60 % modify filename for storing data in struct
61 OCT.mod_fname = strrep(OCT.fname, '.', '_'); % for original data
62 OCT.mod_fname_edit = [OCT.mod_fname '_edit']; % for editet images (
    used filter)
63 OCT.mod_fname_pub = [OCT.mod_fname '_pub_ed'];% for publication
    quality images
64 % OCT.fig.title = strrep(OCT.mod_fname, '_', ' ');
65 OCT.ax_title = strrep(OCT.mod_fname, '_', '\_'); % do not interpret
    as subscript
66
67 %%%% close OCT file (deletes temporary files) %%%%
68 OCTFileClose(handle); % Close OCT file (deletes temporary files)
69
70 % axis definitions
71 xAxis = @(x)(OCT.prop.SpacingX .*x); % convert to mm
72 xAxisList = xAxis(1:OCT.prop.SizeX); % fill list of xAxis
    values
73
74 zAxis = @(z)(OCT.prop.SpacingZ .*z./OCT.refIndList); % rescale
    zAxis (depth)
75 zAxisList = zAxis(1:OCT.prop.SizeZ); % fill list of zAxis
    values
76 OCT.zAxisList = zAxisList;
77
78 % saving to OCT struct
79 OCT.data = Intensity;
80
81 OCT.fname = strrep(OCT.fname, '.', '_');
82 OCT.fname = OCT.fname;
83 % Thorlabs processed Data: I [dB] = 20*log10(abs(FFT(Spektrum [e-]))
    ).
84 % OCT.Averaged_A(:,i) = sum(Intensity,2)/size(Intensity, 2); %
    Average over B-Scan
85 % OCT.IntensityScan(:,i) = 10.^(OCT.Averaged_A(:,i)/20);
86 % OCT.IntensityScan_dB(:,i) = OCT.Averaged_A(:,i);
87 %

```

B Layer segmentation

```
88 %     OCT.AScans.(OCT.fname) = OCT.IntensityScan(:,i);
89 %     OCT.AScans_dB.(OCT.fname) = OCT.IntensityScan_dB(:,i);
90 %     OCT.BScans.(OCT.fname) = Intensity;
91
92 %OCT.zAxisList(:,i) = OCT.zAxis(1:1024)./OCT.refIndList;
93 end
94 %----- END OF CODE -----
```


B.2 LayerDetection2D.m

This routine detects the 2-dimensional boundaries of skin surface and dermoepidermal junction (DEJ). It calls the boundary detection and the classification algorithm.

```

1 function [ OCT_data ] = LayerDetection2D( OCT_data )
2 origImage = squeeze(mat2gray(OCT_data));
3 Image = sgolay_prompt(origImage);
4
5 %% Detect boundaries
6 nhood = 55;
7 [boundaries, im_p_top, bias] = boundary_detection(Image, nhood);
8
9 %% Classification
10 % Separate points by z-index -> classification
11 % zTol = 150;
12 zTol = 30;
13 % zTol = (sin(linspace(0,pi,length(Image(1,:))))).^2*120+30)';
14 B = classification3(boundaries,zTol);
15
16 % plot selected points
17 figure(10)
18 imagesc(origImage);
19 colormap gray
20 hold on
21 plot(boundaries.outer(:,:)+im_p_top-bias,'k.',...
22 'DisplayName','bo1','LineWidth',1,'Visible','off');
23 plot(boundaries.inner(:,:)+im_p_top-bias,'k.',...
24 'DisplayName','bi1','LineWidth',1,'Visible','off');
25
26 plot(B.outer(:,1), B.outer(:,2)+im_p_top-bias,'k.',...
27 'DisplayName','o1',...
28 'LineWidth',1,...
29 'Visible','off');
30 plot(B.o_smooth(:,1), B.o_smooth(:,2)+im_p_top-bias,'k-',...
31 'DisplayName','os1','LineWidth',1);
32 plot(B.inner3(:,1), B.inner3(:,2)+im_p_top-bias,'r.',...
33 'DisplayName','i3','LineWidth',1,'Visible','off');
34 plot(B.i_smooth3(:,1), B.i_smooth3(:,2)+im_p_top-bias,'r-',...
35 'DisplayName','is3','LineWidth',1);
36 plot(B.inner1(:,1), B.inner1(:,2)+im_p_top-bias,'b.',...

```

B Layer segmentation

```
37 'DisplayName','i1','LineWidth',1,'Visible','off');
38 plot(B.i_smooth1(:,1), B.i_smooth1(:,2)+im_p_top-bias,'b-',...
39 'DisplayName','is1','LineWidth',1);
40 plot(B.inner2(:,1), B.inner2(:,2)+im_p_top-bias,'g.',...
41 'DisplayName','i2','LineWidth',1,'Visible','off');
42 plot(B.i_smooth2(:,1), B.i_smooth2(:,2)+im_p_top-bias,'g-',...
43 'DisplayName','is2','LineWidth',1);
44 axis ij
45 ylim([0 1024])
46 hold off
47
48 end
49
50 function [ ImageOut ] = sgolay_prompt( ImageIn )
51 prompt = {'Enter order m:','Enter framelength n:'};
52 dlg_title = 'Savitzky-Golay Filters';
53 num_lines = [1 50];
54 defaultans = {'5', '51'};
55 answer = inputdlg(prompt,dlg_title,num_lines,defaultans);
56 m = str2double(answer{1});
57 n = str2double(answer{2});
58 ImageOut = sgolayfilt(ImageIn, m, n, [], 1);
59 end
```

B.3 boundary_detection.m

This routine performs the basic detection algorithm for the boundary points. It returns initial candidate data points for the boundaries.

```

1 function [ B, im_p_top, bias ] = boundary_detection( Image, nhood )
2
3 im_size = size(Image);
4 im_height = im_size(1); % z-axis
5 im_max_height = 800;
6 im_width = im_size(2); % x-axis
7 im_p_top = 17;          % image padding top
8 bias = 5;
9 % Minimal thickness of epidermis in pixels/indices
10 thick_min = 10;
11 % Maximal thickness of epidermis in pixels/indices
12 thick_max = 400;
13 % outer boundary (air - horny layer)
14 boundary_1 = NaN(im_width, 2, 2);
15 % inner boundaries
16 boundary_2 = NaN(im_width, 2, 3);
17 max_distance = 250;
18 % b_max_f = [];
19 b_max_ind = NaN;
20 % Minimal index difference for maxima
21 min_ind_dist = 10;
22
23 % process A-scan by A-scan
24 for i = 1:im_width
25     % select column (Image(z,x))
26     col = Image(im_p_top:im_max_height,i);
27     % diff_col = diff(col);
28     diff_col = col;
29     % max value and index of column max
30     [max_f, max_ind] = max(diff_col);
31
32     % First boundary
33     %Step 1: Find all local maxima
34     [peaks,p_locs] = findpeaks(diff_col);
35     % peaks = f(x), p_locs = x (locations)
36     step_1 = [peaks,p_locs];

```

B Layer segmentation

```
37 %Step 2: Only positive values
38 step_2 = step_1(all(step_1(:,1) > 0, 2), :);
39 %Step 3: Only values >= 0.1*max_f
40 step_3 = step_2(all(step_2(:,1) >= 0.1*max_f, 2), :);
41 %Step 4: Only values with a distance of >10 to max_ind
42 step_4 = step_3(all(abs(step_3(:,2)-max_ind) > min_ind_dist, 2), :)
;
43 % append global max
44 step_4 = [step_4;[max_f, max_ind] ];
45 %Step 5: Make sure that x >= x_max (where x_max = max_ind)
46 step_5 = step_4(all(step_4(:,2)>= max_ind, 2),:);
47 %Step 6: Find max and second highest element
48 step_6 = sortrows(step_5, -1);
49 if size(step_5,1)>1
50     % step_6 = step_6(1:2,:);
51     boundary_1(i,:,1) = step_6(1,:);
52     boundary_1(i,:,2) = step_6(2,:);
53 else
54     boundary_1(i,:,1) = step_6(1,:);
55 %     boundary_1(i,:,2) = step_6(1,:);
56 end
57
58 % Second boundary
59 diff_col = diff(col);
60 %     diff_col = col;
61
62 %Step 1: Find all local maxima
63 [peaks,p_locs] = findpeaks(diff_col);
64 % peaks = f(x), p_locs = x (locations
65 step_1 = [peaks,p_locs]; )
66 %Step 2: Only positive values
67 step_2 = step_1(all(step_1(:,1) > 0, 2), :);
68 %Step 3: Only values x-t_m > boundary_1
69 step_3 = step_2(all(step_2(:,2) - thick_min > boundary_1(i,2,1),2)
,,:);
70 %Step 4: Choose maxima where the top neighborhood < bottom
neighborhood
71 %     nhood = 30;
72 if ~isempty(step_3)
73     for j = 1:size(step_3,1)
74         if step_3(j,2) <= nhood
```

```

75     step_3(j,3) = sum(col(1:step_3(j,2)-1));
76     step_3(j,4) = sum(col(step_3(j,2) + 1:step_3(j,2) + nhood));
77     elseif step_3(j,2) >= size(col,1)-nhood
78         step_3(j,3) = sum(col(step_3(j,2)-nhood:step_3(j,2)));
79         step_3(j,4) = sum(col(step_3(j,2)+1:end));
80     else
81         step_3(j,3) = sum(col(step_3(j,2)-nhood:step_3(j,2)-1));
82         step_3(j,4) = sum(col(step_3(j,2)+1:step_3(j,2)+nhood));
83     end
84 end
85 step_4 = step_3(all(step_3(:,3) < step_3(:,4),2),:);
86 else
87     boundary_2(i,:,1) = [NaN, NaN];
88     continue;
89 end
90 %Step 5: Choose only x with reasonable thickness
91 step_5 = step_4(all(step_4(:,2) - boundary_1(i,2) < thick_max, 2),
1:2);
92 if isempty(step_5)
93     boundary_2(i,:,1) = [NaN, NaN];
94     boundary_2(i,:,2) = [NaN, NaN];
95     boundary_2(i,:,3) = [NaN, NaN];
96     boundary_2(i,:,4) = [NaN, NaN];
97     continue;
98 end
99 %Step 6: Only values >= 0.1*max(f(x))
100 st5_sort = sortrows(step_5, -1);
101 st5_max = st5_sort(1,1);
102 st5_ind = st5_sort(1,2);
103 step_6 = step_5(all(step_5(:,1) >= 0.1*st5_max, 2), :);
104 if isempty(step_6)
105     boundary_2(i,:,1) = [NaN, NaN];
106     boundary_2(i,:,2) = [NaN, NaN];
107     boundary_2(i,:,3) = [NaN, NaN];
108     boundary_2(i,:,4) = [NaN, NaN];
109     continue;
110 end
111 %Step 7: Only values with a distance of >10 to st5_ind
112 step_7 = step_6(all(abs(step_6(:,2))-st5_ind) > 10, 2), :);
113 step_7 = [step_7;[st5_max, st5_ind]]; % append global max
114 if isempty(step_7)

```

B Layer segmentation

```
115     boundary_2(i,:,1) = [NaN, NaN];
116     boundary_2(i,:,2) = [NaN, NaN];
117     boundary_2(i,:,3) = [NaN, NaN];
118     boundary_2(i,:,4) = [NaN, NaN];
119     continue;
120 end
121 %Step 8: Find the max or the four
122 % highest elements if available
123 if ~isempty(step_7)
124     step_8 = sortrows(step_7, -1);
125     if size(step_8,1)>3
126         boundary_2(i, :, 1) = step_8(1,:);
127         boundary_2(i, :, 2) = step_8(2,:);
128         boundary_2(i, :, 3) = step_8(3,:);
129         boundary_2(i, :, 4) = step_8(4,:);
130     elseif size(step_8,1) == 3
131         boundary_2(i, :, 1) = step_8(1,:);
132         boundary_2(i, :, 2) = step_8(2,:);
133         boundary_2(i, :, 3) = step_8(3,:);
134         boundary_2(i, :, 4) = [NaN, NaN];
135     elseif size(step_8,1) == 2
136         boundary_2(i, :, 1) = step_8(1,:);
137         boundary_2(i, :, 2) = step_8(2,:);
138         boundary_2(i, :, 3) = [NaN, NaN];
139         boundary_2(i, :, 4) = [NaN, NaN];
140     elseif size(step_8,1) == 1
141         boundary_2(i, :, 1) = step_8(1,:);
142         boundary_2(i, :, 2) = [NaN, NaN];
143         boundary_2(i, :, 3) = [NaN, NaN];
144         boundary_2(i, :, 4) = [NaN, NaN];
145     end
146 else
147     boundary_2(i, :, 1) = [NaN, NaN];
148     boundary_2(i, :, 2) = [NaN, NaN];
149     boundary_2(i, :, 3) = [NaN, NaN];
150     boundary_2(i, :, 4) = [NaN, NaN];
151 end
152 % b_max_ind = boundary_2(i,2,2);
153 end
154
155 boundary_1 = squeeze(boundary_1(:,2,:));
```

```
156 boundary_2 = squeeze(boundary_2(:,2,:));
157
158 % prepare container
159 B.outer = boundary_1;
160 B.inner = boundary_2;
```

B.4 classification3.m

The classification algorithm sorts the candidates provided by the boundary detection algorithm and returns data point sets belonging to the specific boundaries.

```
1 function [ B_out ] = classification3( B_in, zTol )
2 %CLASSIFICATION Summary of this function goes here
3 boundary = [B_in.outer B_in.inner];
4 B = sort(boundary, 2, 'Ascend');
5 B_orig = B;
6 b_len = length(boundary);
7 %   Seperate points by z-index -> classification
8 % zTol = 150;
9 % zTol = (sin(linspace(0,pi/2,b_len)).^2*120+30)';
10 %% Outer boundaries
11 % Classification
12 % take only values from 1st row if not higher than neighbors+
    threshold
13 % B1_min = movmin(B(:,1),15);
14 B1_mean = movmean(B(:,1),20,'omitnan');
15 % B1_min = movmin(B1_mean,15);
16 C = [(1:b_len)',B(:,1)];
17 % C = C(C(:,2) < B1_min+zTol,:);
18 C = C(C(:,2) < B1_mean+10,:);
19 % B1_i = find(B(:,1) < B1_min+zTol);
20 B1_i = C(:,1);
21 B1 = NaN(b_len,1);
22 B1(B1_i) = B(B1_i,1);
23 B(B1_i,1) = NaN;
24 B = sort(B, 2, 'Ascend');
25 %% Inner boundaries
26 % Classification
27 % take only values from 1st row if not higher than neighbors+
    threshold
28 % B2_min = movmin(B(:,1),15);
29 B2_mean = movmean(B(:,1),20,'omitnan');
30 C = [(1:b_len)',B(:,1)];
31 % C = C(C(:,2) < B2_min+zTol,:);
32 C = C(C(:,2) < B2_mean+10,:);
33 B2_i = C(:,1);
34 % B2_i = find(B(:,1) < B2_min+zTol);
```



```

35 B2 = NaN(b_len,1);
36 B2(B2_i) = B(B2_i,1);
37 B(B2_i,1) = NaN;
38 B = sort(B, 2, 'Ascend');
39
40 B3_mean = movmean(B(:,1),20,'omitnan');
41 % B3_mean = smooth(movmean(B(:,1),15,'omitnan'),0.15,'rloess');
42 % B3_max = smooth(movmax(max(B(:,1:2),[],2),15),0.15,'rloess');
43 % B3_max = smooth(movmax(B(:,1),15),0.15,'rloess');
44
45 % B3_mean = NaN(b_len,3);
46 B3_top = NaN(b_len,3);
47 B3_bot = NaN(b_len,3);
48
49 % Remove peaks
50 B3_wp = B(:,1:3);
51 B3_wp(B3_wp >= B3_mean+zTol) = NaN;
52 % Hull
53 B3_max = movmax(max(B3_wp, [], 2),10);
54 B3_min = movmin(min(B3_wp, [], 2),10);
55
56 C_t = B3_wp-B3_min <= 30;
57 C_b = B3_max-B3_wp <= 30;
58 B3_top(C_t) = B3_wp(C_t);
59 B3_bot(C_b) = B3_wp(C_b);
60
61 % Take only the highest values per row of B3_top
62 B3_top = nanmean(B3_top,2);
63 % B3_top = sort(B3_top, 2, 'Ascend');
64 % B3_top = B3_top(:,1);
65 % Take only the lowest values per row of B3_bottom
66 B3_bot = nanmean(B3_bot,2);
67 % B3_bot = sort(B3_bot, 2, 'Descend','MissingPlacement','last');
68 % B3_bot_mean = movmean(mean(B3_bot(:,1:3),2,'omitnan'),20,'omitnan')
    ;
69 % B3_bot = B3_bot(:,1);
70
71 %%
72 outer = [(1:b_len)', B1];
73 inner1 = [(1:b_len)', B2];
74 inner2 = [(1:b_len)', B3_top];

```

B Layer segmentation

```
75 inner3 = [(1:b_len)', B3_bot];
76
77 B_out.outer = outer;
78 B_out.inner1 = inner1;
79 B_out.inner2 = inner2;
80 B_out.inner3 = inner3;
81 B_out.o_smooth = [outer(:,1),smooth(outer(:,2), 0.15, 'rloess')];
82 B_out.i_smooth1 = [inner1(:,1),smooth(inner1(:,2), 0.15, 'rloess')];
83 B_out.i_smooth2 = [inner2(:,1),smooth(inner2(:,2), 0.15, 'rloess')];
84 % Update DEJ smooth
85 B_out.i_smooth3 = [inner3(:,1),smooth(inner3(:,2), 0.15, 'rloess')];
86 end
```

B.5 LayerDetection3D.m

Similar to the 2D version a 3D layer detection is performed returning the dimensions of a suited pigmented lesion. It returns the boundaries and provides data for visual inspection of the lesion geometry.

```

1 function [ OCT ] = LayerDetection3D( OCT, xy )
2 %LayerDetection3D is an OCT image segmentation tool providing a
  boundary
3 %detection and classification of 3D OCT data.
4 %
5 % Author: Arthur Varkentin, M.Sc., scientific staff member
6 % Leibniz Univeritaet Hannover, Hannover Centre for Optical
  Technology - HOT
7 % email address: arthur.varkentin@hot.uni-hannover.de
8 %
9 % June 2017; Last revision: 26-June-2017
10
11 %% Get properties
12 SizeX = OCT.prop.SizeX;
13 SizeY = OCT.prop.SizeY;
14 SizeZ = OCT.prop.SizeZ;
15
16 %% Settings
17 [SGm, SGn] = sgolay_prompt;
18 % zTol_y = 150;
19 zTol_y = 30;
20 % zTol_y = (sin(linspace(0,pi,SizeY)).^2*120+30)';
21 % zTol_x = 150;
22 zTol_x = 30;
23 % zTol_x = (sin(linspace(0,pi/2,SizeX)).^2*120+30)';
24 %% Waitbar
25 % clean up waitbars
26 F = findall(0,'type','figure','tag','TMWaitbar');
27 delete(F);
28 % generate waitbar
29 wb = waitbar(0,'Processing...',...
30             'CreateCancelBtn',...
31             'setappdata(gcf,'canceling',1)');
32 setappdata(wb,'canceling',0)
33 % steps = SizeY;

```

B Layer segmentation

```
34 %% Processing
35 % 3D data by slices
36 % in y direction (x-z slices)
37 for i = 1:SizeY
38     % Check for Cancel button press
39     if getappdata(wb,'canceling')
40         break
41     end
42     tic;
43     % filtering of B-scan to remove high, sharp artifact peaks
44     Image = sgolayfilt(mat2gray(OCT.data(:, :, i)), SGm, SGn, [], 1); %
OCT.data(z,x,y)
45
46     %% Detect boundaries
47     nhoud = 55;
48     [boundaries, im_p_top, bias] = boundary_detection(Image, nhoud);
49
50     %% Classification
51     % Separate points by z-index -> classification
52     OCT.By(i) = classification3(boundaries,zTol_y);
53
54     %%
55     remTime = toc*(SizeY+SizeX-i);
56     timeString = datestr(remTime/(24*60*60), 'MM:SS');
57     waitbar(i / (SizeY+SizeX), wb, ['Processing... Remaining Time: '
timeString])
58 end
59 % in x direction (y-z slices)
60 for i = 1:SizeX
61     % Check for Cancel button press
62     if getappdata(wb,'canceling')
63         break
64     end
65     tic
66     % filtering of B-scan to remove high, sharp artifact peaks
67     Image = sgolayfilt(mat2gray(OCT.data(:, i, :)), SGm, SGn, [], 1); %
OCT.data(z,x,y)
68
69     %% Detect boundaries
70     nhoud = 55;
71     [boundaries, im_p_top, bias] = boundary_detection(Image, nhoud);
```

```

72
73 %% Classification
74 % Seperate points by z-index -> classification
75 OCT.Bx(i) = classification3(boundaries,zTol_x);
76
77 %%
78 remTime = toc*(SizeX-i);
79 timeString = datestr(remTime/(24*60*60), 'MM:SS');
80 waitbar(i / (SizeY+SizeX) + 0.5, wb, ['Processing... Remaining
    Time: ' timeString])
81 end
82 %%
83 delete(wb); % Close waitbar
84 end
85
86 function [ m, n ] = sgolay_prompt( )
87 %SGOLAY_PROMPT Summary of this function goes here
88 % Detailed explanation goes here
89 prompt = {'Enter order m:', 'Enter framelength n:'};
90 dlg_title = 'Savitzky-Golay Filters';
91 num_lines = [1 50];
92 defaultans = {'5', '51'};
93 answer = inputdlg(prompt,dlg_title,num_lines,defaultans);
94 m = str2double(answer{1});
95 n = str2double(answer{2});
96 % input_data.img_h.CData = sgolayfilt(input_data.img_h.CData, m, n,
    [], 1);
97 end

```

B.6 EpiSeg_Example.m

This file is an example script which explains how to call the main program script and how to handle the generated output of EpiSeg_GetData.m. At least, the data is plotted to visualize the result.

```
1 addpath('./Functions');
2 addpath('./Functions/gridfitdir');
3 OCT = EpiSeg_GetData('H:\Seafiler\Meine Bibliothek\Messungen\OCT\');
4 %% Get properties
5 SizeX = OCT.prop.SizeX;
6 SizeY = OCT.prop.SizeY;
7 SizeZ = OCT.prop.SizeZ;
8 x = 1:SizeX;
9 y = 1:SizeY;
10 [x, y] = meshgrid(x, y);
11 xi = linspace(1,SizeX,SizeY);
12 yi = linspace(1,SizeY,SizeX);
13 % [X,Y] = meshgrid(xi,yi);
14
15 %% variable definitions
16 refInd = 1.36; % mean refractive index of tissue (1.36)
17 % axis definitions
18 xAxis=@(x)(OCT.prop.SpacingX .*x); % convert to mm
19 xAxisList= xAxis(1:OCT.prop.SizeX); % fill list of xAxis values
20
21 yAxis=@(y)(OCT.prop.SpacingY .*y); % convert to mm
22 yAxisList= yAxis(1:OCT.prop.SizeY); % fill list of yAxis values
23
24 zAxis=@(z)(OCT.prop.SpacingZ .*z./refInd); % rescale zAxis (depth)
25 zAxisList= zAxis(1:OCT.prop.SizeZ); % fill list of zAxis values
26
27 %% Perform layer detection and classification of measurement
28 OCT = LayerDetection3D(OCT,'y');
29 %%
30 Horn_y = zeros(SizeY,SizeX);
31 Horn_x = zeros(SizeX,SizeY);
32 DEJ_y = Horn_y;
33 DEJ_x = Horn_x;
34 Skin_y = Horn_y;
35 Skin_x = Horn_x;
```

```

36 for i = 1:SizeY
37   Horn_y(i,:) = OCT.By(i).o_smooth(:,2);
38 %   layerVal(i,:) = OCT.B(i).o_smooth(:,3,1);
39
40 % allocate NaN matrix and fill it with x-z pairs of classified layers
41 %   temp = NaN(SizeY,1);
42 %   temp(OCT.By(i).i_smooth1(:,1)) = OCT.By(i).i_smooth1(:,2);
43 %   H_Derm_y(i,:) = temp;
44
45   temp = NaN(SizeY,1);
46   temp(OCT.By(i).i_smooth3(:,1)) = OCT.By(i).i_smooth3(:,2);
47   DEJ_y(i,:) = temp;
48   temp2 = NaN(SizeY,1);
49   temp2(OCT.By(i).i_smooth1(:,1)) = OCT.By(i).i_smooth1(:,2);
50   Skin_y(i,:) = temp2;
51 end
52
53 for i = 1:SizeX
54   Horn_x(i,:) = OCT.Bx(i).o_smooth(:,2);
55 %   layerVal(i,:) = OCT.B(i).o_smooth(:,3,1);
56
57   % allocate NaN matrix and fill it with x-z pairs of classified
   layers
58 %   temp = NaN(SizeX,1);
59 %   temp(OCT.Bx(i).i_smooth1(:,1)) = OCT.Bx(i).i_smooth1(:,2);
60 %   H_Derm_x(i,:) = temp;
61
62   temp = NaN(SizeX,1);
63   temp(OCT.Bx(i).i_smooth3(:,1)) = OCT.Bx(i).i_smooth3(:,2);
64   DEJ_x(i,:) = temp;
65   temp2 = NaN(SizeX,1);
66   temp2(OCT.Bx(i).i_smooth1(:,1)) = OCT.Bx(i).i_smooth1(:,2);
67   Skin_x(i,:) = temp2;
68 end
69 %%
70
71 % valid = ~isnan(ISm3Z);
72 % zgrid = griddata(x(valid), y(valid), ISm3Z(valid), x, y);
73 % zi = interp2(x, y, zgrid, X, Y, 'spline');
74 DEJ_x = DEJ_x';
75 Horn_x = Horn_x';

```

B Layer segmentation

```
76 % DEJ_x = Skin_x';
77 % DEJ_y = Skin_y;
78
79 Horn = gridfit([x(:); x(:)], [y(:); y(:)], [Horn_x(:); Horn_y(:)], xi
    , yi, 'smoothness',10);
80 Horn(Horn<1) = 1;
81 DEJ = gridfit([x(:); x(:)], [y(:); y(:)], [DEJ_x(:); DEJ_y(:)], xi,
    yi, 'smoothness',100);
82 DEJ(DEJ<1) = 1;
83 %%
84 sh = figure(1);
85 surf(xAxisList,yAxisList,zAxis(Horn_y), 'EdgeColor', 'none', 'FaceColor'
    , [0.8,0.8,0.8], 'Visible', 'off');
86 set(gca, 'ZDir', 'reverse');
87 xlabel('x Position (mm)')
88 ylabel('y Position (mm)')
89 zlabel('Corrected Depth (mm)')
90 hold on
91 surf(xAxisList,yAxisList,zAxis(Horn_x), 'EdgeColor', 'none', 'FaceColor'
    , [0.8,0.8,0.8], 'Visible', 'off');
92 % surf(xi,yi,StratCorn, 'EdgeColor', 'none', 'FaceColor', [0.8,0.8,0.8], '
    FaceAlpha',0.5, 'Visible', 'on');
93 surf(xAxisList,yAxisList,zAxis(Horn), 'EdgeColor', 'none', 'FaceColor', '
    red', 'FaceAlpha',0.8, 'Visible', 'on');
94 surf(xAxisList,yAxisList,zAxis(DEJ), 'EdgeColor', 'none', 'FaceColor', '
    blue', 'FaceAlpha',0.8, 'Visible', 'on');
95 % surf(xi,yi,DEJ, 'EdgeColor', 'none', 'FaceColor', 'blue', 'FaceAlpha
    ',0.8);
96 camlight right;
97 lighting phong;
98 % shading interp
99 % hold off
100 %
101 % [X,Y,Z] = meshgrid(1:SizeX,SizeY,1:1024);
102 % shiftData = shiftdim(OCT.data(1:1024,1:SizeX,1:SizeY),1);
103 % % figure(2);
104 % % pcshow([X(:),Y(:),Z(:)],shiftData(:));
105 % % scatter3(X(:),Y(:),Z(:), [],shiftData(:));
106 %
107 % %%
108 % Volume = zeros(SizeX,SizeY,1024);
```



```

109 % Surface = zeros(SizeX,SizeY,1024);
110 % for i = 1:SizeY
111 %     Surface(1,i,floor(Horn(i,1)):ceil(DEJ(i,1))) = 1;
112 %     Surface(SizeX,i,floor(Horn(i,SizeY)):ceil(DEJ(i,SizeY))) = 1;
113 %     for j= 1:SizeX
114 %         Volume(j,i,floor(Horn(i,j)):ceil(DEJ(i,j))) = shiftData(j,i
, floor(Horn(i,j)):ceil(DEJ(i,j)));
115 %         if i == 1
116 %             Surface(j,1,floor(Horn(1,j)):ceil(DEJ(1,j))) = 1;
117 %         elseif i == SizeY
118 %             Surface(j,SizeY,floor(Horn(SizeX,j)):ceil(DEJ(SizeX,j))
) = 1;
119 %         else
120 %             Surface(j,i,[floor(Horn(i,j)) ceil(DEJ(i,j))]) = 1;
121 %         end
122 %     end
123 % end
124 %
125 % % hold on
126 %
127 % Volume = permute(Volume,[2,1,3]);
128 % p1 = patch(isosurface(xAxisList,yAxisList,zAxisList,Volume,0));
129 % p2 = patch(isocaps(xAxisList,yAxisList,zAxisList,Volume,0));
130 % reducepatch(p1,0.025);
131 % reducepatch(p2,0.025);
132 % p = [p1, p2];
133 % isonormals(xAxisList,yAxisList,zAxisList,Volume,p(1));
134 % set(p,'EdgeColor','black','EdgeAlpha',0.4,'FaceColor','green','
FaceAlpha',0.4,'FaceLighting','gouraud');
135 % set(gca,'ZDir','reverse');
136 % view(3)
137
138 %% Thickness Map
139 Thickness = zAxis(DEJ) - zAxis(Horn);
140 Thickness(Thickness<0) = 0;
141 Thickness_c = zeros(SizeX,SizeY);
142 Th_p = 40; % Thickness padding
143 Thickness_c(Th_p:SizeX-Th_p,Th_p:SizeY-Th_p) = Thickness(Th_p:SizeX-
Th_p,Th_p:SizeY-Th_p);
144 [M,I] = max(Thickness_c(:));
145 [I_row, I_col] = ind2sub(size(Thickness),I);

```

B Layer segmentation

```
146
147 % Lateral size assessment
148
149 % hold off
150 % h = imellipse;
151 % addNewPositionCallback(h,@(p) title(mat2str(p,3)));
152 % fcn = makeConstrainToRectFcn('imellipse',get(gca,'XLim'),get(gca,'
    YLim'));
153 % setPositionConstraintFcn(h,fcn);
154
155 ElSel = regionprops(imbinarize(Thickness, M/2), 'Orientation', '
    MajorAxisLength', ...
156     'MinorAxisLength', 'Eccentricity', 'Centroid');
157
158 phi = linspace(0,2*pi,100);
159 cosphi = cos(phi);
160 sinphi = sin(phi);
161 % Select biggest ellipse
162 [M_el,I_el] = max([ElSel(:).MajorAxisLength]);
163 ElSel = ElSel(I_el);
164 % Weight center of ellipse
165 x_c = ElSel.Centroid(1);
166 y_c = ElSel.Centroid(2);
167 % size of major and minar axis
168 a = ElSel.MajorAxisLength/2;
169 b = ElSel.MinorAxisLength/2;
170 % rotation angle
171 theta = pi*ElSel.Orientation/180;
172 % rotation matrix
173 R = [ cos(theta)   sin(theta)
174       -sin(theta)   cos(theta)];
175
176 Ellipse = [a*cosphi; b*sinphi];
177 Eli4P = [a*cos([0 pi pi/2 3/2*pi]); b*sin([0 pi pi/2 3/2*pi])];
178 Ellipse = R*Ellipse;
179 Eli4P = R*Eli4P;
180
181 x = Ellipse(1,:) + x_c;
182 y = Ellipse(2,:) + y_c;
183 x_maj = Eli4P(1,1:2) + x_c;
184 y_maj = Eli4P(2,1:2) + y_c;
```

```

185 x_min = Eli4P(1,3:4) + x_c;
186 y_min = Eli4P(2,3:4) + y_c;
187
188 figure(2)
189 fs = 10;
190 imagesc(xAxisList, yAxisList, Thickness, [0 M]);
191 axis image
192 xlabel('x Position (mm)')
193 ylabel('y Position (mm)')
194 hold on
195 plot(xAxis(x),yAxis(y),'r','LineWidth',2);
196 plot(xAxis(x_maj), yAxis(y_maj),'r','LineWidth',2);
197 plot(xAxis(x_min), yAxis(y_min),'r','LineWidth',2);
198 plot(xAxis(I_col), yAxis(I_row),'sb');
199 text(xAxis(I_col), yAxis(I_row+10),[num2str(M) ' mm'],'
    HorizontalAlignment','center','FontSize',fs,'FontWeight','bold');
200 text(xAxis(x_maj(2)+10), yAxis(y_maj(2)-10),[num2str(xAxis(2*a) ' mm
    '],'HorizontalAlignment','left','Color','r','Rotation',theta*180/pi,'
    FontSize',fs,'FontWeight','bold');
201 text(xAxis(x_min(2)+10), yAxis(y_min(2)+10),[num2str(xAxis(2*b)) ' mm
    '],'HorizontalAlignment','left','Color','r','Rotation',theta*180/pi
    -90,'FontSize',fs,'FontWeight','bold');
202 hold off
203
204 %%
205 figure(1)
206 plot3(xAxis([I_col I_col]),yAxis([I_row I_row]),zAxis([DEJ(I_row,
    I_col) Horn(I_row, I_col)]),'LineWidth',3,'Color','red');
207 text(xAxis(I_col), yAxis(I_row), zAxis(Horn(I_row, I_col)-40),[
    num2str(M) ' mm'],'HorizontalAlignment','center','FontSize',fs,'
    FontWeight','bold');
208 [A,B,C] = cylinder(a);
209 h_eli = surf(xAxis([x; x]),yAxis([y; y]),zAxis([repmat(DEJ(I_row,
    I_col),100,1) repmat(Horn(I_row, I_col),100,1)]));
210 set(h_eli,'EdgeColor','none','FaceColor','blue','FaceAlpha',0.4);
211 % f = figure(3);
212 % camproj('perspective')
213 %
214 % T = [1 0 0 0;0 1 0 0;0 0 2.5 0];
215 % h = myslicer(squeeze(shiftData),T);
216 % colormap gray;

```

B Layer segmentation

```
217 % % axis off;
218 % % axis equal
219 %
220 % pause;
221 %
222 % delete(h);
223 % close(f);
224
225 %%
226 origImage = squeeze(mat2gray(OCT.data(:,I_row,:)));
227 % origImage = squeeze(mat2gray(OCT.data(:,:,I_col)));
228 % Image = sgolay_prompt(origImage);
229 prompt = {'Enter order m:', 'Enter framelength n:'};
230 dlg_title = 'Savitzky-Golay Filters';
231 num_lines = [1 50];
232 defaultans = {'5', '51'};
233 answer = inputdlg(prompt,dlg_title,num_lines,defaultans);
234 m = str2double(answer{1});
235 n = str2double(answer{2});
236 % input_data.img_h.CData = sgolayfilt(input_data.img_h.CData, m, n,
    [], 1);
237 Image = sgolayfilt(origImage, m, n, [], 1);
238
239 prompt = {'Enter NumTiles m:', 'Enter NumTiles n:'};
240 dlg_title = 'Contrast-limited adaptive histogram equalization (CLAHE)
    ';
241 num_lines = [1 50];
242 defaultans = {'8', '8'};
243 answer = inputdlg(prompt,dlg_title,num_lines,defaultans);
244 m = str2double(answer{1});
245 n = str2double(answer{2});
246 conImage = adapthisteq(Image, 'clipLimit',0.02, 'Distribution','
    exponential', 'NumTiles',[m n]);
247
248 % Detect boundaries
249 nhood = 55;
250 [boundaries, im_p_top, bias] = boundary_detection(Image, nhood);
251
252 % Classification
253 zTol = 300;
254 % zTol = (sin(linspace(0,pi,length(Image(1,:))))).^2*120+30)';
```

```

255 % Seperate points by z-index -> classification
256 B = classification3(boundaries,zTol);
257
258 % B = OCT.Bx(I_row);
259
260 % plot selected points
261 figure(10)
262 imagesc(xAxisList,zAxisList,conImage);
263 % colormap gray
264 hold on
265 plot(xAxisList, zAxis(boundaries.outer(:,1)+im_p_top-bias), '.', 'Color
', [0, 0, 1], 'DisplayName', 'bo1', 'LineWidth', 1, 'Visible', 'off');
266 plot(xAxisList, zAxis(boundaries.outer(:,2)+im_p_top-bias), '.', 'Color
', [0, 0.2, 1], 'DisplayName', 'bo2', 'LineWidth', 1, 'Visible', 'off');
267 plot(xAxisList, zAxis(boundaries.inner(:,1)+im_p_top-bias), '.', 'Color
', [0, 0.4, 1], 'DisplayName', 'bi1', 'LineWidth', 1, 'Visible', 'off');
268 plot(xAxisList, zAxis(boundaries.inner(:,2)+im_p_top-bias), '.', 'Color
', [0, 0.6, 1], 'DisplayName', 'bi2', 'LineWidth', 1, 'Visible', 'off');
269 plot(xAxisList, zAxis(boundaries.inner(:,3)+im_p_top-bias), '.', 'Color
', [0, 0.8, 1], 'DisplayName', 'bi3', 'LineWidth', 1, 'Visible', 'off');
270 plot(xAxisList, zAxis(boundaries.inner(:,4)+im_p_top-bias), '.', 'Color
', [0, 1, 1], 'DisplayName', 'bi4', 'LineWidth', 1, 'Visible', 'off');
271
272 plot(xAxis(B.outer(:,1)), zAxis(B.outer(:,2)+im_p_top-bias), 'k.', '
  DisplayName', 'o1', 'LineWidth', 1, 'Visible', 'off');
273 plot(xAxis(B.o_smooth(:,1)), zAxis(B.o_smooth(:,2)+im_p_top-bias), 'k-
', 'DisplayName', 'os1', 'LineWidth', 1);
274 plot(xAxis(B.inner3(:,1)), zAxis(B.inner3(:,2)+im_p_top-bias), 'r.', '
  DisplayName', 'i3', 'LineWidth', 1, 'Visible', 'off');
275 plot(xAxis(B.i_smooth3(:,1)), zAxis(B.i_smooth3(:,2)+im_p_top-bias), '
r-', 'DisplayName', 'is3', 'LineWidth', 1);
276 plot(xAxis(B.inner1(:,1)), zAxis(B.inner1(:,2)+im_p_top-bias), 'g.', '
  DisplayName', 'i1', 'LineWidth', 1, 'Visible', 'off');
277 plot(xAxis(B.i_smooth1(:,1)), zAxis(B.i_smooth1(:,2)+im_p_top-bias), '
g-', 'DisplayName', 'is1', 'LineWidth', 1);
278 plot(xAxis([I_row I_row]), zAxis([B.o_smooth(I_row,2) B.i_smooth3(
  I_row,2)]+im_p_top-bias), 'LineWidth', 3, 'Color', 'cyan');
279 axis ij
280 xlabel('x Position (mm)')
281 ylabel('Corrected Depth (mm)')
282 colormap gray

```

B Layer segmentation

```
283 % ylim([0 1024])
284 axis equal
285 axis tight
286
287 hold off
288
289 %
290 figure(11)
291 AScan = squeeze(mat2gray(OCT.data(:,I_row,I_col)));
292 % sAScan = Image(:,I_col);
293 sAScan = smooth(AScan,51,'sgolay',5);
294 plot(zAxisList, AScan)
295 hold on
296 plot(zAxisList, sAScan)
297 hold off
298 xlabel('Corrected Depth (mm)')
299 ylabel('Intensity (a.u.)')
300 xlim([0.1 2.7])
301 ylim([0.6 1.05])
```

Bibliography

1. SIMÕES, M. C. F., J. J. S. SOUSA, and PAIS, A. A. C. C.: ‘Skin cancer and new treatment perspectives: a review: A review’. *Cancer Lett.* (2015), vol. 357(1): pp. 8–42. DOI: 10.1016/j.canlet.2014.11.001 (cit. on pp. 1, 63, 69).
2. A. PFLUGFELDER, C. KOCHS, C. GARBE, D. SCHADENDORF, ed.: *S3-Leitlinie "Diagnostik, Therapie und Nachsorge des Melanoms": AWMF-Register-Nummer: 032-024OL : Leitlinie (Langversion)*. Germering: Zuckschwerdt, 2013. ISBN: 978-3-86371-079-8 (cit. on pp. 1, 64).
3. BESSOUD, BERTRAND, NATHALIE LASSAU, SERGE KOSCIELNY, CHRISTINE LONGVERT, MARIE-FRANCOISE AVRIL, PIERRE DUVILLARD, VALÉRIE ROUFFIAC, JERÔME LECLÈRE, and ALAIN ROCHE: ‘High-frequency sonography and color Doppler in the management of pigmented skin lesions’. *Ultrasound Med. Biol.* (2003), vol. 29(6): pp. 875–879. DOI: 10.1016/S0301-5629(03)00035-8 (cit. on pp. 2, 64, 69).
4. GAMBICHLER, THILO, GEORG MOUSSA, KATHARINA BAHRENBERG, MICHAEL VOGT, HELMUT ERMERT, DIRK WEYHE, PETER ALTMAYER, and KLAUS HOFFMANN: ‘Preoperative ultrasonic assessment of thin melanocytic skin lesions using a 100-MHz ultrasound transducer: a comparative study’. *Dermatol. Surg.* (2007), vol. 33(7): pp. 818–824. DOI: 10.1111/j.1524-4725.2007.33175.x (cit. on pp. 2, 64, 65).
5. VILANA, RAMÓN, SUSANA PUIG, MARCELO SANCHEZ, MATTIA SQUARCIA, ALEXANDRA LOPEZ, TERESA CASTEL, and JOSEP MALVEHY: ‘Preoperative assessment of cutaneous melanoma thickness using 10-MHz sonography’. *AJR. Am. J. Roentgenol.* (2009), vol. 193(3): pp. 639–643. DOI: 10.2214/AJR.08.1387 (cit. on pp. 2, 64).
6. MACHET, LAURENT, VÉRONIQUE BELOT, MICHAEL NAOURI, MICHEL BOKA, YOUSSEF MOURTADA, BRUNO GIRAUDEAU, BORIS LAURE, ADELIN PERINAUD, MARIE-CHRISTINE MACHET, and LOÏC VAILLANT: ‘Preoperative measurement of thickness of cutaneous melanoma using high-resolution 20 MHz ultrasound imaging: A monocenter prospective study and systematic review of the literature: A Monocenter Prospective Study and Systematic Review of the Literature’. *Ultrasound Med. Biol.* (2009), vol. 35(9): pp. 1411–1420. DOI: 10.1016/j.ultrasmedbio.2009.03.018 (cit. on pp. 2, 64, 65).

7. CALIN, MIHAELA ANTONINA, SORIN VIOREL PARASCA, ROXANA SAVASTRU, MARIAN ROMEO CALIN, and SIMONA DONTU: ‘Optical techniques for the noninvasive diagnosis of skin cancer’. *J. Cancer Res. Clin. Oncol.* (2013), vol. 139(7): pp. 1083–1104. DOI: 10.1007/s00432-013-1423-3 (cit. on pp. 2, 64).
8. VARKENTIN, ARTHUR, MIKHAIL MAZURENKA, ELIAS BLUMENROTHER, MERVE MEINHARDT-WOLLWEBER, MAIK RAHLVES, SIGRID M. C. BROEKAERT, SUSANNE SCHAD-TRCKA, STEFFEN EMMERTINST, UWE MORGNER, BERNHARD ROTH, ELIAS BLUMENRÖTHER, and SUSANNE SCHÄD-TRCKA: ‘Comparative study of presurgical skin infiltration depth measurements of melanocytic lesions with OCT and high frequency ultrasound’. *J Biophotonics* (2017), vol. 10(6-7): pp. 854–861. DOI: 10.1002/jbio.201600139 (cit. on pp. 2, 68–71, 73).
9. BELL, A. G.: ‘On the production and reproduction of sound by light’. *Am. J. Sc.* (1880), vol. s3-20(118): pp. 305–324. DOI: 10.2475/ajs.s3-20.118.305 (cit. on pp. 2, 86).
10. SCHLEUSENER, JOHANNES, CARINA REBLE, MARTINA C. MEINKE, and JÜRGEN HELFMANN: ‘Raman spectroscopy for the discrimination of cancerous and normal skin’. *Photonics Lasers Med* (2015), vol. 4(2). DOI: 10.1515/plm-2014-0043 (cit. on p. 2).
11. STEVENS, O., PETTERSON I. E. IPING, J. C. DAY, and N. STONE: ‘Developing fibre optic Raman probes for applications in clinical spectroscopy’. *Chem Soc Rev* (2016), vol. 45(7): pp. 1919–1934. DOI: 10.1039/c5cs00850f (cit. on p. 2).
12. PENCE, I. and A. MAHADEVAN-JANSEN: ‘Clinical instrumentation and applications of Raman spectroscopy’. *Chem Soc Rev* (2016), vol. 45(7): pp. 1958–1979. DOI: 10.1039/c5cs00581g (cit. on p. 2).
13. MADHERO88 AND M.KOMORNICZAK: *File:Skin layers.svg - Wikimedia Commons: Madhero88 and M.Komorniczak* (https://commons.wikimedia.org/wiki/File:Skin_layers.svg), „Skin layers“, <https://creativecommons.org/licenses/by-sa/3.0/legalcode>. 2017. URL: https://commons.wikimedia.org/wiki/File:Skin_layers.svg (visited on 04/05/2017) (cit. on p. 6).
14. GARCIA-URIBE, ALEJANDRO, ELIZABETH B. SMITH, JUN ZOU, MADELEINE DUVIC, VICTOR PRIETO, and LIHONG V. WANG: ‘In-vivo characterization of optical properties of pigmented skin lesions including melanoma using oblique incidence diffuse reflectance spectrometry’. *J. Biomed. Opt.* (2011), vol. 16(2): p. 020501. DOI: 10.1117/1.3536509 (cit. on p. 8).

-
15. FRIEBEL, MORITZ, JURGEN HELFMANN, UWE NETZ, and MARTINA MEINKE: 'Influence of oxygen saturation on the optical scattering properties of human red blood cells in the spectral range 250 to 2,000 nm'. *J. Biomed. Opt.* (2009), vol. 14(3): p. 034001. DOI: 10.1117/1.3127200 (cit. on p. 8).
 16. STRUTT, HON J. W.: 'LVIII. On the scattering of light by small particles'. (1871), vol. 41(275): pp. 447–454. DOI: 10.1080/14786447108640507 (cit. on pp. 8, 9).
 17. MIE, GUSTAV: 'Beiträge zur Optik trüber Medien, speziell kolloidaler Metal-lösungen'. *Ann. Phys.* (1908), vol. 330(3): pp. 377–445. DOI: 10.1002/andp.19083300302 (cit. on pp. 8, 10).
 18. BASHKATOV, A. N., E. A. GENINA, V. I. KOCHUBEY, and V. V. TUCHIN: 'Optical properties of human skin, subcutaneous and mucous tissues in the wavelength range from 400 to 2000 nm'. *J. Phys. D: Appl. Phys.* (2005), vol. 38(15): pp. 2543–2555. DOI: 10.1088/0022-3727/38/15/004 (cit. on p. 9).
 19. AROCA, RICARDO: *Surface-enhanced vibrational spectroscopy*. Hoboken, N.J.: Wiley, 2007. ISBN: 0471607312 (cit. on p. 10).
 20. SMEKAL, ADOLF: 'Zur Quantentheorie der Dispersion'. *Naturwissenschaften* (1923), vol. 11(43): pp. 873–875. DOI: 10.1007/BF01576902 (cit. on p. 10).
 21. RAMAN, C. V. and K. S. KRISHNAN: 'A New Type of Secondary Radiation'. *Nature* (1928), vol. 121(3048): pp. 501–502. DOI: 10.1038/121501c0 (cit. on p. 10).
 22. AGACHE, PIERRE and PHILIPPE HUMBERT, eds.: *Measuring the skin*. Berlin: Springer, 2004. ISBN: 3540017712. URL: <http://www.loc.gov/catdir/enhancements/fy0817/2003057310-d.html> (cit. on p. 10).
 23. STEWART, BERNARD W. and CHRISTOPHER P. WILD: *World Cancer Report 2014*. Online-Ausg. EBL-Schweitzer. Lyon: International Agency for Research on Cancer/World Health Organization, 2014. ISBN: 9283204433 (cit. on pp. 11, 12).
 24. BARNES, BENJAMIN, ed.: *Bericht zum Krebsgeschehen in Deutschland 2016*. Berlin: Robert Koch-Institut, 2016. ISBN: 9783896062796 (cit. on p. 11).
 25. NACHBAR, F., W. STOLZ, T. MERKLE, A. B. COGNETTA, T. VOGT, M. LANDTHALER, P. BILEK, O. BRAUN-FALCO, and G. PLEWIG: 'The ABCD rule of dermatoscopy. High prospective value in the diagnosis of doubtful melanocytic skin lesions'. (1994), vol. 30(4): pp. 551–559 (cit. on p. 11).
 26. ALEXILUSMEDICAL: *Stadiums of Melanoma*. Ed. by SHUTTERSTOCK. 2017 (cit. on p. 12).

27. BALCH, C. M. et al.: ‘Final version of the American Joint Committee on Cancer staging system for cutaneous melanoma’. (2001), vol. 19(16): pp. 3635–3648. DOI: 10.1200/JCO.2001.19.16.3635 (cit. on p. 12).
28. CHOMA, MICHAEL, MARINKO SARUNIC, CHANGHUEI YANG, and JOSEPH IZATT: ‘Sensitivity advantage of swept source and Fourier domain optical coherence tomography’. *Opt. Express* (2003), vol. 11(18): p. 2183. DOI: 10.1364/OE.11.002183 (cit. on pp. 15, 17).
29. WIENER, NORBERT: ‘Generalized harmonic analysis’. *Acta Math.* (1930), vol. 55(0): pp. 117–258. DOI: 10.1007/BF02546511 (cit. on pp. 16, 23).
30. AN, LIN, PENG LI, TUENG T. SHEN, and RUIKANG WANG: ‘High speed spectral domain optical coherence tomography for retinal imaging at 500,000 A-lines per second’. *Biomed. Opt. Express* (2011), vol. 2(10): pp. 2770–2783. DOI: 10.1364/B0E.2.002770 (cit. on p. 17).
31. YUN, S. H., G. J. TEARNEY, J. F. de BOER, and B. E. BOUMA: ‘Pulsed-source and swept-source spectral-domain optical coherence tomography with reduced motion artifacts’. *Opt. Express* (2004), vol. 12(23): p. 5614. DOI: 10.1364/OPEX.12.005614 (cit. on p. 17).
32. SPAIDE, RICHARD F., JAMES G. FUJIMOTO, and NADIA K. WAHEED: ‘IMAGE ARTIFACTS IN OPTICAL COHERENCE TOMOGRAPHY ANGIOGRAPHY’. (2015), vol. 35(11): pp. 2163–2180. DOI: 10.1097/IAE.0000000000000765 (cit. on p. 18).
33. HUBER, R., M. WOJTKOWSKI, and J. G. FUJIMOTO: ‘Fourier Domain Mode Locking (FDML): A new laser operating regime and applications for optical coherence tomography’. *Opt. Express* (2006), vol. 14(8): p. 3225. DOI: 10.1364/OE.14.003225 (cit. on p. 19).
34. DREXLER, WOLFGANG, MENG YANG LIU, ABHISHEK KUMAR, TSCHACKAD KAMALI, ANGELIKA UNTERHUBER, and RAINER A. LEITGEB: ‘Optical coherence tomography today: Speed, contrast, and multimodality’. *J. Biomed. Opt.* (2014), vol. 19(7): p. 071412. DOI: 10.1117/1.JBO.19.7.071412 (cit. on p. 19).
35. NAKAMURA, YOSHIFUMI, SHUICHI MAKITA, MASAHIRO YAMANARI, MASAhide ITOH, TOYOHICO YATAGAI, and YOSHIAKI YASUNO: ‘High-speed three-dimensional human retinal imaging by line-field spectral domain optical coherence tomography’. *Opt. Express* (2007), vol. 15(12): p. 7103. DOI: 10.1364/OE.15.007103 (cit. on p. 19).

-
36. WATANABE, YUUKI, KAZUHIKO YAMADA, and MANABU SATO: ‘Three-dimensional imaging by ultrahigh-speed axial-lateral parallel time domain optical coherence tomography’. *Opt. Express* (2006), vol. 14(12): p. 5201. DOI: 10.1364/OE.14.005201 (cit. on p. 20).
 37. BEAUREPAIRE, E., A. C. BOCCARA, M. LEBEC, L. BLANCHOT, and H. SAINT-JALMES: ‘Full-field optical coherence microscopy’. *Opt. Lett.* (1998), vol. 23(4): p. 244. DOI: 10.1364/OL.23.000244 (cit. on p. 20).
 38. BONIN, TIM, GESA FRANKE, MARTIN HAGEN-EGGERT, PETER KOCH, and GEREON HÜTTMANN: ‘In vivo Fourier-domain full-field OCT of the human retina with 1.5 million A-lines/s’. *Opt Lett* (2010), vol. 35(20): pp. 3432–3434. DOI: 10.1364/OL.35.003432 (cit. on p. 20).
 39. DREXLER, WOLFGANG and JAMES G. FUJIMOTO: *Optical coherence tomography: Technology and applications*. Biological and Medical Physics, Biomedical Engineering. Berlin and New York: Springer, 2008. ISBN: 978-3-540-77549-2 (cit. on pp. 21–24, 32).
 40. VAN LEEUWEN, T. G., D. J. FABER, and M. C. AALDERS: ‘Measurement of the axial point spread function in scattering media using single-mode fiber-based optical coherence tomography’. *IEEE J. Select. Topics Quantum Electron.* (2003), vol. 9(2): pp. 227–233. DOI: 10.1109/JSTQE.2003.813299 (cit. on p. 24).
 41. FABER, DIRK J., VAN DER MEER, FREEK J., AALDERS, MAURICE C. G., and VAN LEEUWEN, TON G.: ‘Quantitative measurement of attenuation coefficients of weakly scattering media using optical coherence tomography’. *Opt. Express* (2004), vol. 12(19): p. 4353. DOI: 10.1364/OPEX.12.004353 (cit. on pp. 25, 35).
 42. MORGNER, U., W. DREXLER, F. X. KÄRTNER, X. D. LI, C. PITRIS, E. P. IPPEN, and J. G. FUJIMOTO: ‘Spectroscopic optical coherence tomography’. *Opt. Lett.* (2000), vol. 25(2): p. 111. DOI: 10.1364/OL.25.000111 (cit. on p. 30).
 43. FABER, DIRK J., EGBERT G. MIK, AALDERS, MAURICE C. G., and VAN LEEUWEN, TON G.: ‘Light absorption of (oxy-)hemoglobin assessed by spectroscopic optical coherence tomography’. *Opt. Lett.* (2003), vol. 28(16): p. 1436. DOI: 10.1364/OL.28.001436 (cit. on p. 30).
 44. BOER, JOHANNES F. de, RAINER LEITGEB, and MACIEJ WOJTKOWSKI: ‘Twenty-five years of optical coherence tomography: The paradigm shift in sensitivity and speed provided by Fourier domain OCT [Invited]’. *Biomed. Opt. Express* (2017), vol. 8(7): p. 3248. DOI: 10.1364/BOE.8.003248 (cit. on p. 32).

45. DEREK J SMITHIES, TORE LINDMO, ZHONGPING CHEN, J STUART NELSON, and THOMAS E MILNER: ‘Signal attenuation and localization in optical coherence tomography studied by Monte Carlo simulation’. *Phys. Med. Biol.* (1998), vol. 43(10): p. 3025. URL: <http://stacks.iop.org/0031-9155/43/i=10/a=024> (cit. on pp. 37, 45, 46).
46. GIUSTO, ARIANNA, ROSALBA SAIJA, MARIA ANTONIA IATÌ, PAOLO DENTI, FERDINANDO BORGHESE, and ORAZIO I. SINDONI: ‘Optical Properties of High-Density Dispersions of Particles: Application to Intralipid Solutions’. *Appl. Opt.* (2003), vol. 42(21): p. 4375. DOI: 10.1364/AO.42.004375 (cit. on p. 37).
47. KODACH, V. M., J. KALKMAN, D. J. FABER, and T. G. VAN LEEUWEN: ‘Quantitative comparison of the OCT imaging depth at 1300 nm and 1600 nm’. (2010), vol. 1(1): pp. 176–185. DOI: 10.1364/B0E.1.000176 (cit. on p. 37).
48. MICHELS, RENE, FLORIAN FOSCHUM, and ALWIN KIENLE: ‘Optical properties of fat emulsions’. *Opt. Express* (2008), vol. 16(8): p. 5907. DOI: 10.1364/OE.16.005907 (cit. on p. 37).
49. BLUMENRÖTHER, E., O. MELCHERT, M. WOLLWEBER, and B. ROTH: ‘Detection, numerical simulation and approximate inversion of optoacoustic signals generated in multi-layered PVA hydrogel based tissue phantoms’. *Photoacoustics* (2016), vol. 4(4): pp. 125–132. DOI: 10.1016/j.pacs.2016.10.002 (cit. on pp. 38, 98).
50. THRANE, LARS: *Optical coherence tomography: Modeling and applications*. Vol. 1217 (EN). Risø-R. Roskilde: Risø National Laboratory and available from: Risø National Laboratory, Information Service Department, 2001. ISBN: 8755027717 (cit. on p. 45).
51. ALERSTAM, ERIK, WILLIAM CHUN YIP LO, TIANYI DAVID HAN, JONATHAN ROSE, STEFAN ANDERSSON-ENGELS, and LOTHAR LILGE: ‘Next-generation acceleration and code optimization for light transport in turbid media using GPUs’. *Biomed. Opt. Express* (2010), vol. 1(2): p. 658. DOI: 10.1364/B0E.1.000658 (cit. on pp. 45, 47).
52. THRANE, LARS, HAROLD T. YURA, and PETER E. ANDERSEN: ‘Analysis of optical coherence tomography systems based on the extended Huygens–Fresnel principle’. *J. Opt. Soc. Am. A* (2000), vol. 17(3): p. 484. DOI: 10.1364/JOSAA.17.000484 (cit. on p. 46).
53. NGUYEN, V. DUC, D. J. FABER, E. VAN DER POL, T. G. VAN LEEUWEN, and J. KALKMAN: ‘Dependent and multiple scattering in transmission and backscattering optical coherence tomography’. *Opt. Express* (2013), vol. 21(24): p. 29145. DOI: 10.1364/OE.21.029145 (cit. on p. 46).

-
54. KALKMAN, J., A. V. BYKOV, D. J. FABER, and T. G. VAN LEEUWEN: ‘Multiple and dependent scattering effects in Doppler optical coherence tomography’. *Opt. Express* (2010), vol. 18(4): p. 3883. DOI: 10.1364/OE.18.003883 (cit. on pp. 46, 52, 59).
 55. *Handbook of Coherent-Domain Optical Methods: Analysis in Low and High Scattering Media*. 2nd ed. 2013. SpringerLink : Bücher. New York, NY: Springer New York, 2013: pp. 923–944. ISBN: 978-1-4614-5175-4. DOI: 10.1007/978-1-4614-5176-1{\textunderscore}21 (cit. on p. 46).
 56. ALMASIAN, MITRA, NIENKE BOSSCHAART, VAN LEEUWEN, TON G., and DIRK J. FABER: ‘Validation of quantitative attenuation and backscattering coefficient measurements by optical coherence tomography in the concentration-dependent and multiple scattering regime’. (2015), vol. 20(12): p. 121314. DOI: 10.1117/1.JBO.20.12.121314 (cit. on pp. 46, 60).
 57. FEDOSSEEVA, MARINA S., MIKHAIL Y. KIRILLIN, ALEXANDER V. PRIEZHEV, and RISTO MYLLYLÄ: ‘Estimation of contribution of multiple scattering into the optical coherence tomography signal from layers of different biological tissues’. *Saratov, Russia*. Ed. by TUCHIN, VALERY V. SPIE Proceedings. SPIE, 2005: pp. 283–290. DOI: 10.1117/12.634665 (cit. on p. 46).
 58. KARAMATA, BORIS, PATRICK LAMBELET, MARKUS LAUBSCHER, MARCEL LEUTENEGGER, STÉPHANE BOURQUIN, and THEO LASSER: ‘Multiple scattering in optical coherence tomography I Investigation and modeling’. *J. Opt. Soc. Am. A* (2005), vol. 22(7): p. 1369. DOI: 10.1364/JOSAA.22.001369 (cit. on p. 46).
 59. YAO, GANG and LIHONG V. WANG: ‘Monte Carlo simulation of an optical coherence tomography signal in homogeneous turbid media’. *Phys. Med. Biol.* (1999), vol. 44(9): pp. 2307–2320. DOI: 10.1088/0031-9155/44/9/316 (cit. on p. 49).
 60. WANG, RUIKANG K.: ‘Signal degradation by multiple scattering in optical coherence tomography of dense tissue: A Monte Carlo study towards optical clearing of biotissues’. *Phys. Med. Biol.* (2002), vol. 47(13): pp. 2281–2299. DOI: 10.1088/0031-9155/47/13/307 (cit. on p. 49).
 61. VARKENTIN, ARTHUR, MAYA OTTE, MERVE MEINHARDT-WOLLWEBER, MAIK RAHLVES, MIKHAIL MAZURENKA, UWE MORGNER, and BERNHARD ROTH: ‘Simple model to simulate OCT-depth signal in weakly and strongly scattering homogeneous media’. *J. Opt.* (2016), vol. 18(12): p. 125302. DOI: 10.1088/2040-8978/18/12/125302 (cit. on pp. 50, 51, 54–59).
 62. ZANNONI, ALBERTO: *On the Quantization of the Monoatomic Ideal Gas*. URL: <http://arxiv.org/pdf/cond-mat/9912229v1> (cit. on p. 51).

63. DIRAC, P. A. M.: ‘On the Theory of Quantum Mechanics’. (1926), vol. 112(762): pp. 661–677. DOI: 10.1098/rspa.1926.0133 (cit. on p. 51).
64. PERCUS, JEROME K. and GEORGE J. YEVICK: ‘Analysis of Classical Statistical Mechanics by Means of Collective Coordinates’. *Phys. Rev.* (1958), vol. 110(1): pp. 1–13. DOI: 10.1103/PhysRev.110.1 (cit. on p. 60).
65. VOGT, M., A. KNÜTTEL, K. HOFFMANN, P. ALTMAYER, and H. ERMERT: ‘Comparison of High Frequency Ultrasound and Optical Coherence Tomography as Modalities for High Resolution and Non Invasive Skin Imaging. Vergleich von hochfrequentem Ultraschall und optischer Kohärenztomographie als Modalitäten für die hochauflösende und nichtinvasive Abbildung der Haut’. *Biomed. Tech. (Berl.)* (2003), vol. 48(5): pp. 116–121. DOI: 10.1515/bmte.2003.48.5.116 (cit. on pp. 64, 65).
66. HINZ, TORSTEN, LIN-KRISTIN EHLER, THORSTEN HORNING, HARALD VOTH, INES FORTMEIER, TANIA MAIER, TOBIAS HÖLLER, and MONIKA-HILDEGARD SCHMID-WENDTNER: ‘Preoperative characterization of basal cell carcinoma comparing tumour thickness measurement by optical coherence tomography, 20-MHz ultrasound and histopathology’. *Acta Derm.-Venereol.* (2012), vol. 92(2): pp. 132–137. DOI: 10.2340/00015555-1231 (cit. on pp. 64, 65).
67. MEYER, N., V. LAUWERS-CANCES, S. LOURARI, J. LAURENT, M-P KONSTANTINO, J-M LAGARDE, B. KRIEF, H. BATATIA, L. LAMANT, and C. PAUL: ‘High-frequency ultrasonography but not 930-nm optical coherence tomography reliably evaluates melanoma thickness in vivo: a prospective validation study’. *Br. J. Dermatol.* (2014), vol. 171(4): pp. 799–805. DOI: 10.1111/bjd.13129 (cit. on pp. 64, 65, 69, 74).
68. BOONE, MARC A. L. M., GREGOR B. E. JEMEC, and VERONIQUE DEL MARMOL: ‘High-definition optical coherence tomography enables visualization of individual cells in healthy skin: comparison to reflectance confocal microscopy’. *Exp. Dermatol.* (2012), vol. 21(10): pp. 740–744. DOI: 10.1111/j.1600-0625.2012.01569.x (cit. on p. 65).
69. BOONE, MARC A. L. M., M. SUPPA, F. DHAENENS, M. MIYAMOTO, A. MARNEFFE, G. B. E. JEMEC, V. DEL MARMOL, and R. NEBOSIS: ‘In vivo assessment of optical properties of melanocytic skin lesions and differentiation of melanoma from non-malignant lesions by high-definition optical coherence tomography’. *Arch. Dermatol. Res.* (2016), vol. 308(1): pp. 7–20. DOI: 10.1007/s00403-015-1608-5 (cit. on p. 65).

-
70. BOONE, MARC A. L. M., SARAH NORRENBERG, GREGOR B. E. JEMEC, and V. DEL MARMOL: 'High-definition optical coherence tomography imaging of melanocytic lesions: a pilot study'. *Arch. Dermatol. Res.* (2014), vol. 306(1): pp. 11–26. DOI: 10.1007/s00403-013-1387-9 (cit. on p. 65).
 71. GAMBICHLER, THILO, IRIS PLURA, MONIKA SCHMID-WENDTNER, KONSTANTINOS VALAVANIS, DANIELA KULICHOVA, MARKUS STÜCKER, AZEM PLJAKIC, CAROLA BERKING, and TANJA MAIER: 'High-definition optical coherence tomography of melanocytic skin lesions'. *J. Biophotonics* (2015), vol. 8(8): pp. 681–686. DOI: 10.1002/jbio.201400085 (cit. on p. 65).
 72. GAMBICHLER, T., M. H. SCHMID-WENDTNER, I. PLURA, P. KAMPILAFKOS, M. STUCKER, C. BERKING, and T. MAIER: 'A multicentre pilot study investigating high-definition optical coherence tomography in the differentiation of cutaneous melanoma and melanocytic naevi'. *J. Eur. Acad. Dermatol. Venereol.* (2015), vol. 29(3): pp. 537–541. DOI: 10.1111/jdv.12621 (cit. on p. 65).
 73. KANAWADE, RAJESH, BENJAMIN LENGENFELDER, TASSIANA MARINI MENEZES, MARTIN HOHMANN, STEFAN KOPFINGER, TIM HOHMANN, URSZULA GRABIEC, FLORIAN KLÄMPFL, JEAN GONZALES MENEZES, MAXIMILIAN WALDNER, and MICHAEL SCHMIDT: 'Improved cancer diagnostics by different image processing techniques on OCT images'. *European Conferences on Biomedical Optics*. Ed. by BOUMA, BRETT E. and MACIEJ WOJTKOWSKI. SPIE Proceedings. SPIE, 2015. DOI: 10.1117/12.2183838 (cit. on pp. 67, 75).
 74. LEE, YIM-KUL and WILLIAM T. RHODES: 'Nonlinear image processing by a rotating kernel transformation'. *Opt. Lett.* (1990), vol. 15(23): p. 1383. DOI: 10.1364/OL.15.001383 (cit. on pp. 67, 96).
 75. DING, HUAFENG, JUN Q. LU, WILLIAM A. WOODEN, PETER J. KRAGEL, and XIN-HUA HU: 'Refractive indices of human skin tissues at eight wavelengths and estimated dispersion relations between 300 and 1600 nm'. *Phys. Med. Biol.* (2006), vol. 51(6): pp. 1479–1489. DOI: 10.1088/0031-9155/51/6/008 (cit. on pp. 67, 72, 96).
 76. MORAN, C. M., N. L. BUSH, and J. C. BAMBER: 'Ultrasonic propagation properties of excised human skin'. *Ultrasound Med. Biol.* (1995), vol. 21(9): pp. 1177–1190. DOI: 10.1016/0301-5629(95)00049-6 (cit. on pp. 68, 72).
 77. ZHENG, Y. P., S. L. BRIDAL, J. SHI, A. SAIED, M. H. LU, B. JAFFRE, A. F. T. MAK, and P. LAUGIER: 'High resolution ultrasound elastomicroscopy imaging of soft tissues: System development and feasibility'. *Phys. Med. Biol.* (2004), vol. 49(17): pp. 3925–3938. DOI: 10.1088/0031-9155/49/17/007 (cit. on pp. 68, 72).

78. GE, LUDI, RICARDO E. VILAIN, SERIGNE LO, KARINA AIVAZIAN, RICHARD A. SCOLYER, and JOHN F. THOMPSON: 'Breslow Thickness Measurements of Melanomas Around American Joint Committee on Cancer Staging Cut-Off Points: Imprecision and Terminal Digit Bias Have Important Implications for Staging and Patient Management: Imprecision and Terminal Digit Bias Have Important Implications for Staging and Patient Management'. *Ann. Surg. Oncol.* (2016), vol. DOI: 10.1245/s10434-016-5196-1 (cit. on p. 69).
79. KOPROWSKI, ROBERT and ZYGMUNT WRÓBEL: *Image processing in optical coherence tomography: Using Matlab*. Katowice, Poland: University of Silesia, 2011. ISBN: 8362462027 (cit. on p. 75).
80. ROGOWSKA, JADWIGA and MARK E. BREZINSKI: 'Image processing techniques for noise removal, enhancement and segmentation of cartilage OCT images'. *Phys. Med. Biol.* (2002), vol. 47(4): pp. 641–655. DOI: 10.1088/0031-9155/47/4/307 (cit. on p. 75).
81. HOJJATOLESLAMI, ALI and MOHAMMAD R. N. AVANAKI: 'OCT skin image enhancement through attenuation compensation'. (2012), vol. 51(21): pp. 4927–4935. DOI: 10.1364/AO.51.004927 (cit. on p. 75).
82. GASCA, FERNANDO, LUKAS RAMRATH, GEREON HUETTMANN, and ACHIM SCHWEIKARD: 'Automated segmentation of tissue structures in optical coherence tomography data'. *J. Biomed. Opt.* (2009), vol. 14(3): p. 034046. DOI: 10.1117/1.3156841 (cit. on p. 75).
83. HORI, YASUAKI, YOSHIAKI YASUNO, SHINGO SAKAI, MASAYUKI MATSUMOTO, TOMOKO SUGAWARA, VIOLETA DIMITROVA MADJAROVA, MASAHIRO YAMANARI, SHUICHI MAKITA, TAKESHI YASUI, TSUTOMU ARAKI, MASAHIRO ITOH, and TOYOHICO YATAGAI: 'Automatic characterization and segmentation of human skin using three-dimensional optical coherence tomography'. *Opt. Express* (2006), vol. 14(5): p. 1862. DOI: 10.1364/OE.14.001862 (cit. on p. 75).
84. KOOZEKANANI, D., K. BOYER, and C. ROBERTS: 'Retinal thickness measurements from optical coherence tomography using a Markov boundary model'. *IEEE Trans Med Imaging* (2001), vol. 20(9): pp. 900–916. DOI: 10.1109/42.952728 (cit. on pp. 75, 96).
85. BEARD, PAUL: 'Biomedical photoacoustic imaging'. (2011), vol. 1(4): pp. 602–631. DOI: 10.1098/rsfs.2011.0028 (cit. on pp. 85, 86).
86. ASHOK, PRAVEEN C., BAVISHNA B. PRAVEEN, NICOLA BELLINI, ANDREW RICHES, KISHAN DHOLAKIA, and C. SIMON HERRINGTON: 'Multi-modal approach using Raman spectroscopy and optical coherence tomography for the discrimination of colonic adenocarcinoma from normal colon'. *Biomed.*

-
- Opt. Express* (2013), vol. 4(10): pp. 2179–2186. DOI: 10.1364/BOE.4.002179 (cit. on p. 89).
87. LIU, CHIH-HAO, JI QI, JING LU, SHANG WANG, CHEN WU, WEI-CHUAN SHIH, and KIRILL V. LARIN: ‘Improvement of tissue analysis and classification using optical coherence tomography combined with Raman spectroscopy’. *SPIE BiOS*. Ed. by TUCHIN, VALERY V., KIRILL V. LARIN, MARTIN J. LEAHY, and RUIKANG K. WANG. SPIE Proceedings. SPIE, 2014: p. 894208. DOI: 10.1117/12.2038508 (cit. on p. 89).
 88. ZAKHAROV, VALERY P., IVAN A. BRATCHENKO, DMITRY N. ARTEMYEV, OLEG O. MYAKININ, DMITRY V. KORNILIN, SERGEY V. KOZLOV, and ALEXANDER A. MORYATOV: ‘Comparative analysis of combined spectral and optical tomography methods for detection of skin and lung cancers’. *J. Biomed. Opt.* (2015), vol. 20(2): p. 25003. DOI: 10.1117/1.JBO.20.2.025003 (cit. on p. 89).
 89. PATIL, CHETAN A., HARISH KIRSHNAMEOORTHY, DARREL L. ELLIS, VAN LEEUWEN, TON G., and ANITA MAHADEVAN-JANSEN: ‘A clinical instrument for combined raman spectroscopy-optical coherence tomography of skin cancers’. *Lasers Surg Med* (2011), vol. 43(2): pp. 143–151. DOI: 10.1002/lsm.21041 (cit. on p. 89).
 90. QI, JI, NARENDRAN SUDHEENDRAN, CHIH-HAO LIU, GREGGY M. SANTOS, ERIC D. YOUNG, ALEXANDER J. LAZAR, DINA C. LEV, RAPHAEL E. POLLOCK, KIRILL V. LARIN, and WEI-CHUAN SHIH: ‘Raman spectroscopy complements optical coherent tomography in tissue classification and cancer detection’. *SPIE BiOS*. Ed. by ALFANO, ROBERT R. and STAVROS G. DEMOS. SPIE Proceedings. SPIE, 2015: p. 931807. DOI: 10.1117/12.2078539 (cit. on p. 89).
 91. MAHER, JASON R., ORANAT CHUCHUEN, MARCUS H. HENDERSON, SANGHOON KIM, MATTHEW T. RINEHART, ANGELA D. M. KASHUBA, ADAM WAX, and DAVID F. KATZ: ‘Co-localized confocal Raman spectroscopy and optical coherence tomography (CRS-OCT) for depth-resolved analyte detection in tissue’. *Biomed. Opt. Express* (2015), vol. 6(6): pp. 2022–2035. DOI: 10.1364/BOE.6.002022 (cit. on p. 89).
 92. VARKENTIN, ARTHUR, MIKHAIL MAZURENKA, ELIAS BLUMENRÖTHER, LEA BEHRENDT, STEFFEN EMMERT, UWE MORGNER, MERVE MEINHARDT-WOLLWEBER, MAIK RAHLVES, and BERNHARD ROTH: ‘Trimodal system for in vivo skin cancer screening with combined OCT-Raman and co-localized optoacoustic measurements’. *J Biophotonics* (2018), vol. DOI: 10.1002/jbio.201700288 (cit. on pp. 89–91, 93, 97, 99, 100, 102, 104).

Bibliography

93. NIEDERHAUSER, J. J., M. JAEGER, M. HEJAZI, H. KEPPNER, and M. FRENZ: 'Transparent ITO coated PVDF transducer for optoacoustic depth profiling'. *Opt. Commun.* (2005), vol. 253(4-6): pp. 401–406. DOI: 10.1016/j.optcom.2005.05.005 (cit. on p. 89).
94. MAZURENKA, M., L. BEHRENDT, M. MEINHARDT-WOLLWEBER, U. MORGNER, and B. ROTH: 'Development of a combined OCT-Raman probe for the prospective in vivo clinical melanoma skin cancer screening'. *Rev. Sci. Instrum.* (2017), vol. 88(10): p. 105103. DOI: 10.1063/1.5004999 (cit. on pp. 89, 93, 94).
95. *American National Standard for safe use of lasers*. Orlando, FL: Laser Institute of America, 2014. ISBN: 1940168007 (cit. on p. 93).
96. BOCZAR, MAREK, MAREK J. WÓJCIK, KRZYSZTOF SZCZEPONEK, DOROTA JAMRÓZ, ADAM ZIĘBA, and BOŻENA KAWAŁEK: 'Theoretical modeling of infrared spectra of aspirin and its deuterated derivative'. *Chem Phys* (2003), vol. 286(1): pp. 63–79. DOI: 10.1016/S0301-0104(02)00912-6 (cit. on p. 94).
97. STRITZEL, JENNY, MAIK RAHLVES, and BERNHARD ROTH: 'Refractive-index measurement and inverse correction using optical coherence tomography'. *Opt Lett* (2015), vol. 40(23): pp. 5558–5561. DOI: 10.1364/OL.40.005558 (cit. on p. 96).
98. DÍAZ, JESÚS DÍAZ, JENNY STRITZEL, MAIK RAHLVES, OMID MAJDANI, EDUARD REITHMEIER, TOBIAS ORTMAIER, and BERNHARD ROTH: 'One step geometrical calibration method for optical coherence tomography'. *J. Opt.* (2016), vol. 18(1): p. 015301. DOI: 10.1088/2040-8978/18/1/015301 (cit. on p. 96).
99. ZUIDERVELD, KAREL: 'Contrast Limited Adaptive Histogram Equalization'. *Graphics Gems*. Elsevier, 1994: pp. 474–485. ISBN: 9780123361561. DOI: 10.1016/B978-0-12-336156-1.50061-6 (cit. on p. 96).
100. ZOOK, J. D. and S. T. LIU: 'Pyroelectric effects in thin film'. *J Appl Phys* (1978), vol. 49(8): pp. 4604–4606. DOI: 10.1063/1.325442 (cit. on p. 97).
101. BERGMAN, J. G., J. H. MCFEE, and G. R. CRANE: 'PYROELECTRICITY AND OPTICAL SECOND HARMONIC GENERATION IN POLYVINYLIDENE FLUORIDE FILMS'. *Appl. Phys. Lett.* (1971), vol. 18(5): pp. 203–205. DOI: 10.1063/1.1653624 (cit. on p. 97).
102. HESS, P. and J. PELZL: *Photoacoustic and photothermal phenomena: Proceedings of the 5th International Topical Meeting, Heidelberg, Fed. Rep. of Germany, July 27-30, 1987*. Vol. v. 58. Springer series in optical sciences. Berlin and New York: Springer-Verlag, 1988. ISBN: 3662137054 (cit. on p. 97).

-
103. STRITZEL, J., O. MELCHERT, M. WOLLWEBER, and B. ROTH: ‘Effective one-dimensional approach to the source reconstruction problem of three-dimensional inverse optoacoustics’. *Phys. Rev. E* (2017), vol. 96(3). DOI: 10.1103/PhysRevE.96.033308 (cit. on p. 98).
 104. ZHAO, JIANHUA, HARVEY LUI, DAVID I. MCLEAN, and HAISHAN ZENG: ‘Automated autofluorescence background subtraction algorithm for biomedical Raman spectroscopy’. *Appl Spectrosc* (2007), vol. 61(11): pp. 1225–1232. DOI: 10.1366/000370207782597003 (cit. on p. 98).
 105. GNIADOCKA, MONIKA, PETER ALSHEDE PHILIPSEN, SIGURDUR SIGURDSSON, SONJA WESSEL, OLE FAURSKOV NIELSEN, DANIEL HØJGAARD CHRISTENSEN, JANA HERCOGOVA, KRISTIAN ROSSEN, HENRIK KLEM THOMSEN, ROBERT GNIADOCKI, LARS KAI HANSEN, and HANS CHRISTIAN WULF: ‘Melanoma diagnosis by Raman spectroscopy and neural networks: structure alterations in proteins and lipids in intact cancer tissue’. *J. Invest. Dermatol.* (2004), vol. 122(2): pp. 443–449. DOI: 10.1046/j.0022-202X.2004.22208.x (cit. on p. 98).
 106. TFAILI, SANA, CYRIL GOBINET, GWENDAL JOSSE, JEAN-FRANÇOIS ANGIBOUST, MICHEL MANFAIT, and OLIVIER PIOT: ‘Confocal Raman microscopy for skin characterization: a comparative study between human skin and pig skin’. *Analyst* (2012), vol. 137(16): pp. 3673–3682. DOI: 10.1039/c2an16292j (cit. on pp. 98, 103).
 107. SAVITZKY, ABRAHAM. and M. J. E. GOLAY: ‘Smoothing and Differentiation of Data by Simplified Least Squares Procedures’. *Anal. Chem.* (1964), vol. 36(8): pp. 1627–1639. DOI: 10.1021/ac60214a047 (cit. on p. 98).
 108. GIBBS, J. WILLARD: ‘Fourier’s Series’. *Nature* (1898), vol. 59(1522): p. 200. DOI: 10.1038/059200b0 (cit. on p. 101).

List of Figures

- 2.1 Exemplary scheme of human skin. The layers' content and thickness varies for different regions of the human body. Hairless, thick skin (hand palm, sole of the foot) has other thickness relations of the different layers and features than thin, hairy skin (most of the human body) [13]. 6
- 2.2 Absorption coefficient μ_a of hematocrit (Hct, blood cells), hemoglobin (Hb) and water. In the therapeutic window (blue region) the absorption has the lowest values [15]. 8
- 2.3 Spectral dependence of reduced scattering coefficient μ'_s of human skin (*in vitro*) [18]. In the therapeutic window (blue region) Mie scattering (green line) is the dominant process, whereas Rayleigh scattering (red line) plays a marginal role. The observed scattering is a superposition (blue line) of both processes. 9
- 2.4 Illustration of the ABCDE criteria for melanomas. If one or more criteria match to the lesion it is advised to make an appointment with a physician. 11
- 2.5 Different melanoma stages, inspired by [26]. 12
- 3.1 Sketch of a typical scanning time domain OCT system. A broadband light source is split into a reference beam with a variable length and a sample beam (z-direction). A galvanometer based scanning system allows for 2-D and 3-D imaging (x-y-plane). Both reflected beams are cross-correlated at the photo detector measuring the center of the ring-shaped interference pattern. 15
- 3.2 Sketch of typical time domain OCT signal. An infinitesimally thin interface (left-hand side) is measured in z-direction. The detected signal (middle plot) is an intensity modulation (red curve). The FWHM of the envelope (gray dashed line) corresponds to the coherence length of the light source l_c . The detected interface, which is located at a certain depth is represented by the light gray box with a finite thickness. On the right-hand side the broadened image of the object is shown. 15

3.3	Sketch of a typical scanning spectral domain OCT system. A broadband light source is split into a reference beam and a sample beam (z-direction). A galvanometer based scanning system allows for 2-D and 3-D imaging (x-y-plane). The cross-correlated beam is spectrally analyzed by a spectrometer (grating and a linear CCD array).	16
3.4	Sketch of a typical frequency domain OCT signal. Two infinitesimally thin interfaces are measured in z-direction. The detected signal (middle plot) is a superposition of intensity modulations (red and blue curve) on top of the source spectrum (gray dashed line). Each reflection at a particular depth produces a modulation of a corresponding frequency. Different components of the superposition are decomposed via a DFT and produce the depth profile (right plot).	17
3.5	Sketch of a typical scanning swept source OCT system. A swept laser light source is split into a reference beam and a sample beam (z-direction). A galvanometer based scanning system allows for 2-D and 3-D imaging (x-y-plane). Both reflected beams are cross-correlated at the fast photo detector recording the time evolution of the intensity signal.	18
3.6	Sketch of a typical scanning swept source OCT signal. The reflected reference field E_1 and the reflected, time delayed sample field E_2 interfere on the detector. The time evolution of the interference of the swept fields (red curve) has a beat signature over time (envelope, gray dashed line). An infinitesimally thin interface produces a sinusoidal beat with a specific frequency. A DFT provides the sample's depth profile.	19
3.7	Scheme of the field propagation in a typical SD-OCT system. The sample beam (z-axis) and the reference beam (x-axis) interfere through the combination via the beam splitter. The measured detector signal intensity i_D corresponds to the interference intensity of the reference field E_R and the sample field E_S [39].	21
3.8	Fit of normalized measured data of 10% milk concentration including focal contribution (top) and with deconvolved CPSF (bottom). The fitting curve is marked as cyan dashed line. Due to artifacts the first and the last data points are excluded from the evaluation (gray).	26
3.9	OCT A- and B-scan of a thumbnail. On the left-hand side a typical A-scan is presented as a part (marked by a cyan line) of a B-scan image (right-hand side). The light gray curve is the original data whereas the black curve is the smoothed data guiding the eye. The peaks are linked to the corresponding positions of the interfaces between different layers of the skin. In the B-scan shadowing occurs, a typical OCT problem.	28

3.10	Concatenated cross-sectional B-scans (left) produce a C-scan which is a 3-D point cloud (center). On the right hand side the <i>en face</i> image of the measured region is shown marked by a red box.	28
3.11	Artifacts present in FD-OCT. Both images were obtained on human skin. (a) At the top of the image (zero delay) the structure is flipped or mirrored. A hair, not visible in the picture, is producing a signal due to mirroring. In the focal region (vertical center) the reflected light is causing autocorrelation artifacts producing vertical lines (blue ellipse). (b) A typical ripple distortion caused by motion of the sample.	29
3.12	Principle of image distortion by different refractive indices. The acquired image does not show the original equidistant pattern. Real distances are modified by the indices n_1 to n_4	31
4.1	Scheme of the SD-OCT setup. Two broadband SLDs are used as light sources. The scanning probe is a Michelson interferometer with adjustable reference arm length. A galvanometric mirror set and an F-Theta objective allow scanning the surface in x and y direction (in the surface plane). The spectral signal is detected by a linear CCD-array.	36
4.2	OCT measurement of a homogeneous liquid phantom with 50 wt. % milk in demineralized water. The particles, with a size of $\approx 1 \mu\text{m}$, are not resolvable with the used OCT system and produce homogeneous scattering and a decreasing uniform gradient.	38
4.3	OCT measurement of a PVA hydrogel phantom with microsphere scatterers. Clusters are present as white grains of different sizes. The upper blurred clusters are out of the focus of the OCT beam.	39
4.4	Rendered image of the double layer cuvette. The core element consists of two spacers combined with double faced adhesive tape on each side. Three cover glasses are pasted to create two chambers for the liquid. A socket is holding the assembly vertically, where a cap is closing up the cuvette.	40
4.5	OCT measurement of a stacked PVA hydrogel phantom with two layers of different melanin concentrations. The focal plane is in the lower part. For a better index matching the space between the layers is filled with demineralized water.	40
4.6	PVA phantom with spacer ring (6 cm inner diameter) and glass plates as described in Section 4.2.2. The measurement points to calculate the refractive index of the phantom are marked red for d_{air} (optical distance between glass plates in air) and blue for d_{PVA} (optical distance between glass plates in PVA).	41

4.7	Measured OCT depth profiles (A-scans, green) of milk phantoms with different milk concentrations. The dashed cyan lines are the fitting functions.	43
5.1	Light propagation scheme of simulated photons in a scattering medium. The contributing trajectories are highlighted in blue and green. The black paths are also calculated but do not contribute to the OCT signal simulation.	47
5.2	Schematic of different photon scattering orders. The left and the middle photon trajectories represent the least scattered photons (LSP), which include the ballistic case. The trajectory on the right shows an example for multiple scattered photons (MSP). Δz is the depth interval of the current bin. [61]	50
5.3	Weighting function F_w for different combinations of parameters a and b as function of the number of scattering events N_{se} (see also Equation 5.6). [61]	51
5.4	Contribution of MSP (green) and LSP (magenta) to the simulated OCT signal (cyan) for μ_s^{LIN} ranging from 2.7 cm^{-1} to 54 cm^{-1} . Comparison to ballistic signal (BSP, purple) and deconvolved OCT signal (black) in the ROI (red vertical lines). The legend for all panels is depicted in the lower right panel. [61]	54
5.5	Intensity profile of ballistic photons, LSP (always including ballistic photons), MSP, and sum of LSP and MSP (all backscattered photons) for $\mu_s^{LIN}=40 \text{ cm}^{-1}$. (a) best fit with $a = 5$, $b = 4.2$, (b) fit with $a = 1$, $b = 1$. Red vertical lines indicate the ROI. [61]	55
5.6	Best fit parameters: (a) 3-D surface and (b) 2-D intensity plot of the difference of fitted and measured μ_s as function of parameters a and b (for 25% milk, $\mu_s^{LIN} = 13.5 \text{ cm}^{-1}$) and (c) minimal difference for various μ_s^{LIN} ranging from 2.7 (bottom line) to 54 cm^{-1} (top line). The dashed vertical line indicates the parameter $a = 5$, which is chosen as working point for the model. [61]	56
5.7	Linear dependence of parameter b (considered scattering events) on concentration of scatterers for fixed $a = 5$ (sharpness of the number of scattering events, see Figure 5.3), proving the predictability of μ_s^{OCT} . [61]	57
5.8	Comparison of fitted measurement (OCT data, black) and fitted simulation (Sim data, gray) and their fits (green dashed line for OCT, cyan dash-dotted line for simulation data) for a milk concentration of 10% (top) and of 100% (bottom). The ROI, where a good fit of the simulated data can be achieved, is reduced for larger concentrations. [61]	58

5.9	Comparison of goniometer measurements μ_s^{GON} , simulation input data μ_s^{LIN} (green) linearly extrapolated from these measurements, Sim output μ_s^{SIM} (black) and OCT measurements μ_s^{OCT} (cyan). The gray line is a linear extrapolation from the goniometer measurements as a guide to the eye. The inset shows a magnified part of the data for low milk concentrations where μ_s^{OCT} and μ_s^{GON} similar. The scattering coefficients obtained by simulation are in good agreement with the OCT values, which are more and more differing from the linear extrapolated values for larger concentrations. [61]	59
6.1	Consecutive OCT image post-processing of two representative lesions (columns I (poor contrast) and II (good contrast)). Row (a) unprocessed, (b) after contrast enhancement by CLAHE, (c) after rotating kernel transform, (d) after thresholding. The dermoepidermal junction is marked by arrows, respectively. [8]	68
6.2	Example of the depth determination of a representative melanocytic lesion (same as Fig. 1 II): (top) post-processed OCT image, (bottom) Gaussian smoothed HFUS image. [8]	69
6.3	Histology of the melanocytic lesion shown in Figures 6.1 II and 6.2: (top) H&E stained (x40), used for histopathological measurement of infiltration depth in this work and (bottom) after staining with Melan-A (x100). [8]	70
6.4	Comparison of histology and OCT measurement of a lesion with a thickness of approximately 1mm. The corresponding region is marked by the red dashed lines. [8]	71
6.5	Bland-Altman plots: a) OCT measurements, b) HFUS measurements. Blue lines: mean difference between measurement and histology, respectively. Red lines: 95 % limits of agreement estimated by mean difference \pm standard deviation (SD) of the difference. [8]	73
6.6	Measured lesion thickness as determined by OCT, HFUS and histopathology; data is sorted according to increasing thickness measured by histopathology (gold standard). [8]	73
7.1	Exemplary peak detection on one A-scan. The raw signal (gray) is smoothed (black curve) before peak detection. The peak candidates for boundaries are marked by cyan circles.	77
7.2	First step of boundary detection. Boundary candidates o1, o2 and i1 to i4 are printed with different colors (see legend on top).	79
7.3	Classification of the points to correspond to the different interfaces (see legend on top).	80

List of Figures

7.4	Segmentation of stratum corneum (between black and red line) and epidermis (between red and green line).	80
7.5	3-D-segmentation of a melanocytic lesion corresponding to Figure 7.4. The gray surface corresponds to the outer boundary. The green surface is the DEJ. The red elliptic cylinder marks the lesion dimensions. A vertical line is drawn at the thickest point annotated with the thickness.	82
7.6	Thickness map of the lesion presented before. The red ellipse and its major axes indicate the lesion dimensions. The red annotations contain the sizes of the axes. The global maximum is marked by a cyan box annotated with the thickness value.	82
7.7	Work-flow scheme of the segmentation and thickness assessment algorithm.	83
8.1	Comparison of the sensitivity pattern with and without the optoacoustic detector foil on top of the phantom measured with OCT. The vertical lines crossing the uppermost interfaces originate from dust particles at the surface and interference effects due to signal intensity saturation. The vertical and horizontal lines at the bottom of the images are mirror artifacts due to reflection on the bottom interface (not on the image).	87
8.2	Example of a combined measurement with optoacoustics and OCT. The OCT depth is corrected by the refractive index of the PVA sample containing melanin as an absorber for optoacoustics.	88
8.3	Experimental setup of the combined OA-OCT-Raman system. Laser line filter (LF), long-pass filter (LPF), lens(L), scanning mirrors (M), spectrometer (Spectr) [92].	90
8.4	Rendered image of the combined OCT-Raman probe with an applicator and a spacer ring. The OCT part is framed red and the Raman part is highlighted with a green frame [92].	91
8.5	Photo of the OA handheld applicator on a nevus. The illumination fiber is aligned coaxially with the detection point. The ITO electrodes and the detector zone are highlighted in green [92].	93
8.6	a) Cross-sectional image of a processed melanoma. The contrast is enhanced as guide to the eye. The green line shows the upper skin layer (stratum corneum), whereas the red line denotes the detected DEJ. b) The green volume represents the segmented lesion, similar to a) (region between green and red line) but in three dimensions. c) Thickness map of the lesion. The maximum is marked by a black square. The blue ellipse in b) corresponds to the red ellipse in c) [92].	97

8.7	a) Plot of the acquired, energy normalized OA signal (blue) from a lesion and the according fit for the pyroelectric contribution (Pyro, orange), b) OA signal after subtraction of pyroelectric contribution (cyan) and the deconvolved, Fourier filtered signal (green). The histopathologic lesion thickness (gray frame) corresponds well to the distance of the main slopes of the deconvolved OA signal. This OA measurement corresponds to the lesion presented in Figure 8.9. The corresponding data was produced by Elias Blumenröther [92].	99
8.8	a) Acquired Raman spectrum (cyan) from a skin lesion. The intensity is represented by CCD camera counts. The baseline (red) is a polynomial fit of 9th order. b) After baseline correction and smoothing, the signal shows a periodic modulation distorting the Raman signal. This is probably from an etalon effect of the back illuminated CCD sensor or the Rayleigh filter. This effect can be removed by an FFT notch filter rendering the skin Raman lines visible. c) The resulting data shows a representative Raman spectrum with distinct peaks, notably the resonant carotenoid peaks (orange) [92].	100
8.9	a) Enhanced OCT image of a thin lesion (benign melanocytic junction nevus) with manual thickness assessment of 0.18 mm. b) Dermatoscopic image (left, 1 mm per line distance). c) Histopathology with an assessed lesion thickness of 0.179 mm. The lesion corresponds to the lesion obtained with OA in Figure 8.7 [92].	102
8.10	Smoothed spectra of a melanocytic lesion (cyan) and of normal skin from the same patient as reference (red). The spectra are normalized to the band at 1800 cm^{-1} . Typical skin lines are represented by gray vertical lines and the resonant carotenoids by orange vertical lines. The lesion corresponds to Figure 8.7 and 8.9 [92].	104
A.1	Photo of the whole Thorlabs Telesto-II setup. The commercial probe (left) is attached on an optical table and the combined OCT-Raman probe (right) attached on the trolley. PC (black chassis) and spectrometer/source (light gray chassis) are placed on the second level below the table. The trolley with the equipment was also used as mobile setup in the clinical study.	112
A.2	Photo of the commercial Thorlabs probe. It was used for preliminary investigations.	113
A.3	Applicator attachment to the commercial OCT probe. It was designed as a first attempt to fix the skin for OCT measurements. It was used during first clinical trials and the preclinical study in Chapter 6.	114

List of Figures

- A.4 Photo of the final modified scientific Thorlabs probe for simultaneous Raman and OCT measurements, denoted as OCT-Raman probe. It was used during the preclinical study in Chapter 6 and for the investigations in Chapter 8. 115
- A.5 Goniometer GON360 (Instrument Systems) was used to investigate the scattering profile of low scattering media. 117

List of Tables

- 2.1 *T* parameter classification of melanoma, corresponding thickness and recommended surgical excision safety margins [23]. 12
- 4.1 Overview of extracted effective scattering coefficients μ_s^{OCT} acquired from the prepared phantoms (ratio of milk/water is given by weight percent). R-squared is the coefficient of determination indicating the fit quality. 43
- 5.1 Overview of prepared phantom (ratio of milk/water is given by weight percent). Values for μ_s^{LIN} were used as input for the simulations and are either measured by goniometer (m) or extrapolated (e). The value for 7.5 wt. % is interpolated (i). 53
- A.1 Optical performance specifications – TELESTO II. Source: Thorlabs . 116
- A.2 Performance Specifications – GON360. Source: Instrument Systems . 118



Arthur Varkentin

Lebenslauf

Persönliche Angaben

Geburt **5. August 1985**, Purkary (Moldawien).

Berufserfahrung

- 11/2017–heute **wissenschaftlicher Mitarbeiter**, *Laserzentrum Hannover e.V.*
- 11/2013–05/2017 **wissenschaftlicher Mitarbeiter**, *Hannoversches Zentrum für Optische Technologien - HOT*, Leibniz Universität Hannover.
- 08/2009–03/2012 **studentische Hilfskraft im Rechenzentrum des Instituts**, *Max-Planck-Institut für Gravitationsphysik, Teilinstitut Hannover*.

Studium und Ausbildung

- 11/2013–heute **Doktorand**, *Hannoversches Zentrum für Optische Technologien - HOT*, Leibniz Universität Hannover.
Thema der Dissertation: *Thickness Determination of Melanocytic Nevi by means of Optical Coherence Tomography*
voraussichtlicher Abgabetermin: September/Oktober 2017
- 04/2011–10/2013 **Master**, *Leibniz Universität Hannover*, Hannover, M.Sc. Physik, mit Schwerpunkt Festkörperphysik/Optik.
Thema der Masterarbeit: *Spindynamik in verspannten Quantenstrukturen bei Raumtemperatur*
- 10/2006–04/2011 **Bachelor**, *Leibniz Universität Hannover*, Hannover, B.Sc. Physik.
Thema der Bachelorarbeit: *Ultrastabile Phasenmodulation zur Echtzeit-Spinrausmessung*
- 07/2005–06/2006 **Wehrdienst**, *Ausbildungszentrum Panzertruppen*, Munster, freiwillig verlängert auf 12 Monate, eingesetzt als Kraftfahrer (Klasse C) für Panzerfahrzeuge bei der Truppenausbildung.
- 06/2005 **Abitur**, *Europaschule Humboldt-Gymnasium*, Gifhorn.

Danksagung

Prof. Dr. Bernhard Roth danke ich für die Betreuung der Arbeit und für die vielen Freiheiten, die ein guter Nährboden für diese Arbeit und meine persönliche Entwicklung waren.

Prof. Dr. Uwe Morgner danke ich für das Korreferat und die Vermittlung an das HOT ohne die es niemals zu dieser Arbeit gekommen wäre.

Prof. Dr. Steffen Emmert danke ich für die außergewöhnlich guten Rahmenbedingungen und das tolle Miteinander bei unserer klinischen Studie in Göttingen und in Rostock.

Ein Dank geht auch an Dr. Maik Rahlves, der wichtigen fachlichen Input gegeben hat und damit zu der Qualität dieser beigetragen hat.

Vielen Dank an Dr. Merve Wollweber, die mit den richtigen Fragen oftmals eine gute Route legte.

Ich möchte mich bei meinen Kollegen aus dem Projekt *MeDiOO* bedanken, die offen für Ideen waren und auch immer Quelle neuer Inspiration.

Elias Blumenröther danke ich für die vielen Diskussionen, die meine Arbeit voran gebracht haben und für seinen Anteil der Optoakustik an dem multimodalen System.

Dank geht auch an Jenny Stritzel, die neben ihrer eigenen Arbeit die Last der Finanzplanung des Projektes auf sich nahm und uns andere damit entlastete.

Vielen Dank an die gesamte Belegschaft des *Hannoverschen Zentrums für Optische Technologien* (HOT) für das tolle zwischenmenschliche Klima und einen guten Platz zum Arbeiten.

Danke an Martin für die zahlreichen hervorragenden Kaffeepausen und die *co-operative* Entspannung und fachliche Expertise der Raman-Spektroskopie.

Mein Interesse an der Wissenschaft und insbesondere der Mathematik und Physik haben meine Leistungskurs-Lehrer Torsten Micheels und Dr. Gelbhaar stets befeuert, sodass nichts anderes außer ein Physik-Studium infrage kam. Auch dafür einen herzlichen Dank.

Ein besonderer Dank gilt meinen Eltern Ida und Viktor, die mich auf meinem Weg durch das Studium begleitet haben und mich nicht nur finanziell unterstützt haben, sondern mir auch menschlich vieles mit auf den Weg gegeben haben.

Auch meinen Schwiegereltern Gisela und Rolf möchte ich für alle Unterstützung danken, die sie mir und meiner Familie zuteilwerden ließen. Ich denke da an die Kinderbetreuung oder an das Asyl für meine Frau und meine Kinder beim Endspurt.

Dir Silke, mein Schatz, danke ich aus tiefstem Herzen und zolle dir größten Respekt für das Managen des Familienunternehmens, insbesondere zum Ende dieser Arbeit als ich gerade nicht so viel Zeit für die Familie aufbringen konnte.